



ENGINEERING DOCTORATE SCHOOL
SECTION: MECHANICAL AND INDUSTRIAL ENGINEERING

CYCLE XXVI

STRUCTURAL, FERROELECTRIC AND PIEZOELECTRIC
PROPERTIES OF EPITAXIAL PMN-PT THIN FILMS DEPOSITED
BY PULSED LASER DEPOSITION

Muhammad Boota
PhD Student

Prof. Edoardo Bemporad
Tutor

Prof. Edoardo Bemporad
Coordinatore

Doctorate Dissertation

**STRUCTURAL, FERROELECTRIC AND PIEZOELECTRIC
PROPERTIES OF
EPITAXIAL PMN-PT THIN FILMS
DEPOSITED BY PULSED LASER DEPOSITION**



Muhammad Boota

Doctorate studies have been performed under guidance of

◆ Supervisor: Prof. dr. ing. Edoardo Bemporad
Materials Science and Technology Group (STM)
Engineering Department: Mechanical and Industrial Engineering
University of Rome "ROMA TRE" 00146 Rome, Italy

◆ Supervisor: Prof. dr. ing. A. J. H. M. Rijnders
Inorganic Materials Science Group (IMS)
MESA+ Institute for Nanotechnology
Faculty of Science and Technology
University of Twente, 7500 AE Enschede, The Netherlands

◆ Assistant Supervisor: Dr. ing. Giulia Lanzara
Materials Science and Technology Group (STM)
Engineering Department: Mechanical and Industrial Engineering
University of Rome "ROMA TRE" 00146 Rome, Italy

PhD studies have been accomplished at

◆ Materials Science and Technology Group (STM)
Engineering Department
Section: Mechanical and Industrial Engineering
University of Rome "ROMA TRE" 00146 Rome, Italy

◆ Inorganic Materials Science Group (IMS)
MESA+ Institute for Nanotechnology
Faculty of Science and Technology
University of Twente, 7500 AE Enschede, The Netherlands

Thesis Commission Members:

Full Members (Membri effettivi)

- ◆ Prof. dr. ing Ennio Antonio Carnevale
University of Florence, Florence, Italy
- ◆ Prof. dr. ing. Giancarlo Chiatti
University of Rome “Roma Tre” Rome, Italy
- ◆ Ass. Prof. dr. ing. Fabio Giulii Capponi
University of Rome “La Sapienza” Rome, Italy

Experienced Members (Membri Esperti)

- ◆ Dr. ing. Uwe Schulz
German aerospace centre, Köln, Germany
- ◆ Dr. ing. Francesco Salvatore
CNR, Italy

This dissertation to be publically defended on 12th of June 2014 at 10:00 am.

Financial Support:

The research work reported in this dissertation has been financially supported by the Engineering Doctorate School of University of Rome "ROMA TRE" and by NanoNextNL, a micro and nanotechnology consortium of the Government of the Netherlands and 130 partners.

Abstract

Ferroelectric oxides, most notably PZT, are typically used for the fabrication of high performing piezoelectric MEMS devices for the purpose of sensing and actuation. An alternative to PZT is the relaxor ferroelectric such as PMN-PT. Bulk PMN-PT shows a 5-10 times larger piezo-response than bulk PZT ceramics and has a large electromechanical coupling coefficient of $k_{33} \approx 0.9$. Therefore, this material is an auspicious candidate for hyperactive MEMS devices for sensor and actuator applications. This thesis deals with the study of epitaxial PMN-PT films for the purpose of sensing and actuation.

Perovskite phase and (001) orientation pure epitaxial PMN-PT films were fabricated by carefully controlling the fabrication conditions. Within a relative narrow process window to achieve phase and orientation pure films, the effect of the growth conditions like substrate temperature, fluence, target-substrate distance and ambient gas pressure was investigated. This study shows that polarization is more sensitive to substrate temperature than to target distance and much less to fluence and least to gas pressure.

It is known that better lattice matching can broaden the processing window. Superior lattice matching was achieved using a PZT buffer layer between the PMN-PT and SRO bottom electrode resulting in a significant improvement in crystallinity and consequently in properties of the PMN-PT films. Furthermore the effect of lattice strain was investigated by varying the PZT interfacial layer composition in a wide range. The PMN-PT films showed giant self-bias field which can be tuned by the composition of the PZT interfacial layer. This is of significance for devices like energy scavengers and low energy consumption sensors that preferably operate at zero bias voltage.

The highest longitudinal piezoelectric coefficient (d_{33}) was achieved for PMN-PT films deposited on PZT (50/50) interfacial layer with lowest self-bias field. For some applications, it is desirable to have a higher d_{33} as well as a high self-bias. It is known that doped PZTs can produce self-bias field. Therefore, PMN-PT films were deposited on Nb and Fe doped PZT interfacial layers. PMN-PT films on doped PZT interfacial layer show a higher self-bias along with a higher d_{33} . Furthermore the effect of Nb-doped PZT interfacial layer thickness on the properties of PMN-PT was investigated, which showed a variation in properties associated with epitaxial strain.

Besides epitaxial strain, the residual strain (substrate induced strain) due to the difference of thermal expansion coefficients between substrate and deposited film, show an influence on the ferro and piezoelectric properties of epitaxial PMN-PT films. To study the effect of substrate induced strain on the ferro and piezoelectric properties, PMN-PT films were prepared on a wide range of substrates. This study shows that substrate induced strain has a significant effect on the

structural properties of PMN-PT films and consequently on the ferro and piezoelectric properties of these films. The knowledge of strain effect on properties is useful to engineer a PMN-PT film with certain desired properties.

Silicon is the gold standard substrate for the fabrication of MEMS sensors. To study the effect of orientation on properties, epitaxial PMN-PT films with different out of plane orientation [(001) and (110)] were prepared using a CeO₂/YSZ bilayer buffer and symmetric SrRuO₃ electroded silicon substrates by carefully controlling the growth conditions. The ferroelectric and piezoelectric properties of these ferroelectric capacitors exhibited orientation dependence. The (001) oriented films show a relatively large self-bias voltage compared to the (110) oriented films. This is ascribed to a strain gradient layer in the relaxor at the interface with the bottom electrode. The aging behaviour of (001) films was superior compared to that of (110) films due to less structural defects. Nevertheless a superior effective, longitudinal piezoelectric coefficient ($d_{33,eff}$) for (110) oriented films was observed compared to (001) oriented films, due to a less dense columnar structure. Furthermore, a PMN-PT thin film based sensing device (cantilever) was also fabricated and characterized with respect to ferroelectric and piezoelectric response which showed excellent properties.

*All praises for Allah who is the entire source of knowledge and
wisdom endowed to mankind*

and

*all respect for The Holy Prophet (PBUH) who is forever a torch of
guidance*

Table of contents

Chapter 1. Introduction

1.1 Overview of ferroelectric materials	2
1.2 Epitaxial thin films and misfit strain	4
1.3 Thin film nucleation and growth	5
1.4 Ferroelectric fundamentals	7
1.5 Relaxor and standard ferroelectrics	9
1.6 Thesis outline	12
1.7 References	13

Chapter 2. Fabrication and Characterization

2.1 Introduction	17
2.2 Thin films fabrication by Pulsed Laser Deposition	17
2.2.1 Principle of PLD system	17
2.2.2 PLD system structure	18
2.2.3 Epitaxial PMN-PT heterostructures	21
2.2.4 Device design for analysis	22
2.3 Characterization techniques	24
2.3.1 Structural analysis	24
2.3.2 Microstructure and morphological studies	25
2.3.3 Electrical investigations	28
2.3.4 Electromechanical investigations	31
2.4 References	33

Chapter 3. Processing of PMN-PT films

3.1 Introduction	36
3.2 Experimental procedure	39
3.2.1 Samples fabrication	39
3.2.2 Samples characterization	40
3.3 Results and discussions	40
3.3.1 Phase optimization and structural properties	40
3.3.2 Ferroelectric and piezoelectric properties	44
3.3.3 Surface morphology and microstructure	49
3.4 Conclusions	50
3.5 References	51

Chapter 4. PMN-PT films on PZT interfacial layer

4.1 Introduction	54
4.2 Experimental procedure	55
4.2.1 Samples fabrication	55
4.2.2 Samples characterizations	56
4.3 Results and discussions	57
4.3.1 Structural properties	57
4.3.2 Ferroelectric properties and aging behaviour	61

4.3.3 Dielectric and piezoelectric properties	69
4.4 Conclusions	71
4.5 References	72

Chapter 5. PMN-PT films on doped PZT interfacial layer

5.1 Introduction	75
5.1.1 Hard verses soft doped PZTs	75
5.1.2 Iron and Niobium doped PZTs	77
5.2 Experimental procedure	79
5.2.1 Samples fabrication	79
5.2.2 Samples characterization	80
5.3 Results and discussions	81
5.3.1 Structural properties	81
5.3.2 Ferroelectric and piezoelectric properties	83
5.3.3 Ferroelectric response stability behaviour	86
5.4 Effect of Nb-PZT layer thickness on PMN-PT properties	87
5.4.1 Structural properties	88
5.4.2 Ferroelectric and piezoelectric properties	91
5.4.3 Ferroelectric response stability analysis	93
5.5 Conclusions	94
5.6 References	95

Chapter 6. Substrate induced strain in PMN-PT films

6.1 Introduction	99
6.2 Substrates and substrate pre-treatments	102
6.3 Experimental procedure	103
6.3.1 Samples fabrication	103
6.3.2 Samples characterization	104
6.4 Results and discussions	104
6.4.1 Structural properties	104
6.4.2 Ferroelectric and piezoelectric properties	109
6.5 Conclusions	112
6.6 References	113

Chapter 7. Integration with silicon

7.1 Introduction	116
7.2 Orientation control of PMN-PT films [(001) and (110)]	118
7.2.1 Thin films growth	118
7.2.2 Thin films characterizations	119
7.2.3 Results and discussions	120
7.3 Fabrication of PMN-PT film based free standing cantilever	129
7.3.1 Deposition of PMN-PT films stack for cantilever beam	129
7.3.2 Structure, ferroelectric and piezoelectric characterization	130
7.3.3 Structural properties of PMN-PT films stack	130
7.3.4 Fabrication process of free standing cantilever	131
7.3.5 Analysis of free standing cantilever beam	133
7.4 Conclusions	134

7.5 References	135
Acknowledgements	137
List of Publications	139

1.

Introduction

Chapter Overview:

This chapter describes brief history of ferroelectric materials together with evolution of ferroelectric technology. Nucleation and growth of epitaxial thin films along with hetero-epitaxy induced strain and strain relaxation by structural defects is briefly explained. The material used in this dissertation is a solid solution of relaxor and standard ferroelectric. The fundamentals related with relaxors and standards ferroelectric are also presented. The last part of this chapter describes the outline of this thesis.

1.1 Overview of ferroelectric materials

An unusual physical characteristic to attract the other objects when heated was observed in tourmaline during the beginning of the 18th century. About half a century later, a Swedish scientist Carl Linneaus speculates a correlation between this observed phenomenon and electricity. This speculation was confirmed and the effect named pyroelectricity within a decade by a German Physist Franz Aepinus. Pyroelectricity refers to the ability of a material to generate temporary voltage while heating or cooling [1]. In 1880, pyroelectricity led to the discovery of the piezoelectricity by Piere Curie and Jacques Curie. They observed that certain materials (Tourmaline, Quartz, Cane sugar and Rochelle salt) exhibit charge generation on application of mechanical stresses on their surfaces. They applied mechanical stress by placing small weights on the surface of the crystal and found that the magnitude of the generated charge is proportional to the applied stress [2]. The German Physicist Wilhelm G. Hankel introduced the term piezoelectricity derived from ancient Greek words *piezo* or *piezein* (pressed or squeezed) and *elektron* (Amber: ancient source of electric charge). The inverse piezoelectric effect was proposed by French Physicist Gabriel Lippmann and was experimentally verified by the Curie brothers in the same year [1]. Direct and inverse piezoelectric effect is schematically described in figure 1.1.

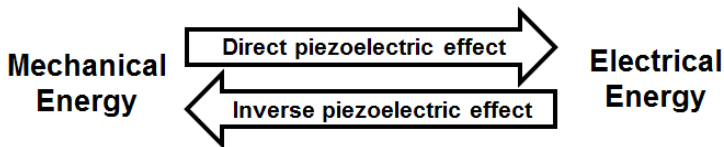


Figure 1.1: Schematic description of the direct and inverse piezoelectric effect.

In 1920 Valasek found that the direction of polarization can be reversed in Rochelle salt ($\text{KNaC}_4\text{H}_4\text{O}_6 \cdot 4\text{H}_2\text{O}$) by applying external electric field. The phenomenon is called ferroelectricity. This was the first discovered ferroelectric material [3]. This material was entitled ferroelectric due to the occurrence of spontaneous polarization which is analogous to spontaneous magnetization in ferromagnetic materials.

It is notable here that although the prefix ferro is used, most of the ferroelectric material do not contain iron. Subsequently potassium di-hydrogen phosphate (KH_2PO_4) having similar properties to Rochelle salt was reported in 1935.

It was common believe that a hydrogen bond is necessary for a material to possess ferroelectric properties until Wul and Goldman identified the presence of ferroelectricity in barium titanate (BaTiO_3) in 1945 [4]. This was the first oxide material with perovskite crystal structure showing ferroelectric behavior. This discovery initiated the curiosity to search for ferroelectricity in oxide materials. Due to structural simplicity, chemical and mechanical stability, ferroelectricity at room temperature and simplicity in fabrication, BaTiO_3 is included in the list of the highly investigated/used ferroelectric materials. During this era numerous ferroelectric oxide materials with perovskite structure like KNbO_3 , KTaO_3 , LiNbO_3 , PbTiO_3 were discovered [5-8].

The struggle to fabricate better and better ferroelectric materials resulted in the discovery of lead zirconate titanate (PZT) in the 1950s [9]. PZT is a solid solution of PbTiO_3 (PTO) with PbZrO_3 (PZO). Due to its superior properties compared to BaTiO_3 , this material has replaced it in almost all its piezoelectric applications. To date, this material is the most widely employed piezoelectric material due to its superior properties and relatively high Curie temperature.

In 1997, S. E. Park and T. R. Shrout reported PZN-PT and PMN-PT single crystal ceramics with ultrahigh strain up to 1.7% and large electromechanical coupling coefficient of $k_{33} \approx 0.9$. These materials show one order of magnitude superior piezoelectric response compared to PZT due to electrical field induced phase transitions from rhombohedral to tetragonal phase. Subsequently giant piezoelectricity was reported by S. H. Baek et al. for epitaxial PMN-PT thin films deposited on silicon substrate in 2011[10-11]. This material got huge interest to fabricate hyperactive MEMS devices in recent years. Further details about epitaxial PMN-PT films will be discussed in chapter 4.

1.2 Epitaxial thin films and misfit strain

Epitaxy is derived from two ancient Greek words epi (placed or resting upon) and Taxis (arrangements). During thin film growth, epitaxy refer to extended single crystal film formation on top of a single crystal substrate. It was most likely first observed to take place in alkali halide crystals over a century ago [12]. The word Epitaxy was apparently introduced by French mineralogist L. Royer in 1928 [13].

Epitaxy can be divided into two types, homo-epitaxy and hetero-epitaxy. Homo-epitaxy refers to the situation when fabricated film and substrate are of the same material. For instance, epitaxial growth of silicon thin film on top of the single crystal silicon substrate. Under optimum conditions, homo-epitaxial layers possess generally less structural defects compared to the substrate, purer than substrates with doping possibility independent of the substrate [12]. On the other hand, hetero-epitaxy refers to the situation when the deposited film and the substrate consist of two different materials. For example, epitaxial growth of SrRuO_3 on top of the SrTiO_3 single crystal substrates. Hetero-epitaxial growth of functional materials is commonly performed for the fabrication of electronics, photonics and MEMS (micro electromechanical systems) devices. The difference between homo-epitaxy and hetero-epitaxy is schematically demonstrated in figure 1.2.

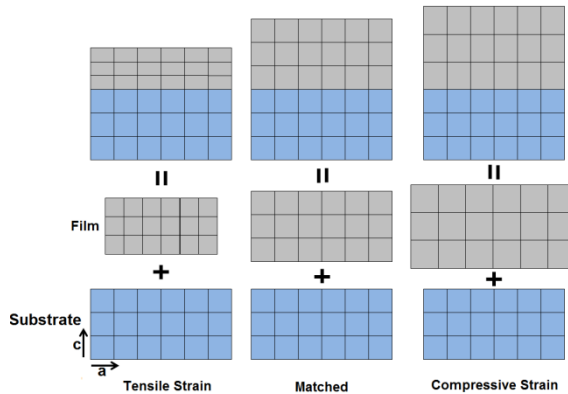


Figure 1.2: Schematic view of the lattice matched or homo-epitaxial structure together with hetero-epitaxial structure under compressive and tensile strain.

When the deposited film and the substrate crystal are identical (Homo-epitaxy), there is no bonding strain at the interface due to perfect lattice matching. However in the hetero-epitaxy case, the lattice parameters are not identical. The lattice mismatch can be defined as (equation 1.1).

$$\text{Lattice mismatch} = \frac{a_f - a_s}{a_f} \quad 1.1$$

Where a_f and a_s are lattice parameters of the film and substrate respectively. The lattice mismatch plays a crucial role during hetero-epitaxial growth of functional thin films. In case of very small mismatch ($\leq 1\%$) between film and substrate, the hetero-interface is essentially similar to homo-epitaxy. Nevertheless the difference in thermal expansion coefficients and film-substrate chemistry can still strongly influence the functional properties of the deposited film. In case of relatively large lattice mismatch ($\geq 5\%$), crystallographic lattice mismatch is either accommodated by the formation of structural defects (edge dislocations) or by tensile/compressive lattice strain at the interface. The strain relaxation by structural defects where the film reflects the bulk lattice parameters is referred to as relaxed epitaxy. The latter case, where the film is strained to the substrate is referred to as strained epitaxy. Strain epitaxy is mainly observed in the hetero-epitaxial layer of similar structure like perovskite SrRuO_3 on top of perovskite SrTiO_3 single crystal substrate.

1.3 Thin films nucleation and growth

Interests in thin film fabrication exists since the 1920s from the experiments performed on evaporated films in Cavendish laboratory in Cambridge, England [14]. At earliest stage of thin film fabrication, adatoms (adatoms refer to the atoms that reach to the substrate surface from the source) with sufficient energy reach the substrate and form clusters as a result of diffuse process on the substrate surface. These clusters become stable after a certain critical thickness. The process of formation of the stable clusters is called nucleation. Many of such

events take place simultaneously at the nucleation stage. As growth continues, coalescence of the stable clusters results in continuous film on the substrate surface. Three growth modes are typically observed during thin film growth.

1. Layer by Layer growth or Frank-van der Merwe mode
2. Island growth or Volmer-Weber mode
3. 2D followed by 3D growth or Stranski-Krastanov mode

In layer by layer growth mode, the smallest stable cluster coalesce in two dimensions only to form planar sheets. During growth, subsequent layers only nucleate with the completion of the underneath layer. In this growth mode, adatoms are more strongly bound to the substrate compared to one other which promotes the layer by layer growth.

In island growth mode, stable clusters nucleate on the substrate surface which only grows in three dimensions to form islands. In this case, adatoms are more strongly bound to each other as compared to the substrate which facilitates the formation of 3D islands.

The Stranski-Krastanov growth mode is a combination of above two modes. Initially films grow in layer by layer mode followed by transition to three dimensional mode. Due to lattice mismatch, strain energy accumulates in the films. After certain critical thickness, the system releases its energy by triggering the island growth mode.

Besides this, another growth mode (step flow) is also reported in the literature [15-16]. This mode differs from layer by layer growth mode in the sense that it occurs only in one direction on the terraces of low miscut angle substrates. Three basic growth modes are schematically shown in figure 1.3.

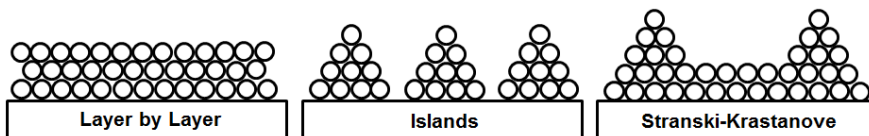


Figure 1.3: Schematic view of the basic growth modes.

1.4 Ferroelectric fundamentals

The family of materials that possess spontaneous polarization whose direction can be reversed by applying external electric field are said to be ferroelectric materials [17]. The relationship between ferro, pyro and piezoelectric materials is schematically shown in figure 1.4. It is evident from this correlation that all ferroelectric materials are both pyroelectric and piezoelectric and all pyroelectric materials are piezoelectric [18]. For instance, PMN-PT possesses spontaneous polarization and is ferro, pyro and piezoelectric simultaneously, whereas Tourmaline does not possess spontaneous polarization, is not ferroelectric, but is pyro and piezoelectric.

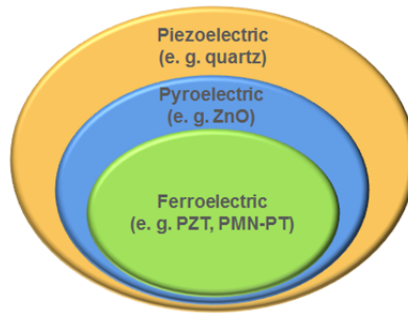


Figure 1.4: Relationship between ferro, pyro and piezoelectric materials.

Crystalline materials can be categorized into seven basic crystal systems; i.e. triclinic, monoclinic, orthorhombic, tetragonal, rhombohedral, hexagonal and cubic. These can be further divided into 32 sub-classes termed as point groups. Twenty point group out of all 32 groups are non-centro-symmetric and exhibit piezoelectric behaviour which is a pre-condition for this. Out of twenty piezoelectric point groups, half exhibit single polar axis and are pyroelectric with temperature dependence. The materials that do not show spontaneous polarization are termed as non-polar or paraelectric [19]. It is valuable to mention here that symmetry considerations are helpful to predict whether a material possesses such

a property (Ferro, Pyro, Piezo) or not. Nevertheless this does not give any information about quantification of any specific property. Parameters like fabrication conditions, density, crystal structural etc. can influence the properties significantly.

Superior properties has been reported for the inorganic ferroelectric oxides like BaTiO_3 , BiFeO_3 , $\text{Pb}(\text{Zr}_x\text{Ti}_{1-x})\text{O}_3$ and $\text{Pb}(\text{Mg}_{1/3}\text{Nb}_{2/3})\text{O}_3\text{-PbTiO}_3$. These materials belong to the perovskite family and can be described with general formula ABO_3 . Perovskites are refer to the catagory of materials that have crystal structure similar to CaTiO_3 , discovered by Gustave Rose in 1839 and named perovskite after Count Lev Alekseevich Perovski, a Russian mineralogist [20]. When the unit cell of the perovskite material is cubic, then the atom A will assemble itself at the corner position of the cube. The atom B and O (oxygen) will reside in body centre and face centre positions of the cube respectively. PMN-PT is a perovskite material with one A site cation and three B site cations. Lead is located at position A whereas other three (Mg, Nb, Ti) are located at position B. The B site cations are randomly distributed inside the material. The oxygen will occupy at face center of the cube. The perovskite unit cell is schematically shown in figure 1.5.

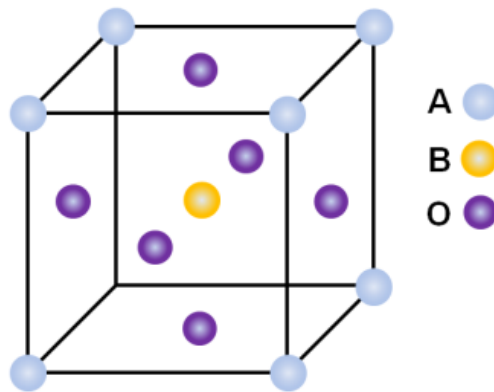


Figure 1.5: Schematic view of perovskite unit cell with atomic locations.

Ferroelectric materials show a paraelectric to ferroelectric phase transition at a specific temperature. This transition temperature is named as Curie temperature (T_c). Above Curie temperature (paraelectric phase), the unit cell is centro-symmetric and does not exhibit spontaneous polarization. Upon cooling (below T_c), it adapts

the ferroelectric phase. The symmetry of the unit cell also changes from centro-symmetric structure to non-centro-symmetric structure. Inside the perovskite unit cell, the central ion moves from its equilibrium position within the oxygen octahedra. Consequently the material transforms from paraelectric phase to ferroelectric phase [21]. Functional ferroelectric material (PMN-PT) discussed in this dissertation retains cubic crystal structure (paraelectric phase) above Curie temperature. Below Curie temperature, it adopts tetragonal or rhombohedral crystal structure (ferroelectric phase) as a consequence of structural transformation from the cubic structure. It is worth to mention here that there is a composition dependent border line separating tetragonal from rhombohedral crystal structure below Curie temperature named as morphotropic phase boundary [22]. The direction of polarization in tetragonal and rhombohedral crystal structure is along $\langle 001 \rangle$ and $\langle 111 \rangle$ respectively. The polarization refers to the total dipole moment (μ) per unit volume (V) and can be written as

$$\text{Polarization} = \frac{\sum \mu}{V} \quad 1.2$$

Typically in ferroelectric materials, the polarization is not uniformly aligned in the same direction inside the entire crystal. The region inside the crystal in which spontaneous polarization is aligned in one direction is named as domain. The interface separating two domains is called domain wall. The non-uniformly aligned polarization in bulk ferroelectric materials can be aligned by applying external field named as poling process. However, the poling is not needed for epitaxial films due to self-alignment of the domains during fabrication.

1.5 Relaxor and standard ferroelectrics

Lead magnesium niobate - Lead titanate (PMN-PT) reported in this dissertation is a solid solution of lead magnesium niobate (PMN) and lead titanate (PT). The $\text{PbMg}_{1/3}\text{Nb}_{2/3}\text{O}_3$ (PMN) is a classical relaxor having cubic crystal structure at high temperature and pseudo-cubic at lower temperature [23]. The PbTiO_3 (PT) is a typical ferroelectric material that shows cubic structure above Curie

temperature ($T_c \approx 770\text{K}$) and tetragonal below T_c [24]. The relaxors can be distinguished from normal ferroelectrics in terms of properties summarized in table 1.1.

Table 1.1: Property difference between relaxor and normal ferroelectric (Table adopted from reference 25).

Properties	Normal Ferroelectric	Relaxor
Dielectric temp. dependence $K = K(T)$	Sharp 1 st or 2 nd order transition about Curie temperature (T_c)	Broad diffuse phase transition about Curie Maxima (T_{\max})
Dielectric temp. and freq. dependence $K = K(T, \omega)$	Weak frequency dependence	Strong frequency dependence
Dielectric behavior in paraelectric range ($>T_c$)	Fellow Curie-Weiss law $\frac{1}{K} = \frac{C}{T - T_c}$	Fellow Curie-Weiss square law $\frac{1}{K} = \frac{1}{K_{\max}} + \frac{(T - T_{\max})^2}{2K_{\max}\delta^2}$
Remanent Polarisation (Pr)	Strong remanent Polarisation (Pr)	Weak remanent Polarisation (Pr)
Scattering of light	Strong anisotropy (birefringent, Δn)	Very weak anisotropy to light (pseudo-cubic)
Diffraction of X-rays	Line splitting indicating spontaneous deformation (paraelectric \rightarrow ferroelectric phase)	No X-rays line splitting giving a pseudo cubic structure

Relaxor (PMN) typically exhibit diffuse phase transition with significant dispersion (temperature and frequency dependent) in dielectric permittivity. Secondly, low temperature behavior under high alternating fields exhibit unpretentious hysteretic response, a necessary and sufficient condition for ferroelectricity. Nevertheless, unlike a normal ferroelectric, the hysteretic response is not lost suddenly at T_{\max} but decays more slowly in a nonlinear mode. Moreover relaxors exhibit longer coherence length while probing with radiations (light, X-rays) i.e. no evidence of optical anisotropic or x-rays line splitting even well below T_{\max} . The model proposed by Smolensky suggests that the origin of diffuse phase transition is due to

local compositional fluctuations associated with B-site cation disorder, resulting in a distribution of Curie temperatures [23]. Subsequently Cross proposed a super-paraelectric model suggesting that the existence of localized polar micro-regions which are analogous to spin clusters behavior in super-paramagnets. This model successfully explains properties like frequency dependence of the permittivity, dielectric aging, and metastable switching from micro to macro domains in relaxors [25-26]. The clear evidence of nonpolar region (NPRs) came from refractive index measurement experiments performed by Burns and Dacol. They reported the formation of static or slowly moving nanopolar-regions (PNRs) about 620K having a size of a few nm. This temperature is referred to as Burns temperature (T_B) [27-28]. Subsequent studies performed by different techniques (X-rays, neutrons scattering, HR-TEM etc.) shows consensus about PNRs which begin to appear at 618K which grow 2-3nm in size near T_B . Further cooling up to 160K enhances the size ($\approx 10\text{nm}$) and volume fraction increases upto 30 percent. A static change in NPRs can be induced by high electric field and micro domains can be obtained which lead to the observation of ferroelectricity at lower temperatures [29-32].

A crystalline solid solution [(1-x)PMN- (x)PT] is shown to be possible over a whole range of concentrations of x [33]. Colla et. al. studied the frequency dependence of dielectric permittivity for wide range of PMN-PT compositions and found that above $x \sim 0.3$ the value of T_{max} becomes frequency independent. These investigations suggest that for PT concentrations higher than ~ 0.3 , the phase transformation becomes largely like a conventional ferroelectric phase transition [34]. Xu et.al. investigated the PMN-PT (67:33) single crystals and found the co-existence of monoclinic and rhombohedral phase, in the same single crystals. They suggested that electric field induced polarization rotation takes place via rhombohedral-monoclinic-tetragonal phase transition in this single crystal. Subsequent studies performed by Noheda et.al using synchrotron X-rays confirmed these findings. It was also found that the monoclinic

phase does not exist as single phase in this composition. These studies shows that PMN-PT (67/33) system can be characterized by multiphase components and complex phase behaviour [35-36]. It is notable that PMN-PT (67/33), which is a bulk morphotropic phase boundary (MPB) composition, was employed for the investigations reported in this dissertation.

1.6 Thesis Outline

The scientific investigations reported in this dissertation are focused on epitaxial PMN-PT thin films for sensor and actuator applications. This dissertation consists of seven chapters which can be further sub-divided into two main parts. The first part (Chapter 1 and 2) covers the fundamentals like evolution of ferroelectric technology, basics of ferro and piezoelectricity, epitaxial thin film nucleation and growth and difference between relaxors and normal ferroelectrics. This part also covers fabrication and characterization techniques which were intensively utilized during this experimental research. The second part consists of five principal chapters (Chapter 3 - 7) covering scientific studies performed in this research.

Chapter 3 discusses the issues concerning perovskite phase development during growth of epitaxial PMN-PT films. The effect of processing conditions like laser energy density (fluency), substrate temperature, target-substrate distance and deposition pressure on perovskite phase formation and properties are investigated in detail.

Chapter 4 deals with the epitaxial PMN-PT films deposited on a PZT interfacial layer. The epitaxial PMN-PT films were deposited on wide range of PZT compositions. The influence of PZT interfacial layer composition on structural, ferro and piezoelectric properties was investigated in detail.

Chapter 5 describes the effect of doped PZT interfacial layers on structural, ferro and piezoelectric properties of epitaxial PMN-PT films. $\text{Pb}(\text{Zr}_{0.52}\text{Ti}_{0.48})\text{O}_3$ doped with one mole percent Iron (acceptor

doping) and Niobium (donor doping) was selected for these studies. Doped PZT interfacial layer samples were compared with undoped $\text{Pb}(\text{Zr}_{0.52}\text{Ti}_{0.48})\text{O}_3$ interfacial layer samples. Additionally, the effect of Nb doped PZT interfacial layer thickness on properties of epitaxial PMN-PT films was examined.

Chapter 6 refer to the studies of epitaxial PMN-PT film deposited on different substrates. The effect of misfit strain was investigated using a wide variety of substrates. The PZT interfacial layer having very close lattice matching with PMN-PT films was used as interfacial layer to minimize epitaxial strain and to enhance the effect of thermal induced strain which was analyzed.

Chapter 7 is designated to epitaxial PMN-PT films deposited on silicon substrates. Epitaxial PMN-PT films with different out of plane orientation were fabricated on CeO_2/YSZ bilayer buffered silicon substrate. The effect of crystallographic orientation on properties of epitaxial PMN-PT films was studied. Besides this, PMN-PT thin film based free standing cantilevers were fabricated and characterized.

1.7 References

- [1] Jan Holterman and Pim Groen, An interdiction to piezoelectric material materials and components, Sticing Applied piezo, The Netherlands (2012).
- [2] P. J. Curie and P. Curie, Bull. Soc. Min. de France. 3 (1880) 90.
- [3] J. Valasek. Phys. Rev.15 (1920) 537.
- [4] B. Wul and I. M. Goldman. C. R. Acad. Sci. USSR, 46 (1945) 12.
- [5] M. E. Lines and A. M. Glass. Principles and Applications of Ferroelectric and Related Materials. Clarendon Press Oxford, (2004).
- [6] K. A. Rabe, T. J. M., and C. H. Ahn (eds.). Physics of Ferroelectrics: A Modern Perspective. Springer-Verlag (2007).

- [7] G. Shirane, S. Hoshino, and K. Suzuki. *Physical Review*, 80 (1950) 1105.
- [8] B. T. Matthias and J. P. Remeika. *Phys. Rev.*, 76 (1949) 1886.
- [9] G. H. Haertling, *Ferroelectric Ceramics: History and Technology*, *J. Am. Ceram. Soc.*, 82 (1999) 797.
- [10] S. E. Park and T. R. Shrout, *J. Appl. Phys.*, 82 (1997) 1804.
- [11] S. H. Baek, J. Park, D. M. Kim, V. A. Aksyuk, R. R. Das, S. D. Bu,...and C. B. Eom, *Science*, 334 (2011) 958.
- [12] Milton Ohring, *The materials science of thin films*, Academic press, California (1992) 307.
- [13] L. Royer, *Bull. Soc. Fr. Mineral Cristallogr.*, 51 (1928) 7.
- [14] B. Lewis and J. C. Anderson, *Nucleation and growth of thin films*, Academic Press, London, 1982.
- [15] G. Rosenfeld, B. Poelsema, and G. Comsa, *Epitaxial growth modes far from equilibrium*. In D. A. King (ed.) *The chemical physics of solid surfaces*. Elsevier Science B.V. (1997).
- [16] K. Sangwal and R. Rodriguez-Clemente, *Surface morphology of crystalline materials*, Trans Tech Publications (1991).
- [17] M. E. Lines, A. Alstair and A. Glass, *Principals and applications of ferroelectric and related materials*, Claredon Press, Oxford, England (1977).
- [18] C. R. Bowen, H. A. Kim, P. M. Weaver and S. Dunn, , *Energy Environ. Sci.*, 7 (2014) 25.
- [19] W. Massa. *Crystal structure determination*. Springer-Verlag, Berlin, Germany (2004).
- [20] R. V. Gaines, H. C. W. Skinner, E. E. Foord, B. Mason, and A. Rosenzweig, *Dana's new mineralogy*. John Wiley & Sons, Inc. (1997).
- [21] K. M. Rabi, C. H. Ahn and J. M. Triscone, *Physics of ferroelectrics* (2007).
- [22] B. Noheda, D. E. Cox, G. Shirane, G.A. Gonzalo, L.E. Cross and S. E. Park, *Appl. Phys. Lett.*, 74(14) (1999) 2059.
- [23] G. A. Smolensky, A. I. Agranovskaya, *Sov. Phys. Solid State*, (1959) 1429.

- [24] G. Shirane, J. D. Axe, J. Harada, and J. P. Remeika, Phys. Rev. B2 (1970) 155.
- [25] L. E. Cross, Relaxor Ferroelectrics, Ferroelectrics, 76 (1987) 241.
- [26] G. A. Smolenskii, Physical Phenomena in Ferroelectric with Diffused Phase Transition, Journal Phys. Soc. of Japan, 28 (1970) 26.
- [27] G. Burns and B. A. Scott, Solid State Comm. 13 (1973) 473.
- [28] G. Burns, F. H. Dacol, Phys. Rev. B 28 (1983) 2527.
- [29] N. D. Mathan, E. Husson, G. Calvarin, J. R. Gavarri, A.W. Hewat, A. Morell, J. Phys. Cond. Matter. 3 (1991) 8159.
- [30] A. Naberezhnov, S. Vakhrushev, B. Dorner, D. Stauch, H. Moudden, Eur. Phys. J. B 11 (1999) 13.
- [31] D. Viehland, M. C. Kien, Z. Xu, J. F. Li, Appl. Phys. Letters. 67 (1995) 2471.
- [32] I. K. Jeong, T.W. Darling, J. K. Lee, Th. Proffen, H. Heffner, J. S. Park, K. S. Hong, W. Dmowski, T. Egami, Phys. Rev. Lett., 94 (2005) 147602.
- [33] H. Ouchi, K. Nagano, and S. Hayakawa, J. Am. Ceram. Soc., 48 (1965) 630.
- [34] E. V. Colla, N. K. Yushin, and D. Viehland, J. Appl. Phys., 83 (1998) 3298.
- [35] G. Xu, H. Luo, H. Xu and Z. Yin, Phys. Rev., B 64 (2001) 020102(R)
- [36] B. Noheda, D. E. Cox and G. Shirane, Phys. Rev., B 66 (2002) 054104.

2.

Fabrication and Characterization

Chapter Overview:

This chapter describes the experimental techniques employed to deposit and characterize epitaxial PMN-PT thin films. All layer stacks reported in this dissertation are fabricated by the Pulsed Laser Deposition (PLD) and the specific deposition machine (setup) is described in this chapter. The characterization techniques used for morphological and structural analysis along with ferroelectric, dielectric and piezoelectric properties are also briefly explained in the subsequent sections.

2.1 Introduction

Thin film deposition techniques are generally divided into Physical Vapour Deposition (PVD) and Chemical Vapour Deposition (CVD). Both film growth methods have their own advantages and drawbacks. Pulsed Laser Deposition (PLD) belongs to the PVD category and was employed for the fabrication of the heterostructures reported in this dissertation.

The use of the pulsed laser as direct energy evaporation source for thin films growth has been explored since the discovery of pulsed laser. The first experiments employing pulsed laser were performed in 1965 [1-3]. Soon after, Schwarz and Tourtellotte demonstrated the deposition of ferroelectric thin films using PLD in 1968 [4]. Pulsed Laser Deposition (PLD) was popularized after in-situ growth of the epitaxial high temperature superconducting thin films [5]. Numerous features make PLD attractive including stoichiometric transfer of material from target regardless of complexity of the crystal chemistry, generation of energetic species, hyperthermal reaction between ablated cations and background gas in the ablation plasma and its compatibility with a wide range (ultrahigh vacuum - 1Torr) of background pressures. Today, PLD is used for the deposition of superconductors, semiconductors, ferroelectrics, ferromagnetics, metals, insulators, polymers and even the biological materials [6].

2.2 Thin films fabrication by Pulsed Laser Deposition

2.2.1 Principle of PLD system

Pulsed laser deposition is based on evaporation of material utilizing an intense laser beam in a vacuum chamber. A pulsed laser beam is focused on to a target composed of the material to be deposited. At sufficiently high laser energy density, each laser pulse

vaporizes/ablates small amount of the target material creating a plasma plume. This ablated material is ejected from the target and expands in a highly forwarded direction normal to target plane (plume) and provides material flux for the film nucleation and growth. Laser ablation parameters like the absorption coefficient of the target, reflectivity of the target material, pulse duration, wavelength and laser energy density (fluency) influence the characteristics of the plume, consequently affecting the properties of the deposited films [7-8]. Besides the laser ablation parameters, thin film fabrication conditions like deposition ambient/pressure, substrate temperature, target-substrate distance and repetition rate (frequency) are the deciding factors for the deposition of high quality thin films material.

The fundamental interaction between laser light (photons) and matter results in the penetration of the laser radiation into the target. This induces oscillations in the optical electrons of the target material which thereby converts into the electron excitations. Following this, the electrons transfer energy to lattice ions by means of electron-phonon (electron-ion) collisions [6]. This process can heat up the target material up to very high temperature (4500°C with heating rate of 10^{12} K/Sec) in a few nanoseconds [9]. This very high temperature causes instantaneous evaporation of the target material. This evaporated material scatters in the laser beam causing even further absorption of the laser energy. This process results in a very high pressure in front of the target. Due to pressure gradients, the evaporated material expands rapidly in the forward direction. These material particles move perpendicular to the target surface providing flux for the thin film nucleation and growth [10].

2.2.2 PLD System Structure

The Pulsed Laser Deposition (PLD) setup employed for the fabrication of heterostructures reported in this dissertation is schematically shown in the figure 2.1.

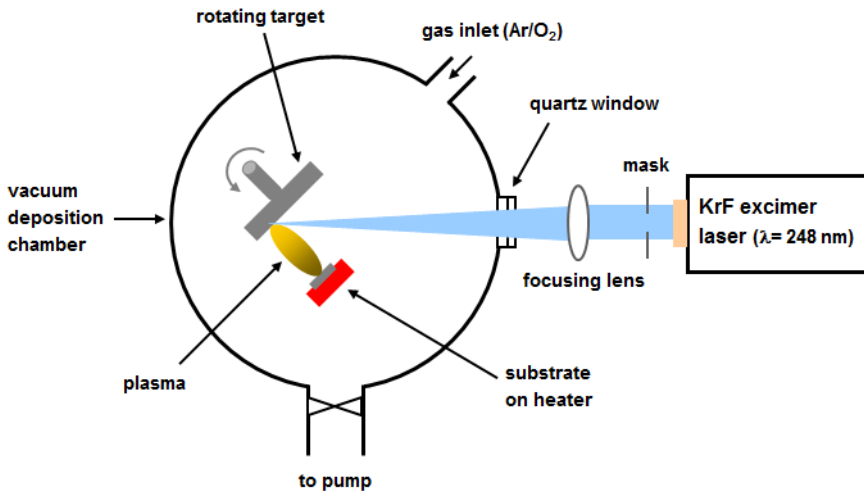


Figure 2.1: Schematic view of the Pulsed Laser Deposition (PLD) setup.

The experimental setup consists of a KrF Excimer laser (Lamda Physics) which operates at wavelength of 248nm. The maximum energy per pulse is 1500 mJ with a pulse duration of 25ns (Pulse full width at half maximum). This laser can be manoeuvred at a repetition rate (frequency) of 1-50 Hz. The selection of the homogeneous (uniform energy density) part of the laser beam is crucial and is performed by a rectangular mask in this setup. The laser beam enters into the deposition chamber via a quartz window by making an angle of 45 degree with the target. The laser spot size on the target can be adjusted by focusing a lens placed close to the quartz window.

The vacuum chamber is fitted with a turbo molecular pump capable of attaining a base pressure of 10^{-7} mbar. The vacuum chamber is equipped with the target holder to install a maximum of four targets simultaneously. The deposition chamber is equipped with oxygen and argon as background gasses. The laser ablation experiments can be performed using mixture of oxygen and argon in a preferred ratio. Similarly deposition experiments can also be performed in pure oxygen or argon ambient. The deposition pressure can be adjusted ranging from 10^0 to 10^{-3} mbar by means of mass flow

controller (0-40ml/min). The substrate holder designed for this system is a steel block-style hot stage. The thermocouple is embedded in this stage to measure the temperature. The substrate temperature during growth experiments can be adjusted from room temperature (RT) to 850°C with control of cooling/heating rate. The substrates can be fixed on the substrate holder by silver epoxy (Silver filled Epoxy EE129-4, Epoxy Technology Inc. Billeria, USA). The substrate holder is placed in front of the target (parallel) during deposition experiments. The distance between substrate and target can be adjusted in a range of 3cm to 9cm. The deposition parameters used during the fabrication of the heterostructures are summarized in table 2.1.

Table 2.1: Investigated materials with deposition conditions used during fabrication experiments.

Parameters	YSZ	CeO ₂	SrRuO ₃	PZT	PMN-PT
Ambient pressure (mbar)	0.02 (Ar/O ₂)	0.016 (O ₂)	0.13 (O ₂)	0.1 (O ₂)	0.27 (O ₂)
Deposition Temperature (°C)	800	800	600	600	585
Target-Substrate distance (mm)	59	58	49	60	60
Fluency (J/cm ²)	2.1	2.5	2.5	3.5	2.0
Frequency (Hz)	4	4	4	2	4
Spot Size (mm ²)	3.35	3.0	1.9	3.0	3.0
Mask (mm ²)	98 (7hole)	98 (7hole)	56.5	102	102
Deposition rate (nm/pulse)	0.023	0.042	0.022	0.042	0.0253

It is necessary to mention here that substrate temperature, deposition pressure, target to substrate distance, fluency and repetition rate are crucial processing parameters which must be carefully optimized to achieve high quality thin films. It is also necessary to mention that starting layers ($\approx 6\text{nm}$) of YSZ films are deposited in pure argon environment and then growth was continued in pure oxygen ambient. Deposition experiments were performed by using YSZ target with 8mole percent Y₂O₃ stabilized in 92mole percent ZrO₂. However PMN-PT target is composed of 67 percent PMN and

33 percent PT which is the morphotropic phase boundary composition for bulk PMN-PT ceramics [11].

2.2.3 Epitaxial PMN-PT heterostructures

Epitaxial PMN-PT films reported in this dissertation were deposited on a variety of single crystal substrates including LaAlO_3 , LSAT, NdGaO_3 , SrTiO_3 , DyScO_3 , MgO , YSZ, and silicon. To achieve an epitaxial growth, the good lattice match of the film with the underlying layer and/or substrate is a pre-requisite [12]. Material with perovskite structure such as SrRuO_3 suits well for epitaxial growth of PMN-PT films owing to its similar crystal structure and close in-plane lattice matching. PMN-PT and SrRuO_3 can grow with cube on cube epitaxial relation on most of the substrates employed during this work. The other advantages to use SrRuO_3 as bottom electrode includes good electrical conductivity, remarkable chemical stability and superb fatigue resistance. The bulk in-plane lattice parameter of the materials employed during investigations are given in table 2.2.

Table 2.2: Bulk in-plane lattice constants of the materials (substrates and films) employed during the studies.

Material	a_{pc} (Å)
LaAlO_3	3.79
NdGaO_3	3.86
LSAT	3.87
SrTiO_3	3.905
DyScO_3	3.95
MgO	4.20
Silicon	5.43
YSZ	5.14
CeO_2	5.41
SrRuO_3	3.93
PMN-PT	4.02

YSZ was also fabricated as thin films besides single crystal substrate, however CeO_2 , SrRuO_3 and PMN-PT are only prepared as films. It is not suitable to fabricate epitaxial PMN-PT films directly on silicon owing to the large lattice mismatch. The other processing difficulty includes interdiffusion and interfacial reactions between silicon substrate and lead (Pb) from PMN-PT material [13]. To reduce lattice mismatch and to avoid interfacial reactions YSZ and CeO_2 films were employed to achieve epitaxial growth of PMN-PT films on silicon. A limited number of samples were also deposited on Si coated with SrTiO_3 by Molecular Beam Epitaxy [14]. The details of epitaxial growth of PMN-PT films on silicon substrates will be discussed in chapter 7.

2.2.4 Device design for analysis

Epitaxial PMN-PT or PZT/PMN-PT bilayer were sandwiched between SrRuO_3 electrodes. These heterostructures were fabricated on different substrates including buffered silicon. To minimize the risk of unwanted contaminations, complete heterostructures were prepared subsequently without breaking the vacuum. The devices in parallel plate capacitor geometry were patterned by standard photolithography and argon ion beam etching. The standard photolithography process involves the following steps.

- Spin coating of the photoresist (OiR 908-17)
- Baking of the photoresist (hardening step)
- Mask alignment and exposure to ultraviolet light
- Developing of the photoresist

During this step, devices with size $200 \times 200 \mu\text{m}^2$ were patterned. The SrRuO_3 top electrode was etched by argon ion beam. This dry etching step was performed at 2×10^{-3} mbar in pure argon environment. During this step, the area which was not protected by photoresist was etched and vice versa. Finally the photoresist was removed by keeping the samples in acetone for half an hour. A schematic of the samples before and after structuring the top electrode is shown in figure 2.2.

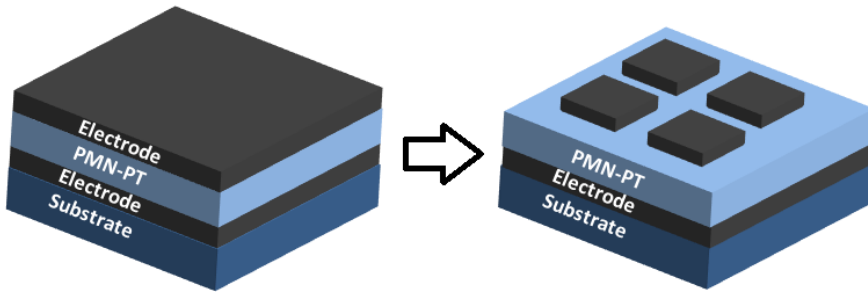


Figure 2.2: Schematic view of the sample before and after patterning of the top electrode.

Epitaxial PMN-PT thin film heterostructures structured in parallel plate ferroelectric capacitor geometry were glued on top of metal plate by silver epoxy (Silver filled Epoxy EE129-4, Epoxy Technology Inc. Billeria, USA) to perform electrical and electromechanical investigations. The electrical connection between bottom electrode and metal plate was established by the same silver epoxy as shown in figure 2.3. The electrical and piezoelectric studies were performed by making connection between top electrode and metal plate (ground). The sample glued by silver epoxy on metal plate with electrical connections is schematically shown in figure 2.3.

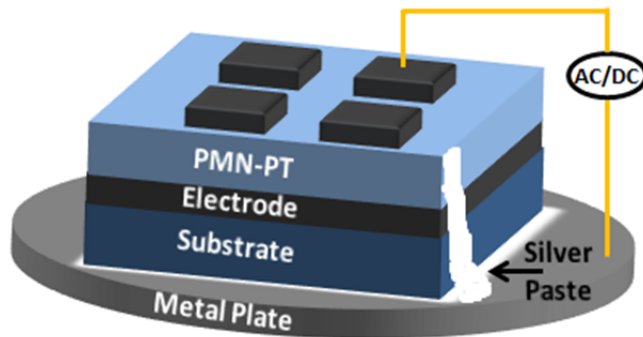


Figure 2.3: Schematic view of the sample glued on metal plate with electrical connections.

2.3 Characterization Techniques

2.3.1 Structural analysis

X-ray diffraction (XRD) is one of the widely used non-destructive techniques for the structural characterization of materials. The structural investigations reported in this dissertation were performed on high resolution X-rays diffraction (HR-XRD) either by Bruker D8 Discover or PANalytical X¹pert PRO MRD using Cu- α radiation source. The XRD technique is based on interference of the scattered X-rays from the crystal planes according to Bragg's law ($n\lambda=2d\sin\theta$). Structural properties of the fabricated heterostructures were studied by performing θ - 2θ scans, rocking curves (ω -scan), in-plane scans (ϕ -scans) and reciprocal space maps of the samples.

θ - 2θ scans also known as out-of-plane measurements are typically performed diffraction scans. These measurements provide information only about those planes which are parallel to the substrate surface. Information like out-of-plane lattice constants (d-spacing), phases purity, strain (peak shifts) and out-of-plane crystallographic orientation can be extracted from these scans. However, these measurements do not provide any information about those planes which are not oriented parallel to the substrate surface. To obtain the information about the other planes, one has to perform ϕ -scans commonly known as in-plane measurements. To perform ϕ -scans, the sample is moved in such a way that Bragg conditions are fulfilled for a specific set of planes. These scans can provide information about the in-plane alignment of the film with respect to the substrate, in-plane lattice constants, in-plane strain and in-plane orientations. To investigate the crystalline quality of the deposition material, rocking curves (ω -scans) are commonly recorded. In this scan, 2θ value is fixed and ω is varied to capture the in-plane distribution of diffracted intensities. Wider distribution means poor crystalline quality. Reciprocal space maps are very useful and provide variety of

information about the deposited films such as layer tilt, lattice relaxation, domain structure, crystalline quality, in and out of plane lattice constants etc. Lattice parameters reported in this work were extracted from reciprocal space maps.

2.3.2 Microstructure and morphological studies

The surface quality of the substrate is crucial for epitaxial thin film fabrication. Thin films with smooth surfaces/interfaces are highly desirable for multilayer device fabrication. Similarly, the microstructure of the deposited film has important consequences on the ferro and piezoelectric properties of ferroelectric oxide thin films. Considering this, surface morphology and microstructural investigations of the substrates and deposited films were performed by atomic force microscope (AFM) and high resolution scanning electron microscope (HR-SEM).

Atomic force microscopy (AFM) is one of the scanning probe microscopy techniques that can be used to analyse the surface properties of the substrates and the thin films. AFM studies reported in this dissertation were performed on Bruker Icon. This instrument is capable to analyse topography, conductivity, ferroelectric properties, piezoelectric properties, elastic properties, thermal properties and magnetic properties. The images reported in this thesis were acquired by operating the instrument either in contact mode or tapping mode. In contact mode operations, the cantilever tip constantly remains in contact with the sample surface during scanning. This imaging mode is heavily influenced by frictional forces due to strong tip sample interactions. This can damage the sample surface or distort the image data spatially in case of soft samples. Vertical deflection of the cantilever during scanning provides the dynamic feedback signal necessary to image the feature height on the sample surface. In tapping mode operation, the cantilever is oscillated at or near its resonance frequency. In this mode, forces between cantilever tip and sample surface cause a change in the initial resonance behavior. A

phase image can also be created by simultaneously monitoring the phase shift between drive signal to the cantilever and its response. The AFM setup is schematically shown in figure 2.4.

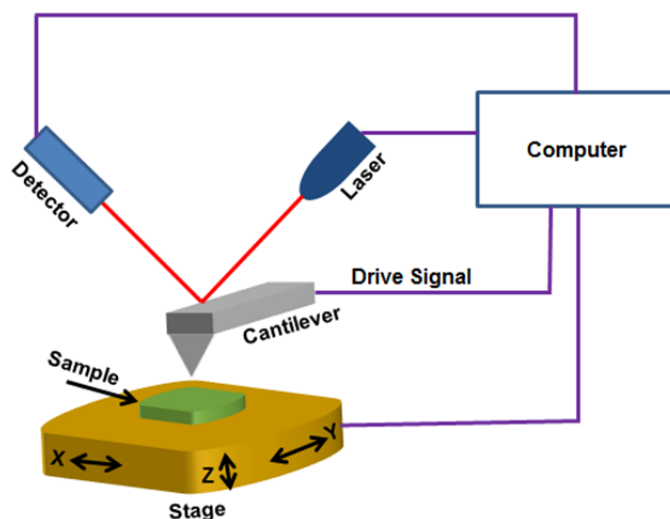


Figure 2.4: Simplest schematic view of the Atomic Force Microscope

Scanning electron microscopes (SEM) fall in the category of electron microscopes because they employ electrons for imaging instead of light. The scanning electron microscope images reported in this dissertation were taken by Zeiss Merlin HR-SEM. This instrument can be operated with an acceleration voltage ranging from 20V to 30kV and have point resolution of 0.9nm in STEM (scanning tunnelling electron microscope) mode, or 1.2nm in normal SEM mode working with acceleration voltage of 30kV. This SEM is equipped with a number of detectors capable of measuring clear topography (SE & SE-2), compositional and crystal orientation mapping (ASB), compositional contrast (ESB), elemental analysis (EDX), conductivity mapping (EBIC) and crystal orientation mapping (EBSD). The simplest schematic view of the scanning electron microscope is shown in figure 2.5.

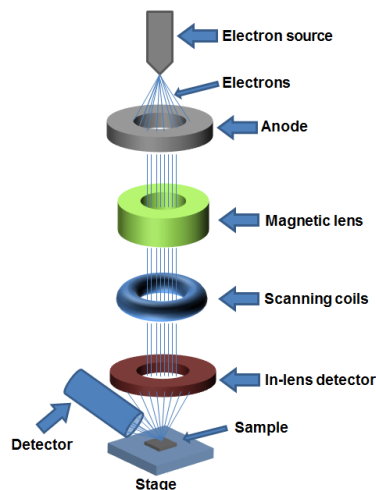


Figure 2.5: Schematic view of the scanning electron microscope

The electrons are emitted from the source (field emission gun in this case) and travel through the column that consists of anode, magnetic lenses and scanning coils placed in vacuum. This beam of electrons is used to scan the sample by scanning coils. Different kinds of interactions take place between the electron beam and the sample generating secondary electrons, back scattered electrons, characteristic x-rays etc. which are used to acquire the informations of interest. The interaction between primary electron beam and sample is schematically shown in figure 2.6.

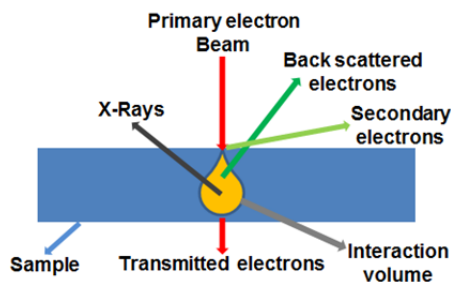


Figure 2.6: Schematic view of the electron and material interaction used for imaging in scanning electron microscope.

2.3.3 Electrical investigations

Polarization hysteresis (P-E) loops corresponding to out of plane polarization reported in this dissertation were measured by aixACCT TF Analyzer 3000. These measurements were performed using triangular wave of amplitude of ± 150 kV/cm at frequency of 1kHz. The schematic view of the saw-tooth waves and modified Sawyer Tower circuit used to measure the ferroelectric hysteresis (P-E) loops is shown in figure 2.7 [15].

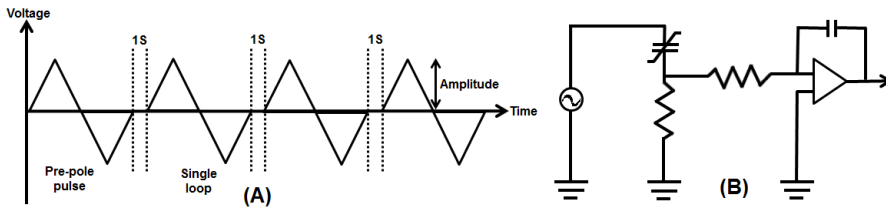


Figure 2.7: Schematic view of the saw-tooth wave used for hysteresis loop measurements (A) and modified Sawyer Tower circuit (B).

The typical result of polarization verses electric field measurements is a hysteresis curve demonstrating the characteristics of the measured material. The commonly used nomenclature for the evaluation of the measured data is described with the help of typical hysteresis curve shown in figure 2.8.

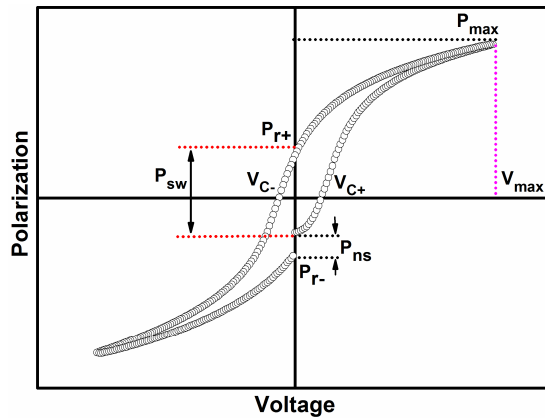


Figure 2.8: Schematic view of typical ferroelectric hysteresis curve.

Where

- P_{r+} : Positive remanent polarization
- P_{r-} : Negative remanent polarization
- V_{c+} : Positive coercive voltage
- V_{c-} : Negative coercive voltage
- P_{max-} : Saturation polarization
- V_{max-} : Saturation voltage
- P_{ns} : Non-switchable polarization
- P_{sw} : switchable polarization

To investigate the ferroelectric response stability, polarization switching behavior (fatigue) tests were performed. Fatigue refers to the change of the hysteresis loop (P-E) with the number of switching cycles the ferroelectric capacitor has gone through. The ferroelectric capacitors were switched multiple times and the influence of the amplitude and frequency excitation signal on fatigue behavior was investigated as the number of switching cycles increases. The saw-tooth wave form excitation signals are usually employed to record the ferroelectric hysteresis loops whereas the rectangular excitation pulses are typically employed to achieve highest amount of instantaneous switching during fatigue treatments. The fatigue treatment process is schematically illustrated in figure 2.9. This method starts with the measurement of the initial ferroelectric hysteresis loop followed by fatigue treatment steps. The fatigue treatment process is interrupted in regular intervals to record the ferroelectric hysteresis loops in such a way that a logarithmic plot of data points can be acquired with an equal spacing. Typically result of the fatigue measurements is a plot between remanent polarization (extracted from P-E loops recorded in-between fatigue treatment) versus the logarithm of the total number of switching cycles.

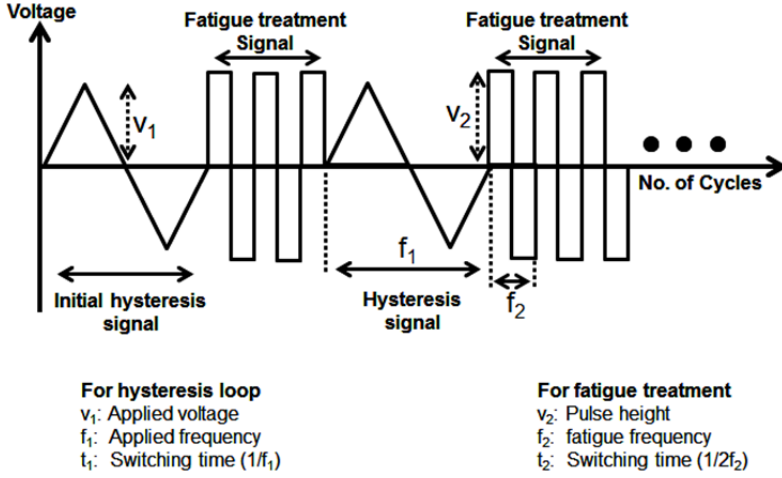


Figure 2.9: Schematic view of the fatigue treatment process.

Epitaxial PMN-PT films are sandwiched between metallic electrodes (SrRuO_3) to form a parallel plate ferroelectric capacitor. Capacitance of a parallel plate capacitor refers to charge stored in the ferroelectric capacitor. Capacitance verses electric field (C-E) measurements reported in this dissertation were performed using a Keithley 4200 semiconductor characterization system (Keithley Instruments GmbH, Germany). These measurements were performed in a frequency range of 10 kHz to 1 MHz by employing a small ac signal of 4kV/cm. The relation between capacitance and dielectric constant is given by.

$$\text{Dielectric Constant: } \varepsilon = \frac{Cd}{\varepsilon_0 A} \quad (2.1)$$

The correlation between capacitance and dielectric losses ($\tan\delta$) is given by.

$$\text{Dielectric loss: } \tan\delta = \frac{G}{2\pi fC} \quad (2.2)$$

Where

- ε : Permittivity of the material between the plates/electrodes (PMN-PT)
- C : Capacitance in Farads [F]
- d : PMN-PT film thickness in meters [m]

- ϵ_0 : Dielectric constant of free space [8.854×10^{-12} F/m]
- A : Area of the capacitor in square meters [m^2]
- G : Conductance in Siemens [S]
- f : Frequency in Hertz [Hz]

The leakage current is another important characteristics which affects the performance of ferroelectric material based devices and need to be studied. The leakage current investigations (J-E) reported in this dissertation were performed using a Keithley 4200 semiconductor characterization system (Keithley Instruments GmbH, Germany).

2.3.4 Electromechanical investigations

The piezoelectric properties of the epitaxial PMN-PT films and free standing cantilevers reported in this dissertation were measured with a Polytec MSA-400 Microsystem System Analyzer. This instrument is a combination of Scanning Laser Doppler Vibrometry, Stroboscopic Video Microscopy and White Light Interferometry. Laser Doppler Vibrometer (LDV) is a non-contact based instrument designed to measure out of plane vibrations [16-17]. The laser beam is directed towards the surface to be measured. Vibrations in the piezoelectric material induce changes in vibrational amplitude and frequency which can be detected through the Doppler shift of the laser beam. LDV is a Michelson interferometer based instrument that measures the difference in interference fringes which are caused by changes in length between the measured laser beam with respect to a reference laser beam [18]. This instrument can detect deformations with a resolution of roughly 5pm if good vibration filtering and a frequency higher than 500Hz are employed [19].

The laser doppler vibrometer utilizes a He-Ne laser operating at wavelength of 632.8nm. It is evident from figure 2.10 that the laser beam from the source is divided into two beams, one for measurement and other for reference. The measurement beam, after reflecting from

the vibrating sample, reaches the detector where it is combined with the reference beam to generate interference fringes. From the interference pattern, vibration frequency and amplitude can be deduced.

The longitudinal piezoelectric coefficients (d_{33}) were derived from piezoelectric hysteresis loops which were measured by connecting additional electronics with the LDV [20]. These measurements were performed by employing dc signal of amplitude ± 12 V at 8kHz frequency superimposed with a small ac-signal of 0.5 V. Basic Laser Doppler Vibrometer (LDV) setup is shown in the figure 2.10.

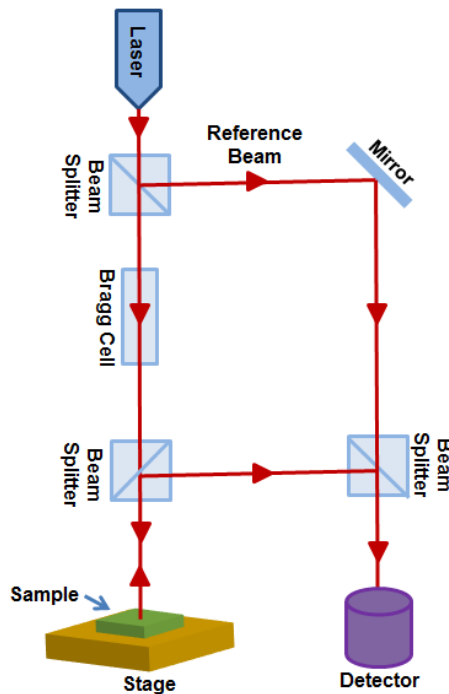


Figure 2.10: Schematic view of basic of Laser Doppler Vibrometer (LDV) setup

2.4 References

- [1] T. H. Maimon, *Nature*, 187 (1960) 493.
- [2] F. Breech and L. Cross, *Appl. Spectrosc.* 16 (1962) 59.
- [3] H. M. Smith and A. F. Turner, *Appl. Opt.* 4 (1965) 147.
- [4] H. Schwarz and H. A. Tourtellotte. *J. Vac. Sci Technol.* **6** (1968) 373.
- [5] A. Inam, M. S. Hegde, X. D. Wu, T. Venkatesan, P. England, P. F. Miceli, E.W. Chase, C. C. Chang, J. M. Tarascon, J. B. Wachtman, *Appl. Phys. Lett.*, 53, (1988) 908.
- [6] Robert Eason, Pulsed laser deposition of thin films: applications led growth of functional materials, John Wiley and Sons, Inc. New Jersey (2007).
- [7] G. Rijnders, G. Koster, D. H. A. Blank and H. Rogalla, *Appl. Phys. Lett.*, 70 (1997) 1888.
- [8] G. Koster, G. Rijnders, D. H. A. Blank and H. Rogalla, *Appl. Phys. Lett.*, 74 (1999) 3729.
- [9] F. Fahler and H. U. Krebs, *Appl. Surf. Sci.*, 61 (1996) 96-98.
- [10] Mark Huijben, Interface Engineering for oxide electronics, PhD Thesis, University of Twente, 2006. (ISBN: 90-365-2351-6)
- [11] S. E. Park, T. R. Shrout, *IEEE Trans. Ultrason. Ferroelectrictr. Freq. Control.* 44, (1997) 1140.
- [12] M. Ohring, *Material science of thin films*. Academic press, London, 2nd Edition, 2002.
- [13] S. Horita, T. Naruse, M. Watanabe, A. Masuda, T. Kawada, Y. Abe, *Appl. Surf. Sci.*, 117–118 (1997) 429.
- [14] P. Maitri, Warusawithana, C. R. Sleasman, J. C. Woicik, Y. Li, L. F. Kourkoutis, J. A. Klug, H. Li, P. Ryan, L. P. Wang, M. Bedzyk, D. A. Muller, L. Q. Chen, J. Levy, D. G. Schlom, *Science*, 324 (2009) 367.
- [15] Y. T. Tsui, P. D. Hinderaker and F. J. Mcfadden, , *Rev. Sci. Instrum.* 39 (1968) 1423.
- [16] W. Y. Pan, L. E. Cross, *Rev. Sci. Instrum.* 60 (1989) 2701.

- [17] A. L. Kholkin, Ch. Wutrich, D. V. Taylor, and N. Setter, Rev. Sci. Instrum. 67 (1996) 1935.
- [18] Z. Haung, G. Leighton, R. Wright, F. Duval, H. C. Chung, P. Kirby and R. W. Whatmore, Sens. Act. A., 135 (2007) 660.
- [19] A. L. kholkin, C. Wutrich, D. V. Taylor and N. Setter, Rev. Sci. Instrum., 67 (1996) 1935.
- [20] Minh Duc Nguyen, Ferroelectric and piezoelectric properties of epitaxial PZT films and devices on silicon, PhD Thesis, University of Twente, 2010. (ISBN: 978-90-365-3047-7)

3.

Processing of PMN-PT films

Chapter Overview:

This chapter describes the growth of perovskite phase and (001) orientation pure epitaxial PMN-PT thin films on SrRuO₃ electroded SrTiO₃ substrates. The effect of fabrication conditions like laser energy density (fluency), substrate temperature, target to substrate distance and deposition pressure on phase formation was investigated in detail. Within relatively narrow processing window to achieve phase and orientation pure films, the effect of growth conditions on ferroelectric and piezoelectric properties of these films was studied.

This chapter to be submitted as:

- Optimization of the growth of epitaxial PMN-PT thin films on (001) SrTiO₃ substrates.

3.1 Introduction

Micro-electromechanical systems (MEMS) based on ferroelectric oxides are among the highest performing devices for the purpose of sensing and actuation. Lead zirconium titanate ($\text{PbZr}_{1-x}\text{Ti}_x\text{O}_3$ or PZT) is one of the frequently employed piezoelectric materials for the fabrication of such devices [1-2].

An alternate to PZT are relaxor ferroelectrics like (PMN-PT), (PZN-PT) etc. which are solid solutions between a relaxor (PMN or PZN) and a ferroelectric material (PT). Recent developments in relaxor ferroelectrics yielding giant piezoelectric response compared to the well-known piezoelectric material PZT have propelled them to the forefront for sensors and actuators research and development. Park and Shrout reported ultrahigh strain in $[\text{Pb}(\text{Mg}_{1/3}\text{Nb}_{2/3})\text{O}_3]_{67-}(\text{PbTiO}_3)_{33}$ and $[\text{Pb}(\text{Zn}_{1/3}\text{Nb}_{2/3})\text{O}_3]_{91-}(\text{PbTiO}_3)_{09}$ bulk single crystals oriented and poled in the (001) direction. Specifically PMN-PT (67/33) shows a record high piezo-electric coefficient $d_{33} \approx 2500 \text{ pm/V}$ [3]. In addition these materials exhibit significantly higher coupling coefficients ($k_{33} \approx 0.9$) than bulk PZT ceramics. Due to their superior properties, devices fabricated from these materials may generate large strains for small applied field or vice versa be sensitive to very small strain [3-4].

PMN-PT is a crystalline solid solution of a typical relaxor (PMN) and a classic ferroelectric material (PT). In many ferroelectric solid solutions, the dielectric and piezoelectric properties are maximized at the morphotropic phase boundary. This morphotropic phase boundary occurs at 33 percent of PT in the bulk PMN-PT solid solution system. Nevertheless thin film boundary conditions like clamping to the substrate can modify the morphotropic phase boundary. This behavior is not entirely clear for epitaxial PMN-PT thin films. Giant piezo response up to 1.7% , an order of magnitude higher than for bulk PZT ceramics, was observed for (001) oriented PMN-PT (67/33) single crystal. This ultra-high strain in PMN-PT

single crystals is attributed to electric field induced phase transformations from the rhombohedral to the tetragonal phase. Furthermore, the high coupling coefficient ($k_{33} > 0.9$) and low dielectric losses ($<1\%$) make this material a promising candidate for the fabrication of new generation sensors and actuators [3].

For many applications, one requires PMN-PT in thin film form instead of bulk single crystals. This necessity initiated efforts to synthesize this hyperactive material in thin film form. Epitaxial films are highly desirable compared to polycrystalline films due to a lower leakage current and higher piezo response [5-6]. The growth of high quality epitaxial PMN-PT films is known to be difficult because of the relatively poor thermodynamic stability of the perovskite phase and compositional complexity. The prominent, stable pyrochlore phases like cubic $\text{Pb}_3\text{Nb}_4\text{O}_{13}$, rhombohedral $\text{Pb}_2\text{Nb}_2\text{O}_7$ and tetragonal $\text{Pb}_3\text{Nb}_2\text{O}_8$ appear during growth. These non-piezoelectric phases cause degradation of the functional properties of the deposited films [7-8]. Additionally, the properties of PMN-PT films are sensitive to film stoichiometry and all five elements should be in exact stoichiometry to achieve good properties. Off stoichiometry not only degrades the film properties but also can cause the formation of impurity phases (pyrochlore phases). For instance, epitaxial films are usually deposited at high substrate temperature which may result into lead loss due to its high volatility. Lead loss not only promotes higher leakage current but also can cause the formation of lead deficient pyrochlore phases. It is noticed that PMN-PT is commonly preferred over PZN-PT, since the later contains two volatile elements (Zn and Pb) although both exhibit superior properties compared to the prominent (PZT) ferroelectric material. Besides the lead stoichiometry, the Mg/Nb ratio is also found essential to fabricate perovskite phase pure PMN-PT films [9].

A number of methods and approaches has been adopted to fabricate high quality PMN-PT material. For instance, the columbite process was developed by S. L. Swartz and T. R. Shrout in 1982 for the synthesis of bulk PMN-PT ceramics. This process bypasses the pyrochlore phase formation by facilitating the reaction between MgO

and NbO prior to the addition of and reaction with PbO [10]. Nonetheless, this method is not useful for thin film growth. Maria and co-workers were the first who successfully deposited epitaxial PMN-PT (70/30) thin films, using pulsed laser deposition (PLD) on LaAlO_3 substrates. They achieved perovskite phase pure epitaxial PMN-PT(70/30) films by carefully controlling the fabrication conditions. [11]. Subsequently S. D. Bu et al. adopted the approach of miscut SrTiO_3 (STO) substrates to achieve perovskite phase pure epitaxial PMN-PT(67/33) films. The high density of steps on the miscut substrate surface was thought to promote the growth of the perovskite phase by facilitating the incorporation of volatile PbO into the film. [12]. Afterward S. H. Baek et al. demonstrated the fabrication of high quality epitaxial PMN-PT(67/33) films with giant piezo response on SrTiO_3 buffered miscut silicon substrates [20]. High quality epitaxial PMN-PT films have been deposited using metal-organic chemical vapor deposition, sputtering and pulsed laser deposition [11-14].

From the literature, it is clear that the deposition of high quality PMN-PT films is very sensitive to the deposition conditions and only a very narrow process window exists. Further within this window the piezo and ferroelectric properties of the films are varying strongly with the exact process conditions. It is therefore important to establish the process window (which is clearly somewhat specific for the deposition equipment used) and the (qualitative) relation with the properties.

In the first section of this chapter we describe the optimization of the growth of epitaxial PMN-PT thin films on STO substrates by varying the deposition conditions and find a very narrow process window for phase-pure growth. In the second part the variation of the ferroelectric properties within this process window is investigated.

3.2 Experimental Procedure

3.2.1 Samples fabrication

For this study (001) oriented STO substrates with B-site termination were used for their well-defined crystalline surface and close lattice match to the thin films. The STO substrates were pre-treated to achieve B-site termination using method developed by Koster and co-workers [24]. 100nm thick SrRuO_3 (SRO) thin films were deposited as top and bottom electrodes, because SRO can grow uniformly on a TiO_2 terminated STO substrate with a high crystalline quality [17]. Secondly the use of oxide electrodes is very beneficial for the long-term stability of ferroelectric oxides, as compared to metal electrodes [18,19]. For the ferroelectric the PMN-PT(67/33) composition was selected because of its giant piezoelectricity in thin film form on STO-buffered silicon demonstrated in ref.[20]. All films have been deposited with Pulsed Laser Deposition (PLD) using a KrF Excimer laser operating at 248nm, using commercial targets on a heated substrate. The deposition conditions are given in table 3.1.

Table 3.1: Growth conditions of SRO electrodes and PMN-PT films on STO(001) substrate. (In brackets the initial conditions used prior to the optimization)

Parameters	SrRuO_3	PMN-PT
Gas	Oxygen	Oxygen
Pressure p (mbar)	0.130	0.158 – 0.318 (0.278)
Laser fluency F (J/cm^2)	2.50	2.0 – 2.5 (2.5)
Laser repetition rate (Hz)	4	4
Substrate temperature T ($^\circ\text{C}$)	600	550 – 625 (575)
Target-Substrate distance D (cm)	4.90	5.5 – 6.5 (5.5)
Film thickness t (nm)	100	300

The complete SRO/PMN-PT/SRO heterostructure was deposited without breaking the vacuum. After deposition the samples were cooled down to room temperature in a pure, 1 bar oxygen

atmosphere during one hour (cooling rate = $10^{\circ}\text{C}/\text{minute}$). The growth conditions SRO electrode are given in table 3.1. The PMN-PT the deposition conditions were varied around a set of conditions used for $\text{Pb}(\text{Zr}_{1-x}\text{Ti}_x)\text{O}_3$.

3.2.2 Samples characterization

Structural properties and epitaxial relationships were investigated by High Resolution X-Ray Diffraction (Bruker D8 Discover). The lattice parameters were obtained from reciprocal space maps. The surface morphology and cross-sectional images were measured with atomic force microscopy (Bruker Icon) and high resolution scanning electron microscopy (Zeiss Merlin HR-SEM). Ferroelectric capacitor structures ($200 \times 200 \mu\text{m}^2$) were patterned with a standard photolithography process and structured by argon ion beam etching. Polarisation-electric field (P - E) hysteresis loops were measured using a modified Sawyer Tower circuit (AixACCT TF Analyser 2000) at a scan frequency of 1kHz using a bipolar triangular pulse with an amplitude of 170 kV/cm. Fatigue measurements were performed using a rectangular pulse train at a frequency of 10 kHz and an amplitude of 170 kV/cm. The longitudinal piezoelectric coefficients (d_{33}) were obtained with the Polytec MSA-400 Micro Scanning Laser Doppler Vibrometer. Capacitance versus electric field vs. capacitance (C - E) curves were measured with a Keithley 4200 at 10kHz frequency.

3.3 Results and discussions

3.3.1 Phase optimization and structural properties

In the first optimization step the laser fluence was optimized to achieve uniform ablation of the target material to avoid droplet formation in the plasma plume, which can be incorporated in the growing film. No droplet formation was found in the range $F = 1.5 -$

2.5 J/cm^2 , consistent with frequently employed values found in literature [7,9,11]. Figure 3.1 shows the θ - 2θ scan of the samples deposited at a fluence $F = 2.0, 2.25$ (sample P1) and 2.5 J/cm^2 , keeping the other deposition conditions equal to the initial conditions given in table 3.1.

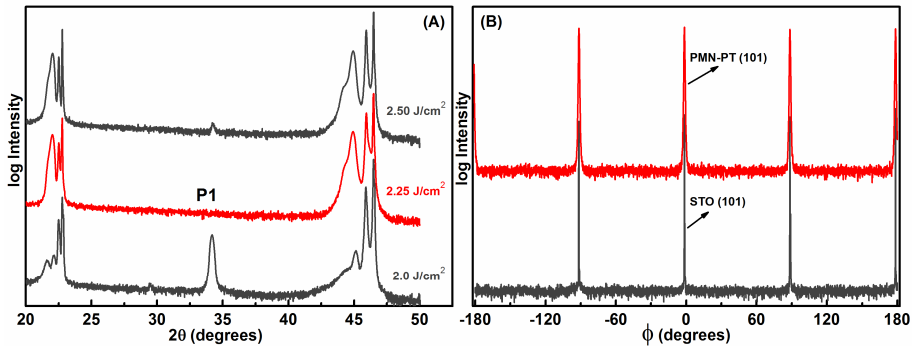


Figure 3.1: Diffraction pattern of epitaxial PMN-PT films deposited with different laser fluency (a) ϕ scans of the PMN-PT (101) reflection and the STO substrate (101) reflection of sample P1, showing cube-on-cube epitaxial relation with the substrate.

The extra diffraction peaks at approximately 34° in the samples made with a fluence of 2.0 and 2.5 J/cm^2 are due to the pyrochlore phase ($\text{Pb}_3\text{Nb}_4\text{O}_{13}$), which is caused by a lead deficiency in the film. For the high fluence case this may be ascribed to re-evaporation of PbO from the substrate, due to the energetic bombardment by atoms and ions from the plasma [7]. In the low fluence case it is assumed that the PbO particles do not have enough kinetic energy to reach the substrate in sufficient amount. In both cases the optimum film stoichiometry is lost. The perovskite phase and (001) orientation pure film P1 was analysed further. The azimuthal ϕ -scan of the PMN-PT (101) reflection of this film shows in-plane epitaxy with a cube-on-cube epitaxial relation with the STO substrate. The full width at half maximum (FWHM) of the ω -scan of the PMN-PT (002) reflection is 0.53° , and a broad shoulder of this

reflection is observed at lower angles in the θ - 2θ scan. This indicates that part of the film is in-plane compressively strained, as may be expected from the lattice mismatch of the film (the literature value of the pseudo-cubic lattice constant of PMN-PT is $a_{\text{PMN-PT}} = 4.022 \text{ \AA}$ [20]) with the substrate ($a_{\text{STO}} = 3.905 \text{ \AA}$). The main diffraction peak corresponds to a PMN-PT out-of-plane lattice parameter of $c = 4.034 \text{ \AA}$, whereas the maximum of the shoulder due to the strained layer corresponds to $c_{\text{str}} = 4.091 \text{ \AA}$. From the reciprocal space map the out-of-plane and in-plane lattice parameters c and a were determined, from which a c/a ratio equal to 1.0057 and a pseudocubic lattice parameter (defined as $a_{\text{pc}} = (ca^2)^{1/3}$, of 4.024 \AA were calculated. Thus the bulk of the film is largely relaxed and has a pseudo-cubic lattice parameter practically equal to that of the rhombohedral phase of PMN-PT(67/33) single crystals [20].

Table 3.2: Summary of deposition conditions and structural properties of the perovskite phase and (001) orientation pure epitaxial PMN-PT films fabricated during optimization process. The F , D , T , P and t corresponds to fluency, target-substrate distance, deposition temperature, deposition pressure and film thickness respectively.

Sample	Deposition				Structure (PMN-PT)				
	F (J/cm^2)	D (cm)	T ($^{\circ}\text{C}$)	P (mbar)	a_{pc} (\AA)	c/a	$FWHM$ (002)	t (nm)	$Roughness$ (R_a) nm
P1	2.25	5.5	575	0.278	4.024	1.0057	0.53	300	1.80
P2	2.25	5.5	600	0.278	4.026	1.0035	0.50	300	0.78
P3	2.25	6.0	600	0.278	4.025	1.0045	0.48	300	0.78
P4	2.25	6.0	600	0.238	4.027	1.0052	0.44	300	0.55
P5	2.25	6.0	600	0.198	4.031	1.0060	0.60	300	0.90

Maintaining the other deposition parameters the same as for sample P1, the substrate temperature was changed to 550, 600 (sample P2) and 625 $^{\circ}\text{C}$. Figure 3.2(a) shows the θ - 2θ scan of these samples. For $T = 550$ and $625 \text{ }^{\circ}\text{C}$ the pyrochlore phase appears again as well as a large increase of the shoulder of the (002) reflection, whereas for $T \geq 600 \text{ }^{\circ}\text{C}$ also peaks corresponding to PbO show up. The shoulder on

the (002) reflection and the FWHM of the (002) ω -scan slightly decrease when the substrate temperature is increased to 600 °C. The lattice parameters of sample P2 are within the error margins equal to that of P1 (see table3.2), however the film is slightly PbO enriched.

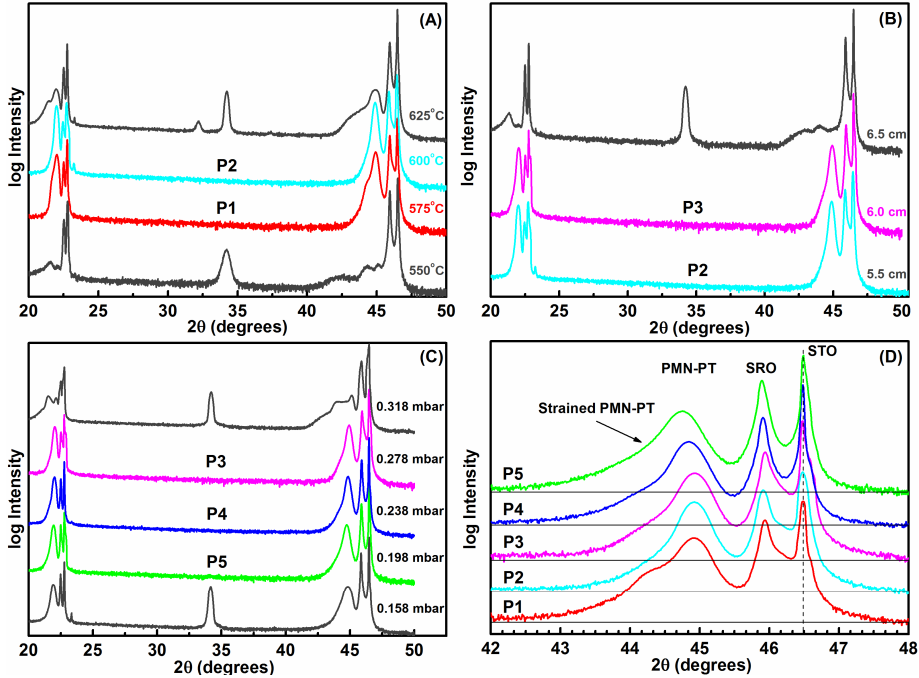


Figure 3.2: (a) Diffraction pattern of PMN-PT films deposited at different substrate temperatures T . The other deposition parameters are those of sample P1. (b) Idem for different target to substrate distances D , with the other parameters equal to those of P2. (c) Idem for different deposition pressures p , with the other parameters equal to those of P3. (d) Detail of the diffraction pattern of the PMN-PT (002) reflections of the samples P1-5 showing the variation in shoulders.

The adjustment of the Pb stoichiometry was accomplished by changing the target-substrate distance D , which is believed to influence the scattering chance of the incoming Pb and PbO particles. Secondly, a larger distance is expected to improve the surface smoothness, due to a reduction of the energy of the incoming particles. Figure 3.2(b) shows the θ - 2θ scans of samples fabricated

with the conditions of sample P2, but with a target-substrate distance of 6.0 and 6.5 cm. For $D = 6.0\text{cm}$ (sample P3) no PbO reflection is observed and the scan does not show any sign of any other phase than pure (001) oriented PMN-PT, whereas for $D = 6.5\text{cm}$ strong pyrochlore phase reflections are present. For P3 there is hardly any effect on the shoulder of the (002) reflection, compared to sample P2, and the lattice parameters are nearly equal to that of P1 and P2. However, no improvement in surface roughness is observed and is similar to P3 below 1 nm (See table 3.2). It is important to note that roughness reported in table 3.2 is the roughness of the PMN-PT film without top electrode. The deposition of SrRuO_3 top electrode further smoothen the surface and decrease the surface roughness.

The deposition pressure has also an important effect on the crystal structure when growing films at high substrate temperature. For example Catalan et al. reported the influence of oxygen partial pressure on the electromechanical properties for PLD deposited PMN films [27-28]. Using the deposition conditions of sample P3, the deposition pressure was varied in the range $p = 0.158\text{-}0.318$ mbar. For low pressure $p = 0.158$ mbar both the pyrochlore and the PbO phase are present in the XRD scans (fig. 3.2c), whereas for the highest pressure the pyrochlore phase is observed. In the narrow intermediate pressure range $p = 0.198\text{-}0.278$ mbar no spurious phases are observed and smooth films are obtained. The lowest FWHM (002) = 0.44° was obtained for $p = 0.238$ mbar (sample P4).

In conclusion of this section: phase pure, (001) oriented, smooth, 300nm thick PMN-PT films were obtained in a narrow window of deposition conditions, $p = 0.198 - 0.278\text{mbar}$, $T \approx 575 - 600^\circ\text{C}$, $F = 2.25 \text{ J/cm}^2$, $D = 5.5 - 6.0\text{cm}$.

3.3.2 Ferroelectric and piezoelectric properties

For all samples that showed no spurious crystal phases the polarisation loops of capacitor devices were measured. Figure 3.3(a) shows the loops of the devices (P1 – P5). All loops show the

characteristic slanting of relaxor type films. A second common feature is the shift of all loops due to a positive field bias. As a characteristic polarization parameter we use the average out-of plane component of the spontaneous polarizations $|P_{s3}|$ estimated from the extrapolated value $P_{ex}(E_{sb})$ of the tangents at the loop at the applied field strength $E=(\pm 120+E_{sb})$ kV/cm of the decreasing (increasing) section of the loop, where the switching is nearly complete and above (below) which the loops become approximately linearly depending on the field. This parameter is a measure for the fraction of the spontaneous polarization that is not affected by screening or strain induced rotation of the polarization vector away from the $[<111>]$ easy axes of a (001) oriented, unstrained single crystal.

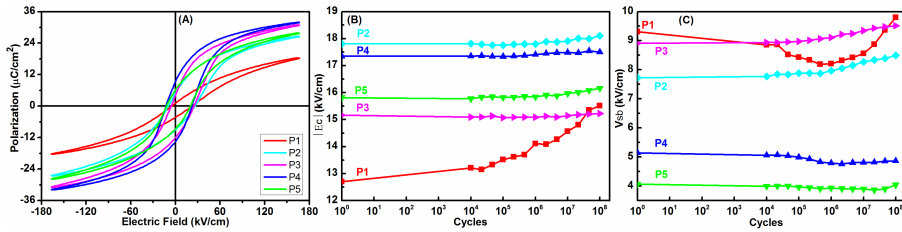


Figure 3.3: (a) polarization hysteresis loops of the samples P1-5; (b) Coercive field and (c) self-bias field during aging.

Figure 3.4 shows P_{ex} as function of deposition pressure p . There is a shallow maximum for $p=0.238$ mbar. The investigated changes of the fluence or substrate target distance at $p=0.278$ mbar result in a lower polarization value. The maximum value of 0.29 C/cm² of P4, is close to the value expected for the out-of-plane component of the spontaneous polarization directed along the body diagonal of the rhombohedral distorted pseudocubic lattice of single crystal PMN-PT, $P_{s3} = P_s/\sqrt{3}=0.32$ C/m². The lower values for the other samples are ascribed to increased screening by charged defects, for example in grain boundaries, or by more rotation of the polarization vector towards the film plane due to strain. The latter seems less likely, considering the observation that for all films the

lattice is slightly tetragonal, with the long axis in the out-of-plane direction, which would give an increased P_{s3} instead of a decreased value. Therefore we believe that the differences are mainly due to differences in screening and thus to the defect concentration. The polarization vector in a relaxor material can easily rotate under influence of external influences, hence the presence of for example charged grain boundaries is expected to have a significant reducing effect on the measured polarization value. To estimate the relative effect of the different deposition parameters on the polarization value $P(0)$ in the regime in which smooth, phase pure films are obtained, the normalized parameter sensitivities S are estimated as,

$$S_p = \left(p_{av} \frac{\Delta P_{s3}}{\Delta p} \right)_{F,T,D}, \quad S_T = \left(T_{av} \frac{\Delta P_{s3}}{\Delta T} \right)_{p,F,D}, \quad S_D = \left(D_{av} \frac{\Delta P_{s3}}{\Delta D} \right)_{p,F,T},$$

$$S_F = \left(F_{av} \frac{\Delta P_{s3}}{\Delta F} \right)_{p,T,D}$$

Here the average and the gradient are taken over the maximum differences of the measured $P(0)$ values of the dataset P1-5, for which the other deposition conditions are (nearly) constant. We find $S_p=0.34$, $S_T=1.76$, $S_D=1.16$, $S_F=0.50$ ($(C/m^2)/\%change$), hence change in the substrate temperature has the largest relative effect on P_{s3} , followed by the variation of the target-substrate distance. The system is least sensitive to pressure variations, as long as one is in the (narrow) range of deposition conditions that allows phase-pure growth of smooth films. The number of samples is limited and the above numbers therefore are only qualitative indications of the sensitivities relative to each other. However we think that the observed trends are systematic and are related to small changes in the crystal structure, and especially in the quality of the grain boundaries.

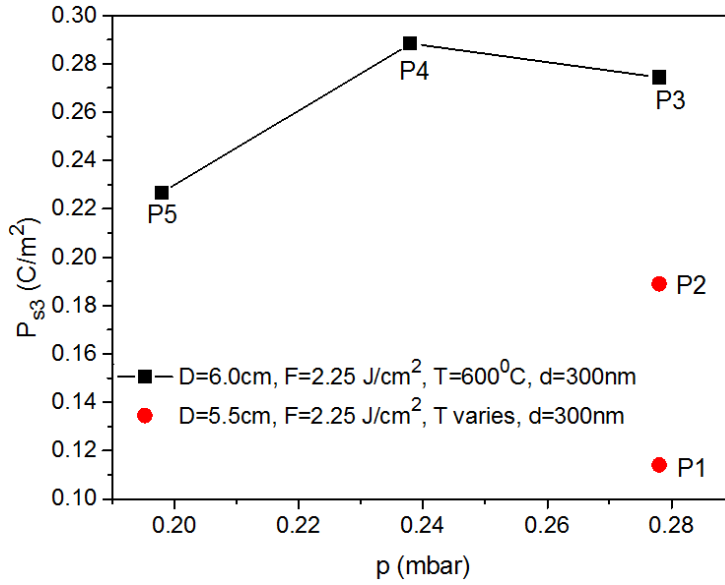


Figure 3.4: P_{33} of 300nm thick PMN-PT films on STO, as function of deposition pressure (p), varying target-substrate distance (D), substrate temperature (T) and fluence (F).

This extreme sensitivity is also reflected in the large variation of the zero-field relative dielectric constant with a factor 2, between 975 and 1806 (these values are close to the maximum values at $E=E_{sb}$ for the samples P1-5, although the high field values drop off to the range 400-500 at $E=200\text{kV/cm}$ for all samples. On the other hand the maximum effective piezoelectric constant $d_{33,\text{eff}}$ hardly depends on the deposition conditions and varies between 46 and 54 pm/V, but the loops are field-shifted with a magnitude approximately equal to that of the PE-loops.

In figure 3.3b and 3.3c the average coercive field $E_c = (E_c^+ - E_c^-)/2$ and the self-bias field $E_{sb} = (E_c^+ + E_c^-)/2$ are shown as function of the number of fatigue cycles. Apart from sample P1, which shows a steady increase of E_c with cycling, indicative for an increase of the domain wall pinning, thus probably of the (charged) defect density, all other films are very stable up to the maximum

number of cycles. In reference [33] the self-bias in PMN-PT capacitor devices grown on 25nm thick PZT seed layers of different compositions was discussed. There it was shown that the observed very large self-bias (up to 101 kV/cm) could be related to a strain gradient layer in the PZT seed layer. In the case of the 200nm thick PMN-PT film without PZT seed layer (S0) discussed in that reference, it was argued that the effect of the strain gradient in the PMN-PT layer was largely cancelled by the incorporation of free charge. The data suggested that this free charge was introduced in the film immediately after deposition in the case of S0, whereas for the devices with PZT seed layer it was slowly incorporated during cycling, resulting in a decreasing self-bias. Here we see that E_{sb} and E_c of sample P1,2,3 and P5 are somewhat changing with cycling, which is interpreted as being due to a change of the mobile charge distribution in the (grain boundaries) of the film. It is noted that the polarization values hardly change upon cycling, except for a shift of the loop due to a changing self-bias field, and changing/opening of the hysteresis loops, due to a changing coercive field. Sample P4 is the most stable upon cycling. This is also the sample with the highest polarization value P_{s3} , close to that expected for a single crystal film, without screening by charged grain boundaries. These findings suggest that the deposition conditions for P4 are close to the best that can be achieved with the PLD system used.

The ferroelectric, dielectric and piezoelectric properties of the samples P1 – P5 are summarized in table 3.3. The difference in dielectrics constants (max and @0V) is due to self-bias which reduces the relative permittivity at zero volt by shifting the electric field verses relative dielectric constant curves. Similarly the difference in longitudinal piezoelectric coefficient (max and average) is due to self-bias which enhances the response in preferential direction.

Table 3.3: Summary of the ferroelectric, dielectric and piezoelectric properties of perovskite phase and (001) orientation pure sample (P1-P5) deposited during phase optimization steps.

Sample	Polarization			Dielectric Constant		$d_{33,eff.}$	
	P_{s3} (C/m ²)	E_{sb} (kV/cm)	$ Ec $ kV/cm	ϵ_r (max)	ϵ_r @0V	$d_{33,eff.}$ (max)	$d_{33,eff.}$ (av.)
P1	0.11	8.6	13.6	886	975	51	49
P2	0.19	8.3	18.0	1399	1341	57	53
P3	0.27	9.4	15.3	1917	1806	55	49
P4	0.29	4.7	17.4	1529	1483	47	46
P5	0.23	4.0	16.1	1622	1587	46	45

3.3.3 Surface morphology and microstructure

Surface morphology and microstructure of epitaxial PMN-PT film at optimum deposition condition on SrRuO₃ electroded and TiO₂ B-site terminated SrTiO₃ substrate is shown in figure 3.5.

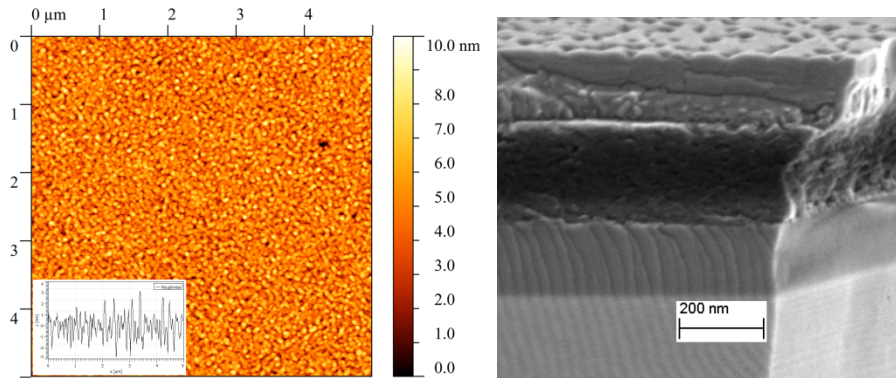


Figure 3.5: AFM image showing surface morphology of the PMN-PT film (left). HRSEM crosssectional image of sandwiched PMN-PT film (dark) between SrRuO₃ electrodes (right).

It is important to mention here that AFM image (left) is without top electrode showing the morphology of the PMN-PT film. The surface roughness (R_a , av.) is 0.78 nm demonstrating very smooth growth of PMN-PT film on SrRuO₃ bottom electrode. The

HRSEM image (left) showing dense microstructure of the PMN-PT film.

3.4 Conclusions

The growth of PMN-PT 300nm thick thin films by pulsed laser deposition on a STO(001) substrate with SRO electrodes was optimized with respect to phase purity and smoothness of the film, by varying the deposition conditions, the substrate temperature, laser fluence, oxygen background gas pressure and substrate-target distance. A narrow parameter regime was found in which phase pure and smooth films were obtained. The properties of the polarization hysteresis loop of devices made with growth conditions in this regime were investigated. In the optimized parameter regime the polarization value is most sensitive to variations in the substrate temperature, then to substrate-target distance and much less to fluence and least to gas pressure. The highest polarization value at the self-bias field, extrapolated from the loop at high fields, corresponds well to the value expected for rhombohedrally distorted pseudocubic lattice of PMN-PT, with a $\langle 111 \rangle$ easy axis.

The variation of the coercive field, and the self-bias field during cycling is small (approximately 0.5 kV/cm) , except for the sample P1 for which both substrate temperature and substrate-target distance are both not optimal and the variation is of the order of 2-3 kV/cm.

The PMN-PT film discussed in this chapter are inferior in terms of crystallinity compared to bulk PMN-PT single crystals. The crystallinity of these film can be improved using buffer layer having superior in-plane lattice matching with PMN-PT film. One of the suitable candidate for this purpose is PZT which have superior in-plane lattice matching with PMN-PT compared to SRO-PMN-PT layer stack. The deposition of PZT (50/50) buffer layer in-between SRO-PMN-PT film expected to improve crystallinity for PMN-PT films.

3.5 References

- [1] D. Isarakorn, A. Sambri, P. Janphuang, D. Briand, S. Gariglio, J. M. Triscone, F. Guy, J. W Reiner, C. H. Ahn and N. F. de Rooij, *J. Micromech. Microeng.* 20 (2010) 055008.
- [2] M. D. Nguyen, H. N. Vu, D. H. A. Blank, G. Rijnders, *Adv. Nat. Sci. Nanosci. Nanotechnol.*, 2 (2011) 015005.
- [3] S. E. Park and T. R. Shrout, *J. Appl. Phys.*, 82 (1997) 1804
- [4] S. E. Park and T. R. Shrout, *IEEE Trans. Ultrason. Ferroelectr. Freq. Control*, 44 (1997) 1140.
- [5] R. Ramesh , D. G. Schlom , *Science*, 296 (2002) 1975.
- [6] D. Akai , M. Yokawa , K. Hirabayashi , K. Matsushita , K. Sawada , M. Ishida , *Appl. Phys. Lett.*, 86 (2005) 202906.
- [7] D. Lavric, R. A. Rao, Q. Gan, J. J. Krajewski, and C. B. Eom, *Integr. Ferroelectr.*, 21 (1998) 499.
- [8] T. R. Shrout , A. Halliyal , *Am. Ceram. Soc. Bull.*, 66 (1987) 704.
- [9] C. Tantigate, J. Lee and A. Safari, *Appl. Phys. Lett.*, 66 (13) (1995) 1611.
- [10] S. L. Swartz and T. R. Shrout, *MRS Bull.*, 17 (1982) 1245.
- [11] J. P. Maria, W. Hackenberger and S. Trolier-McKinstry, *J. Appl. Phys.*, 84 (1998) 5147.
- [12] S. D. Bu, M. K. Lee, and C. B. Eom, *Appl. Phys. Lett.*, 79 (2001) 3482.
- [13] T. Ohnishi, K. Shibuya, M. Lippmaa, D. Kobayashi, H. Kumigashira, M. Oshima, and H. Koinuma, *Appl. Phys. Lett.*, 85 (2004) 272.
- [14] J. G. Connell, B. J. Isaac, G. B. Ekanayake, D. R. Strachan, and S. S. A. Seo, *Appl. Phys. Lett.*, 101 (2012) 251607.
- [15] G. J. Rijnders, G. Koster, D. H. Blank, and H. Rogalla, *Materials Science and Engineering: B* 56 (1998) 223.
- [16] R. Bachelet, F. Sánchez, F. J. Palomares, C. Ocal, and J. Fontcuberta, *Appl. Phys. Lett.*, 95 (2009) 141915.

- [17] G. Rijnders, D. H. A. Blank, J. Choi, and C. B. Eom, , Appl. Phys. Lett., 84 (2004) 505.
- [18] D. C. Worledge and T. H. Geballe, Phys. Rev. Lett., 85 (2000) 5182.
- [19] C. B. Eom, R. B. Van Dover, J. M. Phillips, D. J. Weder, J. H. Marshall and C.H. Chen, Appl. Phys. Lett., 63 (1993) 2570.
- [20] S. H. Baek, J. Park, D. M. Kim, S. D. Bu,... and C. B. Eom, Science, 334 (2011) 958.
- [21] S. Stemmer, G. R. Bai, N. D. Browning, and S. K. Streiffer, J. Appl. Phys., 87 (2000) 3526.
- [22] G. R. Bai, S. K. Streiffer, P. K. Baumann, S. Stemmer, O. Auciello, K. Ghosh, A. Munkholm, C. Thompson, R. A. Rao, and C. B. Eom, Appl. Phys. Lett., 76 (2000) 3106.
- [23] J. Wang, K. H. Wong, H. L. W. Chan, C. L. Choy, Appl. Phys. A, 79 (2004) 551.
- [24] G. Koster, B. L. Kropman, G. J. H. M. Rijnders, D. H. A. Blank, and H. Rogalla, Appl. Phys. Lett., 73 (1998) 2920.
- [25] S. L. Swartz and T. R. Shrout, MRS Bull., 17 (1982) 1245.
- [26] D. L. Smith, Thin Film Deposition (McGraw-Hill, New York, 1995).
- [27] X. S. Gao, J. M. Xue, J. Li, C. K. Ong and J. Wang, Microelectronic Engineering, 66 (2003) 926.
- [28] G. Catalan, M. H. Corbett, R. M. Bowman, and J. M. Gregg, Appl. Phys. Lett., 74 (1999) 3035.
- [29] N. Y. Lee, T. Sekine, Y. Ito and K. Uchino, Jpn. J. Appl. Phys., 33 (1994) 1484.
- [30] R. G. Polcawich, S. Troler-McKinstry, J. Mater. Res., 15 (2000) 2505.
- [31] R. G. Polcawich et al., IEEE Trans. Microwave Theory Tec., 55 (2007) 2642.
- [32] J. F. Scott, Ferroelectric Memories, Springer, New York, 2000
- [33] M. Boota, E. P. Houwman, M. Dekkers, M. D. Nguyen and G. Rijnders, Appl. Phys. Lett., 104 (2014) 182909.

4.

PMN-PT films on PZT interfacial layer

Chapter Overview:

Perovskite phase and (001) orientation pure epitaxial PMN-PT (67/33) films are fabricated on a wide range of $\text{Pb}(\text{Zr}_{(1-x)}\text{Ti}_x)\text{O}_3$ interfacial layer compositions ($x = 0.2 - 0.8$). PMN-PT/PZT bilayer stacks are prepared on SrRuO_3 electroded and TiO_2 (B-site) terminated SrTiO_3 substrates. The effect of PZT interfacial layer composition on structural, ferroelectric and piezoelectric properties of PMN-PT films was investigated in detail. The deposited films are highly crystalline, as is indicated by rocking curve measurements performed on these samples. Devices fabricated using these heterostructures show a giant self-bias field whose magnitude depends upon the PZT interfacial layer composition. The dielectric and piezoelectric properties of these devices also influenced by PZT interfacial layer composition.

Part of this chapter is published as

- M. Boota, E. P. Houwman, M. Dekkers, M. Nguyen and G. Rijnders, Appl. Phys. Lett., 104 (2014) 182909.
- Dielectric and piezoelectric properties of epitaxial PMN-PT films controlled by PZT interfacial layer composition (To be submitted)

4.1 Introduction

In the previous chapter, the growth of perovskite phase and (001) orientation pure epitaxial PMN-PT (67/33) films is demonstrated on SrTiO_3 substrates using SrRuO_3 symmetric electrodes. However, the crystalline quality of the PMN-PT films reported to date, including the PMN-PT films reported in chapter 3 is inferior compared to the bulk PMN-PT single crystals [1-5]. Maria and co-workers studied the growth of epitaxial PMN-PT (70/30) films and observed the broadening of the processing window with superior lattice mismatch. Superior lattice matching was also found to be helpful to stabilize the pure perovskite phase [3]. It is well-known that the crystallinity of a film can be improved by reducing the lattice mismatch between the film and substrate. Zhu et al. reported the growth of polycrystalline PMN-PT films using a PZT interfacial layer on a silicon substrate. The use of PZT interfacial layer was found to be helpful to stabilize the perovskite phase [1].

The bulk lattice parameters of the PMN-PT, PZT, SrRuO_3 and SrTiO_3 are summarized in table 4.1. From this table, it can be noted that the crystal lattice mismatch between PMN-PT and SrRuO_3 bottom electrode can be reduced using a PZT layer between the two.

Epitaxial PMN-PT film can be deposited on a range of $\text{Pb}(\text{Zr}_{(1-x)}\text{Ti}_x)\text{O}_3$ interfacial layer compositions ($x = 0.2 - 0.8$) and the effect of superior lattice matching together with crystal lattice strain (strain imposed by the difference of lattice parameters) on the structure, ferroelectric and piezoelectric properties of epitaxial PMN-PT thin films can be investigated. It is essential to mention here that PZT films deposited on SrRuO_3 electroded SrTiO_3 substrates are under compressive strain. Compressive strain reduces in-plane lattice parameters of PZT interfacial layer compared to the bulk values. From the table 4.1, we anticipate that PMN-PT films are close in-plane lattice matching with PZT (50/50) interfacial layer composition.

Table 4.1: Bulk lattice parameters of PMN-PT, PZT, SrRuO₃ and SrTiO₃. The “pc” and “ICDD” refer to pseudocubic and international centre for diffraction data (ICDD) respectively.

Material	a (Å)	c (Å)	Reference
PMN-PT (67/33)	(4.022) _{pc}	(4.022) _{pc}	[5]
PZT (20/80)	3.948	4.151	[6]
PZT (30/70)	3.975	4.154	[6]
PZT (40/60)	4.001	4.157	[6]
PZT (50/50)	4.028	4.16	[6]
PZT (60/40)	4.087	×	[6]
PZT (80/20)	4.129	×	[6]
SrRuO ₃	3.954	3.954	01-087-1243 (ICDD)
SrTiO ₃	3.905	3.905	00-005-0634 (ICDD)

In this chapter, we present experimental study of high crystalline quality epitaxial PMN-PT (67/33) thin films deposited using PZT interfacial layers of varying composition. Tetragonal compositions introduces a large build-in self-bias field, that is remarkably stable on prolonged cycling. The self-bias field can be tuned by the PZT composition. Such a tunable self-bias may be of great importance for devices like energy harvesters, which are operated at zero bias. By tuning the self-bias one can optimize operation point and potentially the device performance.

4.2 Experimental Procedure

4.2.1 Samples fabrication

Capacitor stacks of a 100nm SrRuO₃ (SRO) base electrode, 25nm thick PbZr_{1-x}Ti_xO₃ (PZTx), buffer layer, 200nm PMN-PT, and a 100nm thick SRO top electrode were grown on TiO₂ terminated low miscut (001) oriented STO substrates, using the substrate treatment described by Koster and co-workers [7]. The deposited layers stacks are SRO/PMN-PT/SRO denoted as S0, SRO/PZT(20/80)/PMN-

PT/SRO-S1, SRO/PZT(30/70)/PMN-PT/SRO-S2, SRO/PZT(40/60)/PMN-PT/SRO-S3, SRO/PZT(50/50)/PMN-PT/SRO-S4, SRO/PZT(58/42)/PMN-PT/SRO-S5 and SRO/PZT(80:20)/PMN-PT/SRO-S6 respectively. All layers are subsequently deposited by Pulsed Laser Deposition (PLD) using a KrF Excimer laser (248nm) without breaking the vacuum. The PMN-PT films were deposited at a substrate temperature of 600°C, at an pure oxygen pressure of 0.28 mbar, a target-substrate distance of 6 cm and at a laser fluence of 2.25 J/cm² at 4 Hz repetition rate. The deposition conditions of the PZT buffer layers are similar except for the oxygen pressure (0.10 mbar). The deposition conditions of the SRO electrodes are reported in chapter 2. The layer stack is cooled down from deposition temperature to room temperature in a 1 bar pure oxygen atmosphere using cooling rate of 10°C/minute.

4.2.2 Samples Characterization

Structural properties and epitaxial relationships were investigated by High Resolution-X-Ray Diffraction (Bruker D8 Discover). The lattice parameters were obtained from reciprocal space maps. Ferroelectric capacitor structures (200×200µm²) are defined by photolithography, Ar ion beam etching and wet etching. Polarisation-electric field (*P-E*) hysteresis loops were measured using a modified Sawyer Tower circuit (AixACCT TF Analyser 2000) at a scan frequency of 1kHz using a bipolar triangular pulse with an amplitude of 10V. Fatigue measurements were performed using a rectangular pulse train at a frequency of 10 kHz and an amplitude of 10V. The longitudinal piezoelectric coefficients (d_{33}) were obtained from d_{33} loops recorded with the Polytec MSA-400 Micro Scanning Laser Doppler Vibrometer. Capacitance versus electric field vs. capacitance (*C-E*) loops were measured with a Suss MicroTech PM300 probe station equipped with a Keithley 4200 at 10kHz frequency.

4.3 Results and discussions

4.3.1 Structural properties

The θ - 2θ spectra of the PMN-PT film stacks with PZT (50/50) interfacial layer and without PZT interfacial layer are shown in figure 4.1(a). Rocking curve measurements were also performed on both samples and are shown in the inset of the figure 4.1(a). The rocking curves corresponding to PMN-PT films deposited using PZT(50/50) interfacial layer exhibit full width at half maximum (FWHM) 0.05° and without interfacial layer 0.52° . This analysis distinguishly demonstrates significant improvement in the crystalline quality of the PMN-PT films deposited using PZT interfacial layer. The narrowness of the rocking curves of PMN-PT films distinguishably demonstrates the high degree of oriented growth and excellent crystallinity. The improvement in crystallinity is due to superior in-plane lattice matching of PMN-PT film with PZT layer underneath compared to SrRuO_3 bottom electrode. The azimuthal ϕ -scan (figure 4.1b) of the PMN-PT (101) reflection shows in-plane epitaxy with a cube-on-cube epitaxial relation with the SrTiO_3 substrate.

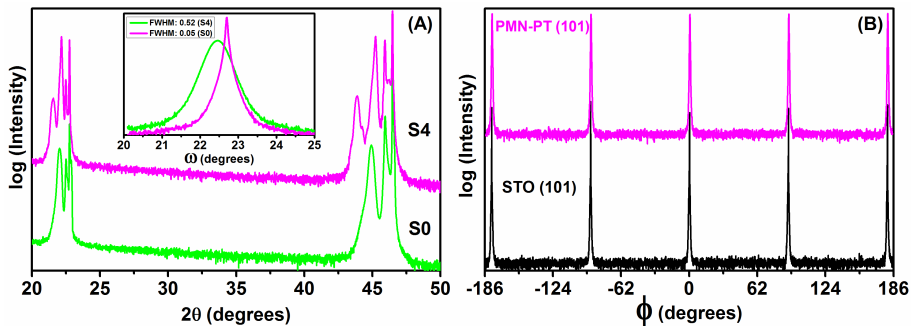


Figure 4.1: Diffraction pattern of epitaxial PMN-PT films deposited with and without PZT interfacial layer with inset showing rocking curves for both samples (a) ϕ scans of the PMN-PT (101) reflection and the STO substrate of sample S4 showing the cube-on-cube epitaxial relation with the substrate (b).

The θ -2 θ spectra of the PMN-PT films deposited on wide range of PZT interfacial layer compositions and without PZT interfacial layer are shown in figure 4.2. The reflections from the substrate, electrodes, PZT interfacial layer and PMN-PT peaks are indicated.

The PMN-PT reflections can all be attributed to (001) growth orientation only, for all samples. In the full range spectrum no extra peaks representing secondary phases (pyrochlore phase) or orientations are detected. Azimuthal ϕ -scans of these PMN-PT films show in-plane epitaxy with a cube on cube relation with the substrate. Rocking scans of the PMN-PT reflections have a full width at half maximum of 0.05-0.21° for the films with PZT buffer layer and 0.52° for the PMN-PT film deposited directly on the SRO bottom electrode. The narrowness of these peaks demonstrates the high degree of oriented growth and good crystallinity of these films. In conclusion the XRD investigations show that the deposited films are perovskite phase and orientation pure as well as epitaxial within the detection limit of the instrument.

From figure 4.2 it is seen that the PMN-PT reflection in most cases are slightly shifted from the angle expected for rhombohedral, unstrained PMN-PT. The broad shoulder at lower angles causing the asymmetric PMN-PT reflection for samples with PZT($x \geq 0.6$) and for sample S0, without PZT, indicates compressive strain relaxation from the in-plane lattice constant of the underlying layer to that of the bulk value of PMN-PT. This is also reflected in the reduced height of the PMN-PT peak relative to the substrate peak for these samples, indicating that part of the signal is shifted to lower reflection angles. For buffer layers PZT($x < 0.6$) there is a small in-plane tensile strain in the PMN-PT layer and thus a marginally decreased out-of-plane lattice parameter. From the RSMs we have determined the in-plane and out-of plane lattice parameters and find marginal tetragonal distortion of the bulk of the layer in the out-of-plane direction, depending on the PZT layer underneath.

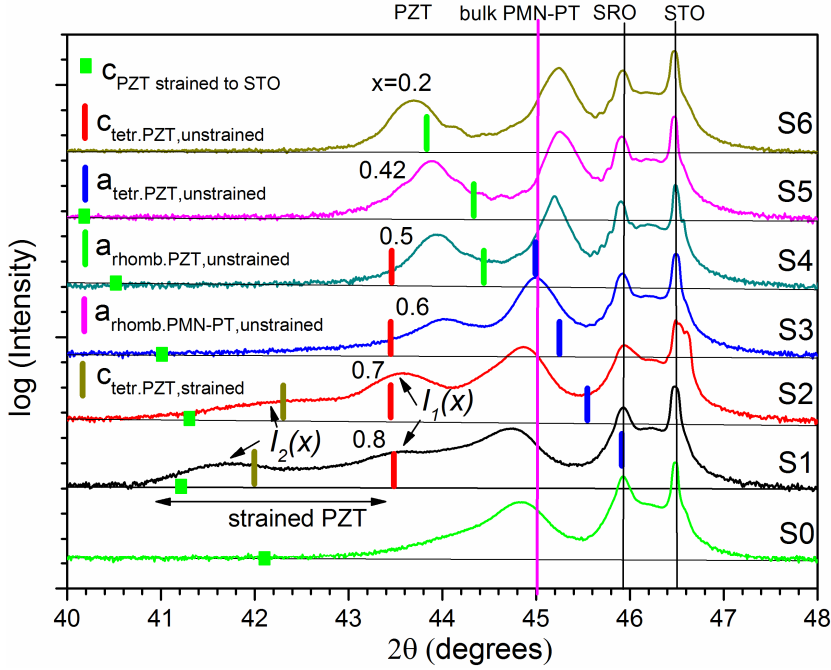


Figure 4.2: X-ray diffraction spectra of 200nm PMN-PT ferroelectric capacitors on STO substrates with 100nm SRO electrodes without (sample S0) and with (S1-S6) 25nm PZT buffer layers with varying compositions. The bars indicate the positions of reflection peaks of unstrained PZT and PMN-PT films. The square denotes the position of PZT and PMN-PT strained fully to the substrate [Figure attained from ref. 8].

The 2θ angles of the bulk, unstrained lattice parameters are denoted in the spectra of figure 4.2. For PZT($x < 0.5$) a single PZT reflection (intensity $I_1(x)$) is observed, whereas for the tetragonal compositions a second, weaker peak ($I_2(x)$) appears with a larger out-of-plane lattice constant. For the tetragonal compositions there is no signature of domains with the long axis in plane (a domains), which would show up near the angles indicated by $a_{\text{tetr.PZT, unstrained}}$. The main out-of-plane reflections for $x=0.7$ and 0.8 correspond well with an unstrained long-axis value of the unit cell ($c_{\text{tetr.PZT, unstrained}}$). The second lower intensity peak corresponds to strong in-plane compression with an in-plane lattice parameter of about 3.95 \AA , approaching that of the

STO substrate (3.905 Å). (If the PZT were fully strained to the substrate, the out-of-plane reflection would appear at the positions denoted by $c_{PZT \text{ strained to STO.}}$) The broad plateau in between the peaks ($x=0.7$ and 0.8) and the wide shoulder (for $x=0.6$) at the low angle side of the main PZT reflection of the tetragonal composition films is attributed to a gradual strain relaxation from the highly strained layer to the bulk of the film. From the measured (integrated) intensities, knowing the total thickness of the PZT layer (25nm), the thickness of the highly strained layers are estimated as 5 nm and 10 nm for $x=0.8$ and 0.7 respectively.

For $x=0.6$ and 0.5 the out-of-plane lattice parameters are clearly reduced from the expected value, indicating tensile strain. For the rhombohedral PZT compositions the unit cell is slightly compressively strained. The c/a ratio obtained from the XRD data as function of the PZT-composition is depicted in figure 4.3 (a), together with the values for bulk PZT as obtained from the description of the PZT-series by Rosetti *et al.* [6]. In figure 4.3(b) the unit cell volumes (V_{uc}) are given, showing constant V_{uc} for all buffer layers. The data points corresponding to the reflections I_2 on the other hand correspond to an extremely large compressive strain (large (c/a) and slightly enhanced V_{uc} .

For $x=0.6$ and 0.5 the out-of-plane lattice parameters are clearly reduced from the expected value, indicating tensile strain. For the rhombohedral PZT compositions the unit cell is slightly compressively strained. The c/a ratio obtained from the XRD data as function of the PZT-composition is depicted in figure 4.3(a), together with the values for bulk PZT as obtained from the description of the PZT-series by Rosetti *et al.* [6]. In figure 4.3(b) the unit cell volumes (V_{uc}) are given, showing constant V_{uc} for all buffer layers. The data points corresponding to the reflections I_2 on the other hand correspond to an extremely large compressive strain (large (c/a) and slightly enhanced V_{uc} .

The XRD analysis indicates that the PZT layers with rhombohedral compositions and the main part of the tetragonal PZT

films are slightly strained. The tetragonal films with large bulk c/a ratio show a relaxing strain gradient with maximum strain at the base electrode/PZT interface, relaxing into the film. Strain relaxation occurs by the incorporation of lattice defect, which is generally accompanied by defect charges. Further, the high strain and an increased defect density increases the PZT unit cell volume.

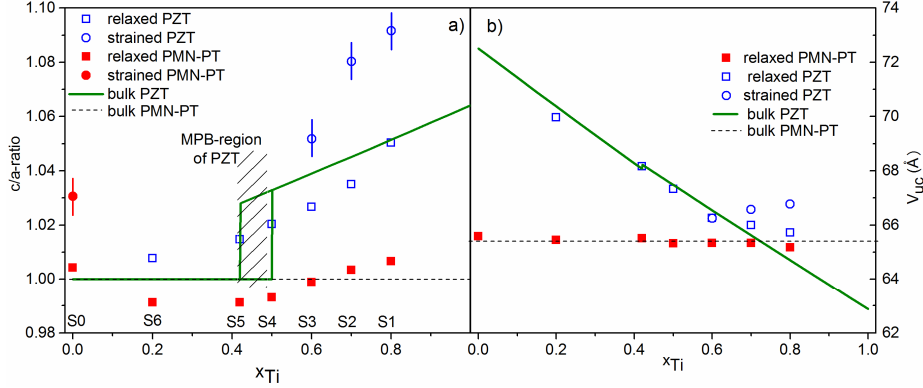


Figure 4.3: Measured ratio of the out-of-plane and in-plane lattice parameters (c/a ratio) of the largely relaxed bulk, respectively, strained fractions of the PZT and PMN films in the PZT/PMN-PT ferroelectric capacitors. The curve is according to the model of ref. [6]. The hatched region denotes the region around the Morphotropin Phase Boundary (a) Measured unit cell volume of the largely relaxed bulk, respectively strained fractions of the PZT and PMN-PT films (b) [Figure attained from ref. 8].

4.3.2 Ferroelectric properties and aging behaviour

The polarization hysteresis loops were measured and for the analysis below the self-bias field $E_{sb} = (E_c^+ + E_c^-)/2$, the coercive field $E_{c,av} = (E_c^+ - E_c^-)/2$ and the saturation polarization field were determined. The latter is defined here as the cut-off of the high-field tangent with the $E = E_{sb}$ axis. In figure 4.4 (b) the self-bias field and the coercive field are shown as function of the PZT-composition of the buffer layer. The devices with large E_c correspond to those with a large strain relaxation layer at the base-electrode/ferroelectric

interface, both in the devices with (S1 and S2) and without PZT-buffer layer (S0). The devices with predominantly constant (small) strain in the PZT and PMN-PT layers (S3 to S6) have negligible self-bias. The coercive field shows a similar trend.

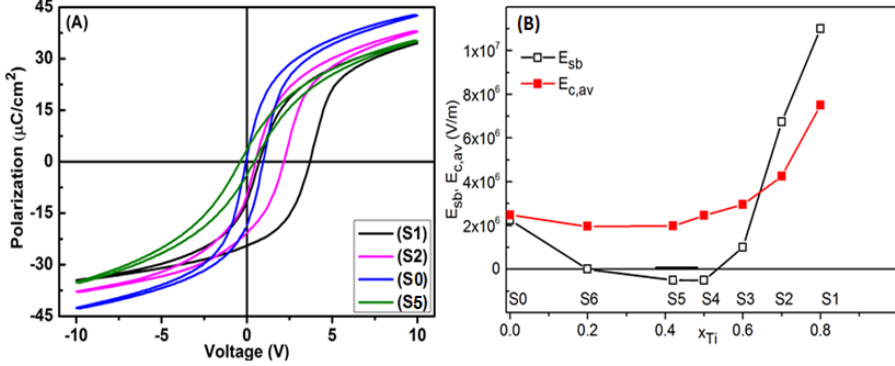


Figure 4.4: Polarization hysteresis loops before cycling indicating PZT interfacial layer composition dependent self-bias (a) Measured self-bias field E_{sb} and coercive field E_c (before aging) of PZT/PMN-PT ferro-electric capacitors. The data point at $x_{Ti}=0$ corresponds to the device without PZT bufferlayer. The lines are guides to the eye (b). [Figure adopted from ref. 8]

In figure 4.5(a) E_{sb} is shown as function of the number of aging cycles (cycling through the complete PE-loop up to ± 500 kV/cm) for the devices S0, S1, S2 and S5. The devices S0 and S3-6, are very stable up to the maximum number of cycles, 10^8 implying that the charge density profile in the device is very stable upon cycling. For S1 as well as S2 the self-bias and coercive field both decrease monotonically upon cycling and stabilize after about 10^7 - 10^8 cycles, which indicates a new, stable charge configuration has been established. We expect that the main reason is that compensating charges enter the film and reduce the charge density. We think that the coercive field values of the devices S1 and S2 are strongly linked to the (charged) defect density through domain wall pinning and that therefore E_c of these devices also decreases with decreasing charge

density. For $E_c < 2.5$ MV/m another pinning mechanism is dominant, that is apparently not linked to the charge density.

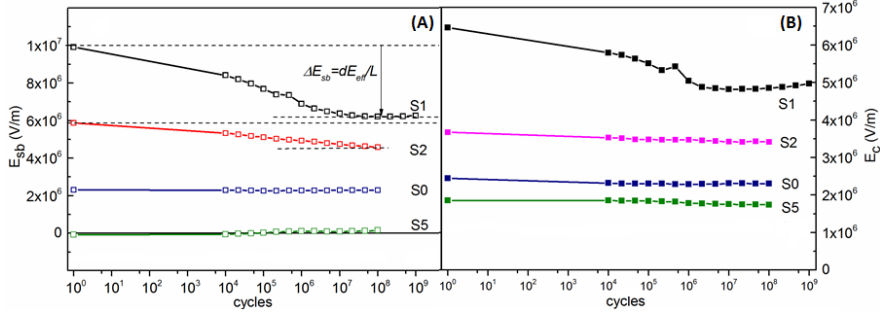


Figure 4.5: Self-bias field E_{sb} as function of number of cycling (up to $\pm 5 \times 10^7$ V/m) (a) and coercive field E_c as function of number of cycling through the hysteresis loop (up to $\pm 5 \times 10^7$ V/m) (b) [Figure adopted from ref. 8].

In spite of many theoretical and experimental work on possible causes of field bias in ferroelectric capacitors the physical mechanism behind the built-in fields are often hard to identify, since many extrinsic (such as asymmetric electrodes; inhomogeneous oxygen distribution; charged defect layers; ‘dead’ dielectric layers near the electrodes) and intrinsic factors (bi- or multilayer structures or compositionally graded structures causing inhomogeneous strain and polarization gradients) may play a role. In the devices S0, S1 and S2 we identified compressively strained layers next to the base electrode, of which the thicknesses were estimated. In such a layer the strain is relaxed by dislocations, which can be accompanied by charged defects. This charged layer may be the (extrinsic) mechanism behind the field bias. On the other hand the strain gradient can also give rise to an internal field. This is then considered an internal cause. Assuming that the self-bias is due to a homogeneous charge distribution $\rho(x)$ due to dislocations in the strain relaxation layer with thickness a_ρ we calculate the field in the dielectric by applying Gauss law to a Gaussian pillbox around the charged layer in the capacitor with grounded electrodes as

$$\vec{E}_p = \begin{cases} \frac{\rho a_p}{\varepsilon_0 \varepsilon_b} \frac{a_p}{2L} \vec{e}_x & x > a_p \\ \frac{\rho a_p}{\varepsilon_0 \varepsilon_b} \left(\frac{a_p}{2L} - 1 + \frac{x}{a_p} \right) \vec{e}_x & 0 < x < a_p \end{cases} \quad (1)$$

Here, ε_b is the dielectric constant of the background dielectric, which is assumed to be constant over the total stack thickness L and is of the order of 10 [9]. The space charge layer thickness a_p is a fraction of the PZT layer and is estimated from the integrated XRD intensity ratio to be 5 and 10nm respectively for S1 and S2 and 16 nm for S0. Since a_p is small compared to the total thickness of the stack the observed self-bias field is largely due to the constant field for $x > a_p$. The space charge density is estimated from the measured self-bias field of the order of $\rho = 1.6 \times 10^7 \text{ C/m}^3$ or $6.4 \times 10^{-3} |e|/\text{unit cell}$ for the sample S1 with the largest bias field, $E_{sb} = 101 \text{ kV/cm}$, is found. This corresponds to a positive charge of one $|e|$ in each cube of $5.4 \times 5.4 \times 5.4$ unit cells, thus a fairly low defect density, consistent with defects concentrated at grain boundaries and defect planes, that create the necessary stress relaxation.

In this picture the very small self-bias fields for S3-6 ($|E_{sb}| < 10^6 \text{ V/m}$) are ascribed to a very thin, lightly charged layer, or ‘dead’ (passive) dielectric layer adjacent to the electrodes and/or dielectric grain boundaries [9].

Upon continuous cycling the self-bias and the coercive field decreases. This can be interpreted as being due to compensation of the positive charges in the strained layer by electrons injected from the electrode in an irreversible process.

The observed strain gradient in the devices with large self-bias suggests a second possible cause, the flexoelectric effect. This mechanism was introduced by Abe et al. [10] and later well explained by Tagantsev and Gerra [9]. Due to the strain gradient in the stress relaxation layer at the bottom electrode a large effective electrical field E_{eff} can be created in this layer (with thickness d) through the flexoelectric effect

$$E_{\text{eff}} = E_3 = \phi_{11} \frac{\partial S_3}{\partial x_3} + 2\phi_{12} \frac{\partial S_1}{\partial x_3} \quad (2)$$

Here ϕ_{ij} are the strain gradient – electric field coupling coefficients. In our case we also have taken into account the gradient in the out-of-plane lattice parameter, which effect is not considered in literature. For the tetragonal films considered here the out-of-plane gradient term can be estimated as $\partial S_3 / \partial x_3 \approx \Delta S_3 / d = (c(d) - c(0)) / a_c d$, where $c(0)$ is the (measured) c –axis length of the strained layer and $c(d)$ of the unstrained PZT. The upper limit of the in-plane gradient term is $\partial S_1 / \partial x_3 = \Delta S_1 / d = (a(d) - a(0)) / a_c d$, where a is the measured in-plane lattice parameter. The values of the flexoelectric tensor components have been estimated as $|\phi_{ij}| = e / 4\pi\epsilon_0 a_l$, with e the electron charge and a_l a typical lattice parameter of the order of a_c . $|\phi_{ij}| / a_l = E_{\text{at}}$ is the so called typical atomic electric field, equal to about 100MV/cm for perovskites. Further it seems reasonable to assume that ϕ_{12} has a sign opposite to that of ϕ_{11} . The resulting estimate of the absolute value of the effective field in the strained layer is $|E_{\text{eff}}| = |E_{\text{at}}(\Delta S_3 - 2\Delta S_1)(a_c/d)|$.

The effective field can be so large that the thin layer can become non-switchable for all applied external field values, so that a fixed polarization P_M is present in the non-switchable layer, that corresponds to the value of the effective field. This polarization is directed away from the bottom electrode. Further, at the interface of the non-switchable layer and the switchable layer a free charge layer with charge density σ may be present. The self-bias voltage V_{sb} (or (apparent) self-bias field $E_{sb} = V_{sb}/h$, where h is the total ferroelectric stack thickness which is contrast with ref. 9. In our configuration the bottom electrode is grounded, therefore the signs of all voltages are inverted)

$$V_{sb} = \frac{d}{\epsilon_0 \epsilon_{f,\text{str}}} (P_M + \sigma) + dE_{\text{eff}} \quad (3)$$

$\epsilon_{f, \text{str}}$ and d are the relative dielectric constant and thickness of the strained layer. We have observed that over time V_{sb} changes with cycling and reaches a new stable value. Assuming that in the initial state the free interface charge density is (negligible) small, one has initially a large self-bias voltage, $V_{sb}^{ini} = dP_M/\epsilon_0\epsilon_{f, \text{str}} + dE_{\text{eff}}$. After long cycling free charge builds up at the interface and compensates the field in the strained layer, reaching a value $\sigma = -\epsilon_0\epsilon_{f, \text{str}}E_{\text{eff}}$, so that the final self-bias voltage is $V_{sb}^{fin} = dP_M/\epsilon_0\epsilon_{f, \text{str}}$.

From the measured self-bias voltages and strained layer thickness, we estimate $E_{\text{eff}} = 1.7 \times 10^8$ V/m for S1. This is only a factor 3 larger than the value estimated above from the flexoelectric effect. Assuming the value of P_M to be equal to the spontaneous polarization $P_s = 0.70$ C/m² of bulk material, one obtains $\epsilon_{f, \text{str}} = 274$ and the free interface charge density is then -0.40 C/m². This suggests that the permittivity of the strain-gradient layer is significantly enhanced over that of the bulk value ($\epsilon_{f, \text{bulk}} = 86$ for $x = 0.8$). This may be ascribed to the fact that the layer is not only subjected to a strain gradient but also to a very large strain, considering that the c/a ratio reaches a value of approximately 1.09 in this layer. In fact this will also cause an increase of P_M .

The large self-bias voltage of S2 and its cycling dependence can be explained in the same way. S0 does not show any cycling dependence of E_{sb} , suggesting that the displacement of free charges does not take place. The self-bias voltage is low compared to the initial V_{sb} values in S1 and S2. The lowest value that can be obtained is when the effective field is fully compensated by trapped free charge from the very first fatigue cycle onwards, thus $V_{sb} = dP_M/\epsilon_0\epsilon_{f, \text{str}}$. In this case the polarization is directed approximately in the body diagonal of the rhombohedrally distorted pseudocubic lattice of PMN-PT, hence $P_M \approx P_s/\sqrt{3} = 0.32$ C/m². With this value one obtains $\epsilon_{f, \text{str}} = 1240$, which is enhanced by a factor 2 with respect to the

literature value 680 for poled PMN-PT [12]. From this argument one has to conclude that already during cool down after fabrication of the S0 device free charge is trapped in the PMN-PT that compensates the effective field.

The samples S3-6 do not show any significant self-bias nor any significant strain gradient in the PZT and the PMN-PT layer. This is taken as a strong indication that the strain gradient is the dominating mechanism behind the large self-biases in the devices S0-2.

The observation that the very thin tetragonal PZT layers (S1-2) grow in a single c -domain phase with the long axis out-of-plane is in accordance with the model of Pertsev *et al.* [13] for strained, single domain PZT thin films. In this model there is a transition to the (rhombohedral) r -phase for $\varepsilon_{f, \text{str}}$ and d are the relative dielectric constant and thickness of the strained layer. We have observed that over time V_{sb} changes with cycling and reaches a new stable value. Assuming that in the initial state the free interface charge density is (negligible) small, one has initially a large self-bias voltage, $V_{sb}^{ini} = dP_M / \varepsilon_0 \varepsilon_{f, \text{str}} + dE_{\text{eff}}$. After long cycling free charge builds up at the interface and compensates the field in the strained layer, reaching a value $\sigma = -\varepsilon_0 \varepsilon_{f, \text{str}} E_{\text{eff}}$, so that the final self-bias voltage is $V_{sb}^{fin} = dP_M / \varepsilon_0 \varepsilon_{f, \text{str}}$.

From the measured self-bias voltages and strained layer thickness, we estimate $E_{\text{eff}} = 1.7 \times 10^8$ V/m for S1. This is only a factor 3 larger than the value estimated above from the flexoelectric effect. Assuming the value of P_M to be equal to the spontaneous polarization $P_s = 0.70$ C/m² of bulk material, one obtains $\varepsilon_{f, \text{str}} = 274$ and the free interface charge density is then -0.40 C/m². This suggests that the permittivity of the strain-gradient layer is significantly enhanced over that of the bulk value ($\varepsilon_{f, \text{bulk}} = 86$ for $x=0.8$). This may be ascribed to the fact that the layer is not only subjected to a strain-gradient but also to a very large strain, considering that the c/a ratio reaches a value of approximately 1.09 in this layer. In fact this will also cause an increase of P_M .

The large self-bias voltage of S2 and its cycling dependence can be explained in the same way. S0 does not show any cycling dependence of E_{sb} , suggesting that the displacement of free charges does not take place. The self-bias voltage is low compared to the initial V_{sb} values in S1 and S2. The lowest value that can be obtained is when the effective field is fully compensated by trapped free charge from the very first fatigue cycle onwards, thus $V_{sb} = dP_M/\epsilon_0\epsilon_{f,str}$. In this case the polarization is directed approximately in the body diagonal of the rhombohedrally distorted pseudocubic lattice of PMN-PT, hence $P_M \approx P_s/\sqrt{3} = 0.32 \text{ C/m}^2$. With this value one obtains $\epsilon_{f,str} = 1240$, which enhanced by a factor 2 with respect to the literature value 680 for poled PMN-PT [12]. From this argument one has to conclude that already during cool down after fabrication of the S0 device free charge is trapped in the PMN-PT that compensates the effective field.

The samples S3-6 do not show any significant self-bias nor any significant strain gradient in the PZT and the PMN-PT layer. This is taken as a strong indication that the strain gradient is the dominating mechanism behind the large self-biases in the devices S0-2.

The observation that the very thin tetragonal PZT layers (S1-2) grow in a single c -domain phase with the long axis out-of-plane is in accordance with the model of Pertsev *et al.* [13] for strained, single domain PZT thin films. In this model there is a transition to the (rhombohedral) r -phase for PZT($x \approx 0.6$) on STO. We observe a transition at approximately this value from the highly strained initial growth layer to what can be interpreted as a slightly tetragonally distorted rhombohedral phase, in accordance with this model. Further it appears that in the samples S1-2 the high initial strain relaxes largely within the first 5-10nm, whereas in S3-6 it is practically immediately relaxed, which is indicative for a high density of misfit dislocations p and therefore short strain relaxation layer thickness.

4.3.3 Dielectric and piezoelectric properties

The voltage verses capacitance (V-C) curves and d_{33} loops are recorded to study the dielectric and piezoelectric properties of the ferroelectric capacitors fabricated from the PMN-PT films grown on wide range of PZT compositions along with without PZT interfacial layer. The relative dielectric constant verses voltage curves derived from capacitance verses voltage curves and d_{33} loops for selected samples are shown in figure 4.6.

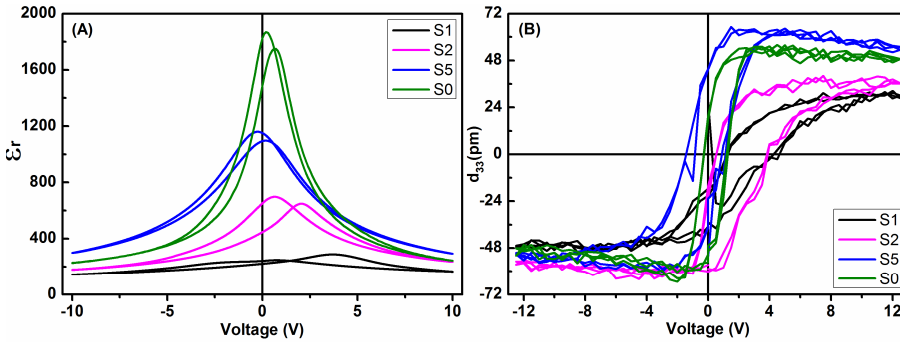


Figure 4.6: Dielectric constant verses voltage curves derived from capacitance verses voltage curves measured at 10kHz of selected samples (a) d_{33} loops of the same samples (b).

The relative permittivity curves shown in figure 4.6 (a) measured for different samples are significantly different. The relative dielectric curves are shifted in positive field direction for the sample S1, S2 and S0 similar to P-E loops shown in figure 4.4(a) while the curve corresponds to S5 is slightly shifted towards negative field direction. The shifting trend of dielectric curves either in positive field direction or negative field direction is found similar to the trend observed for P-E loops recorded for these devices. The shifting trend for relative permittivity curve similar to ferroelectric loop was also observed for epitaxial PMN-PT films deposited on silicon substrate [4] Nagarajan and co-workers studied the effect of strain on dielectric

and piezoelectric properties of epitaxial PMN-PT (91/10) films and observed the enhancement of dielectric constant with strain relaxation [15]. The similar trend was observed in our case. The strain in the film not only results self-bias in the films which reduces relative dielectric constant at zero volts by shifting the relative permittivity curves but also the magnitude of relative dielectric constant. The low dielectric is beneficial because it increases the figure of merit ($\text{FOM} = \frac{e_{31}^2}{\epsilon_0 \epsilon_r}$) for sensors operating in voltage sensing mode, as well as for piezoelectric energy harvesting systems. The dielectric and piezoelectric properties are summarized in table 4.2.

Table 4.2: Summary of dielectric and piezoelectric properties of PMN-PT films deposited on a range of PZT interfacial compositions and without PZT interfacial layer.

Sample	PZT buffer	ϵ_r , (max)	ϵ_r @ 0V	$d_{33 \text{ eff}}$, (max)	$d_{33 \text{ eff}}$, (av.)
	Zr/Ti				
S1	20/80	267	231	49	41
S2	30/70	674	549	62	51
S3	40/60	1312	1248	62	60
S4	50/50	1495	1461	71	67
S5	58/42	1129	1122	63	61
S6	80/20	1309	1300	56	54
S0	No PZT	1810	1654	59	57

The d_{33} loops recorded for the selected samples are shown in figure 4.6(b). The shift of these loops is also similar to P-E loops and relative dielectric curves. The effective longitudinal piezoelectric coefficient (d_{33}) is lower compared for those samples which show higher self-bias and vice versa. However, higher transverse piezoelectric coefficient (e_{31}) is expected for those film which have higher self-bias. Furthermore, it is also evident from these loops that self-bias enhances the longitudinal piezoelectric coefficient (d_{33}) in certain preferential direction. For instance, the S0 show positive

imprint and higher d_{33} in negative field direction compared to positive field direction. Similarly the S5 shows negative imprint and show higher d_{33} in positive field direction. The enhancement of d_{33} in preferential direction might be interesting for some devices which needs higher d_{33} in certain preferential direction.

4.4 Conclusions

In conclusion, we have grown ferroelectric capacitors consisting of a 25nm PZT buffer layer of varying composition and a 200nm PMN-PT(67/33) layer on STO substrates with SRO electrodes, as well as a device without PZT buffer layer. XRD analysis shows that all layers are grown with (001) orientation. The PMN-PT layers are perovskite phase pure and do not show any signatures of the pyrochlore phase. The PZT buffer layers with tetragonal composition ($x_{Ti} > 0.6$) are initially compressively strained to the substrate and relax fully over the layer thickness. The PZT compositions which have nearly cubic bulk lattice structure ($x \leq 0.6$) are only slightly and homogeneously strained. The PMN-PT layers on PZT($x \leq 0.6$) buffers show a small homogenous strain, whereas those on the highly tetragonal compositions and grown directly on the base electrode show a strain gradient.

The samples with strain gradients near the bottom electrode show large and fairly stable self-bias voltages. The large self-bias samples also show strongly increased coercive fields. The large self-bias was discussed in two ways. Firstly in the strain gradient regions the enhanced defect density can be associated with trapped charges. However, in this model the charge density and its sign are free parameters. Secondly, the strain gradient layers can create a self-bias field through the flexoelectric effect. The observed self-bias voltages are consistent with the measured strain gradients and layer thicknesses.

The self-bias voltage can be tuned in a fairly wide range by the composition of the buffer layer. This is of significance for devices like

energy scavengers and low energy consumption sensors that preferably operate at zero bias voltage.

The higher longitudinal piezoelectric coefficient (d_{33}) was observed for the PMN-PT films deposited on PZT (50/50) interfacial layer with very small self-bias. It is known that doped PZTs can show self-bias due to extra defected dipoles resulted from doping. So it is interesting to study growth of epitaxial PMN-PT film on doped PZT (52/48) interfacial layer to achieve higher d_{33} as well as self-bias.

4.5 References

- [1] J. Zhu, X. Zhu, M. Jiang, X. Li, J. Zhu and D. Xiao, *J. Appl. Phys.* 104 (2008) 086104.
- [2] D. Lavric, R. A. Rao, Q. Gan, J. J. Krajewski and C. B. Eom, *Integrated Ferroelectrics*, 21 (1998) 499.
- [3] J. P. Maria, W. Hackenberger and S. Trolier-McKinstry, *J. Appl. Phys.*, 84 (1998) 5147.
- [4] S. D. Bu, M. K. Lee and C. B. Eom, *Appl. Phys. Lett.*, 79 (2001) 3482.
- [5] S. H. Baek, D. M. Kim, V. A. Aksyuk, R. R. Das, S. D. Bu, ... and C. B. Eom, *Science*, 334 (2011) 958.
- [6] G. A. Rossetti, A. G. Khachaturyan, G. Akcay and Y. Ni, *J. Appl. Phys.*, 103 (2008) 114113.
- [7] G. Koster, B. L. Kropman, G. J. H. M. Rijnders, D. H. A. Blank, and H. Rogalla, *Appl. Phys. Lett.*, 73, (1998) 2920.
- [8] M. Boota, E. P. Houwman, M. Dekkers, M. Nguyen and G. Rijnders, *Appl. Phys. Lett.* 104 (2014) 182909.
- [9] A. K. Tagantsev and G. Gerra, *J. Appl. Phys.*, 100 (2006) 051607.
- [10] K. Abe, N. Yanase, T. Yasumoto, and T. Kawakubo, *J. Appl. Phys.*, 91 (2002) 323.
- [11] In contrast with ref. 9 in our configuration, the bottom electrode is grounded; therefore, the sign of all voltages are inverted. In ref. 10 an interface charge is assumed to be present. Here, it is

more likely that the charge is distributed over the strained layer, which is expected to have a similar effect on the self-bias.

- [12] H. Cao, V. H. Schmidt, R. Zhang, W. Cao and H. Luo, J. Appl. Phys., 96 (2004) 549.
- [13] N. A. Perstev, V. G. Kukhar, H. Kohlstedt and R. Waser, Phys. Rev. B 67 (2003) 054107.
- [14] V. Nagarajan, C. S. Ganpule, B. Nagaraj, S. Aggarwal, S. P. Alpay, and A. L. Roytburd, Appl. Phys. Lett. 75 (1999) 4183.

5.

PMN-PT films on doped PZT interfacial layer

Chapter Overview:

Perovskite phase and (001) orientation pure epitaxial PMN-PT (67/33) thin films were fabricated using a hard (Fe-doped) and soft doped (Nb-doped) PZT(52/48) interfacial layer. Heterostructures were prepared on SrRuO_3 electroded and TiO_2 B-site terminated SrTiO_3 substrates. The effect of doping types on the structural, ferroelectric and piezoelectric properties of PMN-PT films was investigated in detail. It was found that a self-bias voltage in the PMN-PT films can be introduced by using an appropriate interfacial layer. The deposited films are highly crystalline, as was indicated by rocking curve measurements performed on these samples. Furthermore, the effect of the thickness of the Nb-PZT interfacial layer on properties of PMN-PT films was analyzed in detail.

This chapter to be submitted as:

- The effect of hard and soft PZT interfacial layer on structural, ferroelectric and piezoelectric properties of epitaxial PMN-PT films

5.1 Introduction

In the previous chapter, it was demonstrated that epitaxial PMN-PT films deposited on a thin PZT layer (25nm) at the bottom electrode/PMN-PT interface can exhibit a giant self-bias voltage. The magnitude of this built-in bias depends upon the composition of the PZT interfacial layer. The highest longitudinal piezoelectric coefficient ($d_{33\text{eff}}$) was observed for PMN-PT films deposited on a $\text{Pb}(\text{Zr}_{0.50}\text{Ti}_{0.50})\text{O}_3$ interfacial layer with very small (1.7kV/cm) self-bias voltage. For some applications, it may be desirable to have a higher build-in bias as well as longitudinal piezoelectric coefficient ($d_{33\text{eff}}$). It is known that donor (Niobium) and acceptor (Iron) doped PZT thin films show self-bias due to oxygen vacancies and space charges. Dopants introduce extra aligned defect dipoles in PZT films which result into an asymmetric polarization hysteresis loop (imprint) [1]. To study the field shifted influence of a Niobium and Iron doped $\text{Pb}(\text{Zr}_{0.52}\text{Ti}_{0.48})\text{O}_3$ interfacial layer on the ferroelectric and piezoelectric properties of epitaxial PMN-PT films, heterostructures were prepared on TiO_2 plane terminated and SrRuO_3 electroded vicinal SrTiO_3 substrates. For sake of comparison, one sample using a $\text{Pb}(\text{Zr}_{0.52}\text{Ti}_{0.48})\text{O}_3$ interfacial layer without doping was also prepared.

5.1.1 Hard verses Soft doped PZTs

Doping elements used for bulk and thin film PZT ceramics are typically categorised into hard doping and soft doping. Hard doping usually refers to acceptor doping whereas soft doping refers to donor doping [2]. PZT is a perovskite material which crystal structure is typically described with the formula ABO_3 . Further information about the perovskite crystal structure can be found in chapter 1. PZT consists of two positively charged ions i.e. A^{2+} and B^{4+} (cations) and three negatively charged ions i.e. O^{2-} (anion) which are simultaneously bonded with the A and B ions. Hard doping refers to the situation in which one of the A-site atoms (A^{2+}) are replaced by monovalent

dopant elements (X^{1+}) or some B-site atoms (B^{4+}) are replaced with trivalent dopant elements (X^{3+}). This situation is universally known as A-site acceptor doping and B-site acceptor doping respectively. Similarly soft doping refers to the situation in which the A-site atom (A^{2+}) is replaced with a trivalent dopant element (X^{3+}) or the B-site atom (B^{4+}) is replaced with a penta-valent dopant element (X^{5+}). This situation is commonly identified as A-site and B-site donor doping respectively. The induced charge resulting from the deficiency of one electron caused by acceptor doping is neutralised by creation of a double positively charged oxygen vacancy ($V_O^{\bullet\bullet}$), thus Fe doping leads to $Fe^{3+}-V_O^{\bullet\bullet}$ complexes. In the case of donor doping, the extra electrons are compensated by double negatively charged lead vacancies (V_{Pb}''). Thus for Nb-doping $Nb^{5+}-V_{Pb}''$ complexes are formed. In this way dipoles are created in the ferroelectric domains [3]. The selection of the doping element depends upon the specific application. The soft doped PZT ceramics exhibit superior piezoelectric coefficients, low conductivity, low coercive field, high dielectric constant along with high dielectric losses while hard doped PZTs performs in the opposite way [4].

The nomenclature ‘hard’ is used for acceptor doped PZTs owing to the stable domain wall structure, which makes poling and depoling more difficult. The compensating defect [Oxygen vacancies ($V_O^{\bullet\bullet}$)] in this case can move relatively easily within the oxygen octahedral (unit cell) network leading to a relative low stability of the defect dipole direction. These defect dipoles tend to align themselves in the direction of polarization vector within the domain. This alignment results stable domain structure and a relatively high coercive field. The nomenclature ‘soft’ is used for donor doped PZTs owing to ease in domain wall motion which makes poling and depoling process comparatively easy. Easily moving compensating defect [electrons or lead vacancies V_{Pb}''] in this case results softening in donor doped PZTs. In the perovskite ABO_3 crystal structure, cations are separated by entire unit cell (0.4nm) from the neighbouring cations

of same kind due to network of oxygen octahedral surroundings. The separation between the cations and anions (0.28nm) is smaller as compared to above case. This small separation between oxygen sites results easy motion of the domains walls in soft ceramics as compared to hard ceramics [5-7]. However, the mechanism responsible for softening effect in donor doped PZTs is still not completely understood.

5.1.2 Iron and Niobium doped PZTs

$\text{Pb}(\text{Zr}_{0.52}\text{Ti}_{0.48})\text{O}_3$ doped with Iron (Fe^{3+}) and Niobium (Nb^{5+}) at B-site acting as acceptor and donor dopant respectively were selected to use as interfacial layer in this study. The ionic radii of Fe^{3+} , Nb^{5+} , Ti^{4+} and Zr^{4+} are 0.65, 0.64, 0.61 and 0.72 respectively. The ionic radius of the acceptor and donor doping element is close to those of the B-site elements of the PZT material. This illustrates that these elements can be doped easily in the B-site of perovskite oxide crystal structure [8]. Doping concentrations of 1.0 mole % Nb^{5+} as donor and 1.0 mole % Fe^{3+} as acceptor (both at $\text{Zr}^{4+}/\text{Ti}^{4+}$ site) were selected based on reported work [9], where for these concentrations maximum d_{33} values were obtained.

Haccart and co-workers performed a study on the effect of the Nb concentration on the properties of PZT films deposited by sputtering on platinised silicon. They observed a relatively high self-bias for low Nb doping level (2 atomic percent) compared to high doping level (7 atomic percent) related with dipolar defects, composed of $\text{Nb}^{5+}-V''_{\text{Pb}}$ complexes aligned within the bulk of the film [10]. Subsequent work performed by different groups shows the effect of Nb-doping on the electrical properties (self-bias) of textured PZT films. They reported the enhancement of ferroelectric and piezoelectric properties of PZT film doped with niobium [11-12]. The effect of the B-site acceptor dopant (Fe) concentration was studied by Majumder and co-workers, who showed a decrease of the remanent polarization with increasing acceptor dopant concentration [13]. Bai

et.al. studied the effect of the Fe concentration on the properties of PZT thin films deposited by the sol gel method. They observed a Fe-concentration dependent shift of the ferroelectric loop, which was ascribed to oxygen vacancies [14]. In Fe-doped PZT films, the acceptor species introduces changes in the domain contribution by increasing oxygen vacancy density. Dawber and co-workers reported that mobile charged defects such as oxygen vacancies can easily accumulate near the film/electrode interfaces due to the higher mobility of the oxygen vacancies than those of lead. This results in the formation of interfacial layers under an external field. These can result in a shift of the hysteresis loops [1, 15].

It is noticed here that most of the work reported on doped PZT films is about polycrystalline thin films. The physical mechanisms behind the origin of different characteristics in acceptor and donor doped PZT films is not fully understood yet. Furthermore, the ferro and piezoelectric properties of epitaxial thin films and the physical mechanisms behind these may be different from polycrystalline thin films.

To study the effect of doped PZT interfacial layers on ferro and piezoelectric properties of epitaxial PMN-PT films, heterostructures were prepared using a $\text{Pb}(\text{Zr}_{0.52}\text{Ti}_{0.48})\text{O}_3$ target doped with 1 mole % Fe^{3+} or 1 mole % Nb^{5+} . The Nb-doped PZT interfacial layer has thus the composition $\text{Pb}(\text{Zr}_{0.52}\text{Ti}_{0.48})_{0.99}\text{Nb}_{0.01}\text{O}_3$ and the Fe-doped PZT interfacial layer has the composition $\text{Pb}(\text{Zr}_{0.52}\text{Ti}_{0.48})_{0.99}\text{Fe}_{0.01}\text{O}_3$. For comparison, epitaxial PMN-PT(67/33) films were also prepared using a $\text{Pb}(\text{Zr}_{0.52}\text{Ti}_{0.48})\text{O}_3$ interfacial layer without doping. The results of these investigations were discussed with respect to ferro and piezoelectric properties of epitaxial PMN-PT thin films. The deposited heterostructure is schematically shown in figure 5.1.

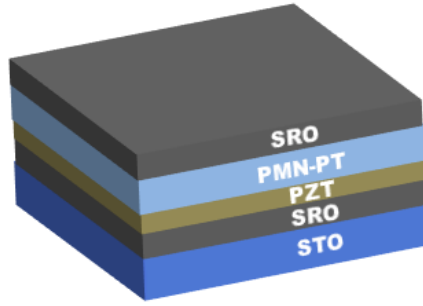


Figure 5.1: Schematic of the layer stack used to study the effect of doped PZT interfacial layer.

5.2 Experimental Procedure

5.2.1 Samples fabrication

The PMN-PT/PZT (200nm/25nm) bilayer stack was sandwiched between 100nm SrRuO₃ electrodes. The complete heterostructure (SrRuO₃/PMN-PT/PZT/SrRuO₃) was deposited on a 0.5mm thick and (001) oriented SrTiO₃ substrate. The SrTiO₃ substrates were pre-treated prior to deposition to achieve TiO₂ single termination using the method developed by Koster and co-workers [16]. The substrates were heated by fixing them on the steel block type hot stage (substrate holder) using silver epoxy. The temperature was measured using a thermocouple embedded inside the substrate holder. All films have been deposited by Pulsed Laser Deposition (PLD) using a KrF Excimer laser operating at 248nm. The complete heterostructure was deposited without breaking the vacuum to avoid unwanted contaminations. The layers stack were cooled down immediately after deposition from deposition temperature to room temperature in an one bar oxygen ambient using cooling rate of 10°C/minute. The specific growth conditions for SrRuO₃, PZT and PMN-PT films and details about the pulsed laser deposition can be found in Chapter 2. The PZT doped with iron and niobium in addition to undoped PZT were used as interfacial layer in this study were

deposited using similar fabrication conditions and are given in table 5.1.

Table 5.1 Specific growth conditions of SRO electrode, PZT interfacial layer and PMN-PT films.

Parameters	SrRuO ₃	PZT	PMN-PT
Ambient	Oxygen	Oxygen	Oxygen
Laser energy density (J/cm ²)	2.50	3.5	2.0
Temperature (°C)	600	600	585
Target-Substrate distance (cm)	4.90	6.0	6.0
Pressure (mbar)	0.13	0.10	0.270
Repetition rate (Hz)	4	2	4

5.2.2 Samples characterization

Structural properties and the epitaxial relationships were investigated by HR-XRD (PANalytical X¹pert PRO MRD). The in-plane and out-of-plane lattice parameters were derived from reciprocal maps. Ferroelectric capacitor devices (200×200μm²) were patterned by a standard photolithography process and structured by argon ion beam etching. Polarization-electric field (P-E) hysteresis loops were measured using a modified Sawyer Tower circuit (AixACCT TF Analyser 3000) at a frequency of 1kHz using a bipolar triangular pulse and with 150 kV/cm amplitude. Fatigue measurements were performed using a rectangular pulse train at a frequency of 10 kHz and using an amplitude of 150 kV/cm. The longitudinal piezoelectric coefficients ($d_{33\text{eff}}$) were obtained using a Polytec MSA-400 Micro Scanning Laser Doppler Vibrometer. The electric field vs. capacitance (E-C) measurements have been performed using Suss MicroTech PM300 probe station equipped with Keithley 4200 semiconductor characterisation at 10kHz frequency. The corresponding dielectric constants has been calculated from these E-C curves. More details about characterization techniques can be found in chapter 2.

5.3 Results and discussions

5.3.1 Structural properties

Figure 5.2(a) shows the θ - 2θ diffraction patterns of the epitaxial PMN-PT films deposited on an iron and niobium doped PZT interfacial layer, as well as with an undoped PZT interfacial layer. The reflections corresponding to the substrate, electrode, PMN-PT and PZT layers are indicated [Figure 5.2(b)]. The solid green lines are specify the reflection positions corresponding to the bulk materials. The diffractograms show the peaks corresponding to (001) growth orientation of PMN-PT and PZT films only. No diffraction peaks due to impurity phases (pyrochlore phase) or other orientations were observed for both (PMN-PT, PZT) ferroelectric materials. This demonstrates that the deposited films are perovskite phase and (001) orientation pure within the detection limits of our instrument.

The PZT interfacial layer reflections are shifted from the expected angle for c-axis oriented unstrained PZT. The peak shift towards a lower angle indicates a change in the out-of-plane lattice constant. Due to the difference in lattice parameters between the PZT interfacial layer ($a = 4.05\text{\AA}$) and the STO substrate ($a = 3.905\text{\AA}$), the deposited PZT interfacial layers are under in-plane compressive strain causing an increase in the out-of-plane lattice constant. It is noted that the SRO bottom electrode is fully strained to the substrate, as was concluded from the peak shift from the unstrained value. The lattice parameters for the different PZT interfacial layers, derived from reciprocal space maps, are shown in table 5.2. We note that the in-plane lattice parameter (a) and out-of-plane lattice parameter (c) of the interfacial layer decrease slightly when changing the composition from undoped, Fe-doped to Nb-doped, although the c/a ratio does not change. This corresponds to a decrease of the average unit cell volume in this order of doping.

Similarly, the PMN-PT reflections are also shifted from the expected angle of unstrained, rhombohedral bulk PMN-PT. The shift

of the PMN-PT diffraction peak towards a higher angle as compared to the unstrained value indicates that the deposited films are under tensile stress. The highest tensile stress was observed for the PMN-PT films deposited on the undoped PZT interfacial layer, while the lowest tensile stress was observed for the films on the Nb-doped interfacial layer. The lattice parameters derived from reciprocal space maps for PMN-PT films are given in table 5.2. The decreasing trend of the in-plane lattice parameter reflects the change in the in-plane lattice parameter of the (doped) PZT interfacial layers. Consequently the c/a ratio is most reduced for the undoped PZT layer and least for the Nb-doped PZT.

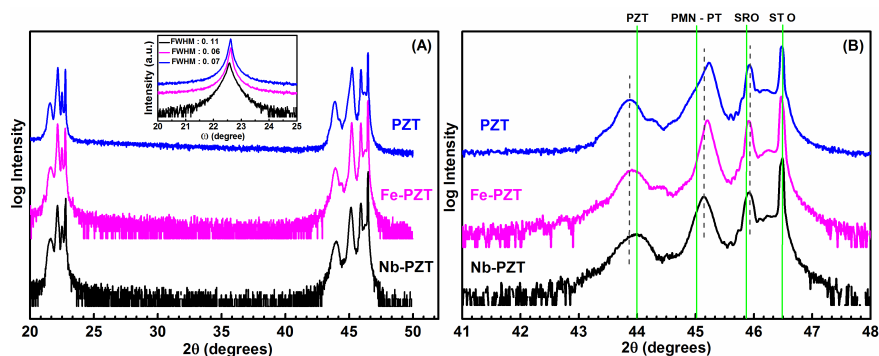


Figure 5.2: XRD pattern of epitaxial PMN-PT films deposited using Nb doped, Fe doped and undoped PZT interfacial layer with inset showing PMN-PT rocking curves for (002) reflections (a) Zoom in of the (002) diffraction peaks indicating peak shift (variation in out of plane lattice constants) based on nature of the interfacial layer material. Bulk peak positions are marked with solid green lines and peak shifts are indicated by the dotted grey lines (b).

The in-plane and out of plane lattice constants for both PZT interfacial layer and PMN-PT films derived from reciprocal space maps are summarized in table 5.2.

Table 5.2 In-plane and out-plane lattice parameters of PZT interfacial layers and PMN-PT films deposited on SRO electroded STO substrates.

Sample	Interfacial layer (PZT)				PMN-PT			
	a (Å)	c (Å)	V_{uc} (Å ³)	c/a	a (Å)	c (Å)	V_{uc} (Å ³)	c/a
Bulk	4.05	4.11	67.41	1.015	4.022	4.022	65.06	1.000
undoped	4.043	4.129	67.49	1.021	4.035	4.007	65.24	0.993
Fe-PZT	4.041	4.125	67.36	1.021	4.030	4.009	65.11	0.995
Nb-PZT	4.038	4.122	67.21	1.021	4.024	4.014	65.00	0.998

The rocking curve measurements were also performed on these samples and are shown in the inset of the figure 5.2 (a). Rocking curves corresponds to PMN-PT films exhibit full width at half maximum (FWHM) of 0.06° - 0.11° for (002) ω -scan and 0.70° for (101) ϕ -scan respectively. Commercially available PMN-PT single crystals have FWHM of 0.14° and 0.27° of the rocking curve and ϕ -scan respectively [23]. The FWHM value for the reflections corresponds to PMN-PT in-plane scans (ϕ -scans) for our deposited PMN-PT films are broader as compared to bulk PMN-PT single crystals. The in-plane lattice parameters of the PZT interfacial layers are slightly bigger than bulk in-plane lattice parameters of PMN-PT ceramics. So the PMN-PT unit cell is stretched in-plane to fit on top of the unit cell of PZT interfacial layer. Due to this stretching, the in-plane diffraction peaks are broader as compared to bulk PMN-PT single crystals. The narrowness of the rocking curves corresponds to PMN-PT films distinguishably demonstrates the high degree of oriented growth and excellent crystalline quality of the deposited epitaxial PMN-PT films.

5.3.2 Ferroelectric and piezoelectric properties

The ferroelectric hysteresis loops recorded for the different samples are shown in the figure 5.3 (a).

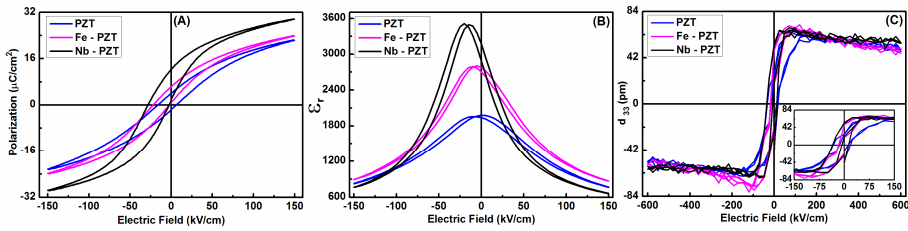


Figure 5.3: Polarization hysteresis loops of the PMN-PT films deposited using doped and undoped PZT interfacial layer (a) relative dielectric constant curves derived from electric field versus capacitance measurements (b) d_{33} loops with zoom in for epitaxial PMN-PT films deposited using doped and undoped PZT interfacial layers (c). All loops are measured before aging of the samples.

It is seen that the polarization hysteresis loops are notably different. A significantly higher polarization was observed for the PMN-PT film on the Nb-doped PZT interfacial layer. Also the polarization of the PMN-PT films on Fe-PZT is slightly higher than of the films on undoped PZT. Another difference is the presence of a self-bias field which value depends on the type of PZT material used as interfacial layer. The presence of a self-bias is of great importance, because it affects the performance of devices made from these films. Due to the shift of the polarization hysteresis loop, the self-bias increases the positive or negative remanent polarization (positive in our case) [17]. The maximum value of the dielectric constant is strongly dependent on the type of interfacial layer, reaching nearly double the maximum value for the Nb-doped PZT interfacial layer, as compared to the undoped layer. On the other hand the increased built-in bias reduces the relative dielectric constant at zero field, due to the loop shift, as is seen in figure 5.3(b). At high fields the dielectric constant become approximately equal, reflecting the nearly parallel slopes of the P-E loops at high fields. Besides this, it was reported that films with built-in bias are more robust against depolarization due to voltage and temperature excursions [18-19], however as seen in the next paragraph this is not the case for our devices, where it is shown

that the device with least self-bias is most stable. The ferroelectric and piezoelectric properties are summarized in table 5.3.

Table 5.3 The ferroelectric and piezoelectric properties of the epitaxial PMN-PT films deposited using doped and undoped PZT interfacial layers.

Sample	P(0) ($\mu\text{C}/\text{cm}^2$)	E_c , av. (kV/cm)	E_{sb} (kV/cm)	$\epsilon_{r, \max}$	$\epsilon_r @ 0\text{V}$	$d_{33, \text{eff.}}$ pm/V
Nb-PZT	19.16	12.81	-15.31	3455	3030	67
Fe-PZT	13.56	9.95	-11.96	2800	2743	74
Undoped	12.42	11.32	-4.92	1970	1958	66

The self-bias is expected to be due to the combined effect of the flexoelectric effect, caused by the strain gradient layer in the interfacial layer and a charge doped layer. The effect of the strain gradient layer is likely to be comparable between the different interfacial layers, since the thickness and (average) c/a ratio of these layers are equal. On the other hand the doping of the interfacial layer is different, either undoped, donor or acceptor doped. The doped layers show a significantly larger self-bias field than the undoped layer, but as is seen in the next section are also less stable upon field cycling. This indicates a change in the (defect) charge distribution. Similarly the variation in coercive field between the different samples can then be ascribed to the different domain wall pinning strength of (charged) defects.

The applied field dependence of the dielectric constant measured for epitaxial PMN-PT films deposited on doped and undoped PZT interfacial layers are very different. It is lowest for PMN-PT deposited on undoped PZT interfacial layer and highest for a Nb-PZT interfacial layer. The PMN-PT film deposited using PZT interfacial is under highest tensile strain and is lowest on Nb-PZT interfacial layer. The variation in the dielectric constant in our film is related with strain and is consistent with observation by Nagarajan and co-workers for epitaxial PMN-PT (90/10) films [22].

5.3.3 Ferroelectric response stability behaviour

The ferroelectric response stability (aging behaviour) of the epitaxial PMN-PT films on doped and undoped PZT interfacial layer were tested by subjecting them to a high number (10^8) of switching cycles. Aging behaviour in terms of remanent polarization, positive and negative coercive field [E_{c+} and E_{c-}], self-bias field [$E_{sb} = \frac{E_{c+} + E_{c-}}{2}$] and average coercive field [$E_{c.av} = \frac{E_{c+} - E_{c-}}{2}$] versus number of cycles are shown in figure 5.4.

The PMN-PT film on undoped PZT interfacial layer shows a very good ferroelectric response stability against the number of switching cycles. No change in the self-bias field was observed for these films, whereas the average coercive field only slightly increases, indicating a small increase in domain wall pinning, hence defect density. The epitaxial PMN-PT films on a Fe-PZT interfacial layer exhibit a small change in the built-in bias field, indicating that the charge and dipole density and/or distribution in the film slightly changes upon cycling. On the other hand the coercive field is very stable. Dipolar defect complexes, $\text{Fe}^{3+}\text{-V}_\text{O}$ and $\text{V}_{\text{Pb}}''\text{-V}_\text{O}$ are present in the Fe-doped PZT interfacial layer. These oxygen vacancies are very mobile and can therefore relatively easily be aligned in an external electric field. The high stability of the ferroelectric properties of the sample with Fe-doped PZT layer, indicates that any redistribution of the charge apparently already happens in the first cycles, after which the distribution is stable upon cycling. The film with Nb-doped PZT interfacial layer shows a similar change in coercive field as for the undoped PZT layer, whereas the self-bias field shows the behaviour of the Fe-doped PZT layer. The charge and dipole distribution of the much less mobile $\text{V}_{\text{Pb}}''\text{-Nb}_{\text{Ti}}$ defects only change upon long-term cycling, as is reflected in the long-term change of self-bias field and coercivity.

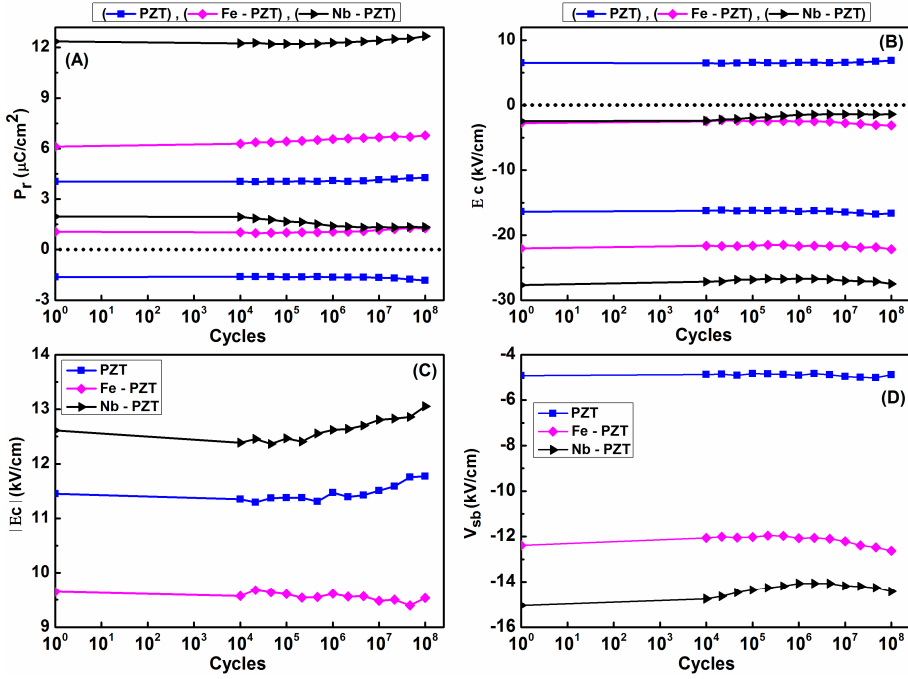


Figure 5.4: Remanent polarization verses number of cycles performance of epitaxial PMN-PT films deposited using doped and un-doped PZT interfacial layer (a) Coercive field verses number of cycles performance (b) Average coercive field verses number of cycles (c) and Self-bias verses number of cycles (d).

5.4 Effect of Nb-PZT layer thickness on PMN-PT properties

The highest self-bias field was observed for devices with a Nb-PZT interfacial layer, compared to the Fe-PZT and undoped PZT interfacial layer samples. To investigate the effect of the Nb-PZT interfacial layer thickness on the ferro and piezoelectric properties of PMN-PT films, layer stacks (SRO/PMN-PT/Nb-PZT/SRO) with four different thicknesses of Nb-PZT interfacial layer (13nm, 25nm, 50nm and 100nm) were fabricated using SRO electroded STO substrates.

5.4.1 Structural properties

Figure 5.5(a) shows the θ - 2θ diffraction patterns of the epitaxial PMN-PT films with different thicknesses of Nb-PZT interfacial layer. The reflections correspond to the substrate, electrodes, PMN-PT and Nb-PZT interfacial layer [Figure 5.5(b)]. The solid green lines indicate the reflection positions of the bulk materials. The reflections correspond to (001) growth of all layers. No diffraction peaks from impurity phase (pyrochlore phase) or other orientations were observed. This demonstrates that the deposited films are perovskite phase and (001) orientation pure with in the detection limits of our instrument.

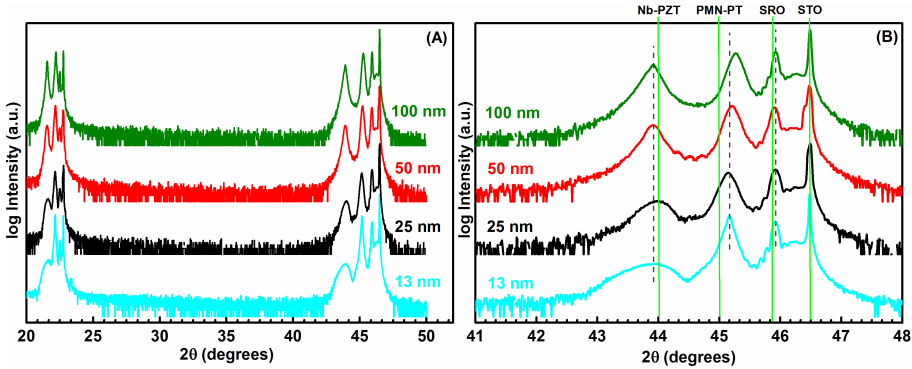


Figure 5.5: XRD patterns of PMN-PT films deposited using four different thicknesses of Nb-PZT interfacial layer (a) Zoom in of the (002) diffraction peaks area indicating peak shift (variation in out of plane lattice constants) based on interfacial layer thickness. The bulk peak positions are marked with solid green lines while dotted lines are drawn to highlight peak shifts (b).

The Nb-PZT interfacial layer reflections are slightly shifted from the unstrained PZT value. This indicates that these films are in-plane slightly compressively strained, giving rise to a small expansion of the unit cell in the out-of-plane direction. This is expected because of the in-plane compressive strain imposed by the STO substrate. A broad shoulder on the Nb-PZT reflection towards lower angle side is

also observed for all Nb-PZT layer thicknesses. The shoulder indicates the presence of a strain gradient in the interfacial layer. The strain relaxes with increasing film thickness and is typically observed in epitaxial PZT films on STO [20]. The formation of structural defect like misfit dislocations are generally believed to be the reason for the strain relaxation [21]. The thickness of the strain gradient layer is of the order of the thinnest layer, 10-20nm. .

Similarly, the XRD reflections of the PMN-PT films deposited on top of different thicknesses of Nb-PZT interfacial layer are also shifted from the bulk angle of unstrained, rhombohedral PMN-PT. The interfacial layer thickness dependent peak shift of the PMN-PT films can also be observed and is highlighted by the dotted grey line. This demonstrates interfacial layer thickness dependent decay in the out of plane PMN-PT lattice parameter. The PMN-PT film ($a \approx 4.02\text{\AA}$) deposited on top of Nb-PZT interfacial layer ($a \approx 4.05\text{\AA}$) is under in-plane tensile strain. The in-plane tensile strain increases in PMN-PT film increases with the increase in the interfacial layer thickness. Due to strain relaxation with the formation of structural defects with the increase in interfacial layer thickness, the in-plane lattice mismatch between interfacial layer and PMN-PT increases. This results higher tensile strain in the PMN-PT film. The lattice parameters derived from the reciprocal space maps for PMN-PT and Nb-PZT interfacial layers are summarized in table 5.4.

Table 5.4 In-plane and out-plane lattice parameters for Nb-PZT interfacial layers and PMN-PT films deposited on SRO electroded STO substrates.

t (nm)	Nb-PZT interfacial layer				PMN-PT (t = 200nm)			
	a (\AA)	c (\AA)	V_{uc} (\AA^3)	c/a	a (\AA)	c (\AA)	V_{uc} (\AA^3)	c/a
13	4.025	4.137	67.02	1.028	4.021	4.013	64.88	0.998
25	4.038	4.122	67.21	1.021	4.024	4.014	65.00	0.998
50	4.050	4.119	67.56	1.017	4.029	4.007	65.04	0.995
100	4.053	4.113	67.56	1.015	4.035	4.004	65.19	0.992
Bulk	4.05	4.11	67.41	1.015	4.022	4.022	65.06	1.00

Figure 5.5(a) shows the in-plane and out-of-plane lattice parameters of the interfacial layer and PMN-PT layer as function of thickness of the interfacial layer. It is seen that the lattice parameters of the Nb-PZT layer relax to approximately the bulk PZT value after 30-50nm. On the other hand the tensile strain in the PMN-PT approximately linearly increases with Nb-PZT layer thickness. Figure 5.5 (a) shows the c/a ratio of the Nb-PZT and the PMN-PT layer. Here the same trend is observed. The unit cell volume is shown in figure 5.5 (c). Again V_{uc} of Nb-PZT saturates to a value slightly larger than of bulk undoped PZT, which suggests that the unit cell volume of Nb-doped PZT is slightly enhanced over that of undoped PZT. The V_{uc} of PMN-PT shows an approximately linearly increase with Nb-doped PZT layer thickness and with strain.

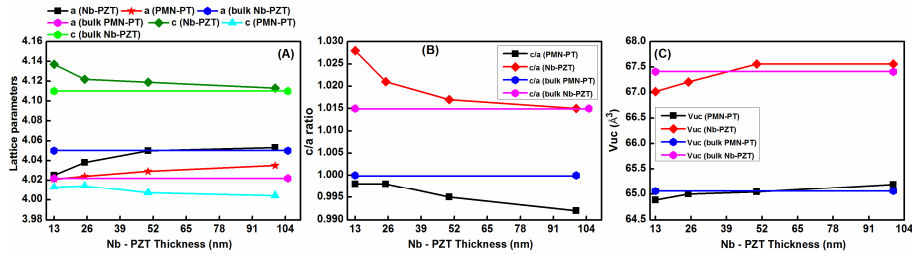


Figure 5.5: Lattice parameters of Nb-PZT and PMN-PT (a) c/a ratio of Nb-PZT and PMN-PT (b) Unit cell volume of Nb-PZT and PMN-PT (c).

The rocking curve measurements (not shown) on PMN-PT films show a full width at half maximum (FWHM) of $0.4^\circ - 0.11^\circ$ for the (002) ω -scans. The narrowness of the rocking curves demonstrates the high degree of oriented growth and the excellent crystalline quality of the deposited epitaxial PMN-PT films. The rocking curve measurements also exhibit excellent sample to sample reproducibility and thus of crystalline quality of the deposited heterostructures also in this study.

5.4.2 Ferroelectric and piezoelectric properties

The ferroelectric hysteresis loops [(Fig. 5.6(a))], relative dielectric constants curves derived from the electric field versus capacitance curves [(Fig. 5.6(b))] and d_{33} loops [(Fig. 5.6(c))] recorded for the Nb-PZT/PMN-PT capacitor devices are shown in figure 5.6.

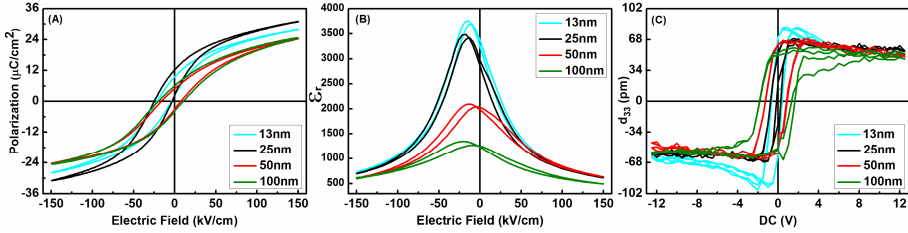


Figure 5.7: Electric field versus polarization hysteresis loops of PMN-PT films deposited on top of four different thicknesses of Nb-PZT interfacial layer (a) relative dielectric constant versus electric field curves (b) and d_{33} loops (c).

The ferroelectric hysteresis loops are significantly different for different Nb-PZT layer thicknesses. Higher self-bias field was observed for the PMN-PT films deposited on thinner interfacial layer as compared to thicker ones. The self-bias field for the 25nm interfacial layer is higher than for the 13nm interfacial layer. This is most probably due to higher number of defected dipole in thicker films (25nm) compared to thinner ones (13nm). With further increase of the interfacial layer thickness (50nm and 100nm), the strain in the Nb-PZT films relaxes towards the Nb-PZT/PMN-PT interface due to the formation of structural defects [21]. Due to the strain relaxation of the Nb-PZT interfacial layer with increasing thickness, the in-plane crystal lattice mismatch with the PMN-PT layer increases which results in a higher tensile strain in the PMN-PT films. The total polarization of the device arises from the thickness weighted sum of the polarizations in the Nb-PZT and PMN-PT layer. The polarization contribution from the Nb-PZT layer scales as $t_{Nb-PZT}/(t_{Nb-PZT} + t_{PMN-PT})$, thus varies from 13/213 to 100/300.

But the average length of the out-of-plane component of the Nb-PZT polarization vector decreases because the average compressive strain in the Nb-PZT decreases. This reduces the tetragonality of the unit cell and thus the polarization strength. Further the average tensile strain in the PMN-PT increases with Nb-PZT layer thickness. This causes the polarization vector to rotate into plane, reducing the measured out-of-plane component. This explains the overall reduction in polarization with increasing Nb-PZT thickness. However for small thicknesses the balance between the Nb-PZT and PMN-PT layer contributions appears to be such that it gives a larger polarization for the 25nm Nb-PZT layer than for the 13nm layer.

A second feature of the loops are the differences in the self-bias fields, which are much more negative for the thin Nb-PZT interfacial layers than for the thick layers. The self-bias field is likely to be due to the combined effect of the charged Nb-PZT layer and the strain-gradient layer which contributes to the build-in electrical field through the flexo-electric effect [20]. It is not straightforward to disentangle to combined effect of these two mechanisms.

The high slopes and high polarization of the PE-loops of the devices with thin Nb-PZT layers are reflected in the high peaks in the relative dielectric curves of these devices. Also here the shift in the electric field is observed. This shift reduces the relative dielectric constant at zero bias somewhat. Nagarajan and co-workers investigated the effects of strain on the dielectric properties of epitaxial PMN-PT (90/10) films and increase of the zero-field dielectric constant with strain relaxation in the PMN-PT was demonstrated [22], as we see here as well for decreasing Nb-PZT thickness. The ferroelectric and dielectric and piezoelectric properties summarised in table 5.5.

Table 5.5 The ferroelectric and piezoelectric properties of the epitaxial PMN-PT films deposited using four different thicknesses of Nb-PZT interfacial layers.

Nb-PZT thickness	P (0) [$\mu\text{C}/\text{cm}^2$]	E_c , av. (kV/cm)	E_{sb} (kV/cm)	ϵ_r (max)	ϵ_r (0V)	$d_{33,\text{eff}}$ pm/V
13 nm	16.70	8.88	-12.77	3722	3308	88
25 nm	19.12	12.81	-15.31	3455	3030	67
50 nm	13.55	11.88	-4.50	2070	2005	66
100 nm	14.03	15.23	-5.11	1310	1234	62

5.4.3 Ferroelectric response stability analysis

The ferroelectric response stability (aging behaviour) of the epitaxial PMN-PT films with different thicknesses of the Nb-doped PZT interfacial were tested by subjecting them to a high number (10^8) of switching cycles. Aging behaviour in terms of remanent polarization, coercive field, self-bias field, and average coercive field are shown in figure 5.7.

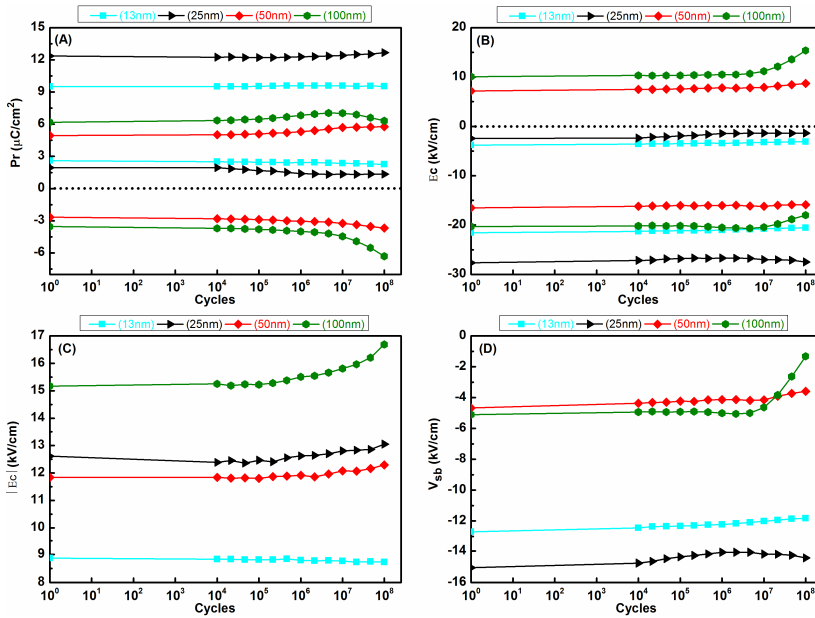


Figure 5.7: Remanent polarization verses number of cycles performance of epitaxial PMN-PT films deposited using different thicknesses of Nb- PZT interfacial layer (a) Coercive field verses number of cycles performance (b) $E_{c,av}$ verses number of cycles (c) and Self-bias verses number of cycles (d).

The PMN-PT films deposited on a 13nm thick Nb-PZT interfacial layer show a very good ferroelectric response stability. Hardly any change in remanent polarization, coercive field and self-bias field can be observed in this case. However with the increase in the interfacial layer thickness, a change in the ferroelectric response upon cycling is observed. This variation increases slightly with increasing interfacial layer thickness, but for the largest thickness a rapid change in properties sets in above about 3×10^6 cycles. The coercive field and increases significantly, indicating an increase of domain wall pinning, which we attribute to a change of the defect charge distribution in the Nb-PZT layer under the cycling electrical field. The increased mobility of the defect charges is likely related to the more relaxed strain state of the major part in this film. We expect that the change in self-bias field is related to the same effect. The slight decay in the self-bias field in the beginning is due to depletion of the space charges as a result of switching process. With the increase in the number of switching This analysis demonstrates that PMN-PT films deposited on top of a thin interfacial layer show superior ferroelectric response stability compared to films deposited on thicker interfacial layers.

5.5 Conclusions

Perovskite phase and (001) orientation pure epitaxial PMN-PT films have been prepared on a STO substrate, using hard and soft doped PZT interfacial layer in addition to undoped PZT interfacial layer. PMN-PT films deposited on an undoped PZT layer are under slight tensile strain, which decays slightly for the PMN-PT films deposited on a Fe-PZT and Nb-PZT interfacial layer respectively. Interfacial layers are under compressive strain due to difference of lattice parameters between interfacial layer and STO substrate. The highest compressive strain was measured in the Nb-PZT layer while the lowest was observed in the undoped PZT interfacial layer. These strains play a key role in the differences in ferroelectric, dielectric and

piezoelectric properties of epitaxial PMN-PT thin film based heterostructures, STO//SRO/(doped)PZT/PMN-PT/SRO.

PMN-PT films were also deposited on a Nb-PZT interfacial layer of varying thicknesses. These heterostructures also show strain variations in both ferroelectric layers (PMN-PT, Nb-PZT). With increasing interfacial layer thickness, the (average) strain relaxes in this layer. This strain relaxation causes an increasing crystal lattice parameter mismatch between PMN-PT and Nb-PZT layer. This causes a higher tensile strain in the PMN-PT films with increasing interfacial layer thickness, which has a noticeable effect on the ferroelectric and dielectric of the PMN-PT films. This strain behavior is consistent which was observed in above case.

It is evident from the investigations reported in chapter 4 and 5 that crystal lattice strain (strain imposed by mismatch of lattice constants) affects the ferroelectric, dielectric and piezoelectric properties of PMN-PT films significantly.

5.6 References

- [1] W. L. Warren, G. E. Pike, K. Vanheusden, D. Dimos, B. A. Tuttle, J. Robertson, Defect dipole alignment and tetragonal strain in ferroelectrics, J. Appl. Phys. 79 (1996) 9250.
- [2] D. Damjanovic, The Science of Hysteresis, 01 (2005) 337.
- [3] B. Jaffe, W. R. Cook and H. L. Jaffe, piezoelectric ceramics, Academic Press INC., New York, USA (1971).
- [4] Piezoelectric Ceramics: Principals and applications, APC International Ltd, Pennsylvania, USA (2002).
- [5] K. Carl, K. H. Hardtl, Electrical after effects in Pb(Ti, Zr)O₃ ceramics, Ferroelectrics, 17 (1977)473.
- [6] U. Robels and G. Arlt, Domain wall clamping in ferroelectrics by orientation of defects, J. Appl. Phys. 73 (1993) 3454.
- [7] D. Damjanovic, Ferroelectric, dielectric and piezoelectric properties of ferroelectric thin films and ceramics, Rep. Prog. Phys., 61 (1998) 1267.

- [8] Xin Wan, Tailored piezoelectric thin films for energy harvester, PhD Thesis (2013), University of Twente, [ISBN: 978-90-365-1423-1].
- [9] M. D. Nguyen, T. Q. Trinh, M. Dekkers, E. P. Houwman, H. N.V and G. Rijnders, Effect of dopants on ferroelectric and piezoelectric properties of lead Zirconate titanate thin films on Si substrates, *Ceramics International*, 40 (2014)1013.
- [10] T. Haccart, D. Remiens and E. Cattan, Substitution of Nb doping on the structural, microstructural and electrical properties in PZT films, *Thin Solid Films*, 423 (2003) 235.
- [11] Z. X. Zhu, C. Ruangchalemwong, J. F. Li, Thickness and Nb-doping effects on ferro and piezoelectric properties of highly a-axis oriented Nb-doped $\text{Pb}(\text{Zr}_{0.3}\text{Ti}_{0.7})\text{O}_3$ films, *Journal of Applied Physics*, 104 (2008) 054107.
- [12] C. Ruangchalemwong, J. F. Li, Z. X. Zhu, F. Lai, S. Muensit, Enhanced ferro- and piezoelectric properties in (100)-textured Nb-doped $\text{Pb}(\text{Zr}_x\text{Ti}_{1-x})\text{O}_3$ films with compositions at morphotropic phase boundary, *Thin Solid Films*, 517 (2009) 6599.
- [13] S. B. Majumder, B. Roy, R. S. Katiyar, and S. B. Krupanidhi, Effect of acceptor and donor dopants on polarization components of lead Zirconate titanate thin films, *Appl. Phys. Lett.* 79 (2001) 239.
- [14] W. Bai, X. J. Meng, T. Lin, L. Tian, C. B. Jing, W. J. Liu, J. H. Ma, J. L. Sun and J. H. Chu, Effect of Fe-doping concentration on microstructure, electrical, and magnetic properties of $\text{Pb}(\text{Zr}_{0.5}\text{Ti}_{0.5})\text{O}_3$ thin films prepared by chemical solution deposition, *J. Appl. Phys.* 106 (2009) 124908.
- [15] M. Dawber, J. F. Scott, A model for fatigue in ferroelectric perovskite thin films, *Appl. Phys. Lett.*, 76 (2000) 1060.
- [16] G. Koster, B. L. Kropman, G. J. H. M. Rijnders, D. H. A. Blank, and H. Rogalla, *Appl. Phys. Lett.* 73 (1998) 2920.
- [17] Z. Zahang, J. H. Park, S. Trolier-McKinstry, *MRS Proc. Ferroelectric thin films VIII*, 596 (2000) 73.

- [18] R. G. Polcawich, S. Trolier-McKinstry, J. Mater. Res. 15, (2000) 2505.
- [19] R. G. Polcawich et al., IEEE Trans. Microwave Theory Tec. 55, (2007) 2642.
- [20] M. Boota, E.P. Houwman, M. Dekkers, M. Nguyen and G. Rijnders, , Appl. Phys. Lett., 104 (2014) 00000.
- [21] S. Gariglio, N. Stuki, J. M. Triscone and G. Triscone, Appl. Phys. Lett., 90 (2007) 202905.
- [22] V. Nagarajan, C. S. Ganpule, B. Nagaraj, S. Aggarwal, S. P. Alpay, and A. L. Roytburd, Appl. Phys. Lett., 75 (1999) 4183.
- [23] S. H. Baek, D. M. Kin, V. A. Aksyuk, R. R. Das, S. D. Bu, ... and C. B. Eom, Science, 334 (2011) 958.

6.

Substrate induced strain in PMN-PT films

Chapter Overview:

Difference of thermal expansion coefficients between substrate and clamped epitaxial films give rise to strain upon cooling from growth temperature to room temperature. To study the effect of thermal (residual) strain on structural, ferro and piezoelectric properties of epitaxial PMN-PT (67/33) films, heterostructures were prepared on SrRuO_3 electroded various substrates in a large misfit strain range using PZT(52/48) as interfacial layer. The deposited films are perovskite phase and (001) orientation pure in the entire investigated range. The ferroelectric and piezoelectric investigations shows influence of internal stresses imposed by the nature of the substrate on these properties.

This chapter to be submitted as

- The effect of substrate induced strain on the ferroelectric and piezoelectric behavior of epitaxial PMN-PT thin films.

6.1 Introduction

Epitaxial PMN-PT thin films based heterostructures generally and reported in this dissertation explicitly are deposited at high temperature (585 °C). Upon cooling from growth temperature to room temperature, the difference in crystal lattice parameters and/or thermal expansion coefficients between substrate and clamped film give rise to strain in the films universally known as misfit and/or residual strain [1]. In previous chapters (chapters 4 and 5), the impact of crystal lattice strain (strain imposed by mismatch of lattice parameters) on structural, ferro and piezoelectric properties of epitaxial PMN-PT films grown on SrTiO₃ substrates is discussed. In this chapter, the influence of the substrate induced strain on the epitaxial PMN-PT(67/33) films will be discussed.

The strain imposed by the mismatch between substrate and film in ferroelectric thin films usually and in epitaxially films particularly has a strong influence on crystal structural, domain structure, ferroelectric and piezoelectric properties. The knowledge of strain factors like misfit strain and/or thermal strain and the transformation strain occurring near Curie temperature is crucial in tailoring the domain structure and consequently physical properties of ferroelectric thin films [2-3].

Epitaxial ferroelectric thin films are typically deposited at high temperature (600 °C) and are in paraelectric phase. During cooling down from growth temperature to room temperature, films transform from paraelectric phase to ferroelectric phase and large spontaneous strain emerges during this phase transformation [4]. The difference of thermal expansion coefficient restricts the free in-plane shrinkage of the deposited film. This leads to significant strain in the film that effects the unit cell parameters and ferroelectric domain formation [5]. The lattice parameters of the film and the substrate can be analyzed as a function of temperature to gain the insight about the thermal strain and strain relaxation process. With increasing film thickness, the

lattice strain (strain due to difference of lattice parameters) relaxes more rapidly as compared to thermal strain with the formation of structural defects like misfit dislocations and/or ferroelectric domains [6]. Due to higher substrate thickness as compared to deposited films, the impact of the substrate induced strain on ferro and piezoelectric properties of the deposited films is generally more prominent. The epitaxial strain of different substrates can be used to control the ferroelectric domain fraction and hence the ferroelectric and piezoelectric properties of these films can be tuned [7].

The effect of crystal lattice and/or residual strain and strain relaxation mechanisms in ferroelectric thin films and its effect on physical properties was studied by various research groups. The mechanism of strain relaxation in epitaxial PZT thin film with the formation of misfit dislocations at growth temperature as well as with the formation of an a/c/a/c polydomain structure had been observed. During thin film growth, part of the strain energy is relaxed with the formation of misfit dislocation at growth temperature. After film deposition, the strain relaxation was also observed with the formation of polydomain structure at the paraelectric to ferroelectric phase transformation stage. The c-lattice parameter decreases when the film relaxes via polydomain formation. This consequences decay in c/a ratio of the ferroelectric layer which effects the static and dynamic ferroelectric response. The epitaxial strain also relaxes with the increase of film thickness [8].

Lee and co-workers investigated and found the strong effect of tensile misfit strain on domain formation of epitaxial PbTiO_3 thin films deposited using pulsed laser deposition on MgO substrates. They studied the effect of elastic misfit strain imposed by heteroepitaxy on domain formation. The strain relaxation with increasing film thickness via domain formation had been observed in this case using synchrotron radiations. A close relation between the domain population and misfit strain had been recorded in this case. The tensile strain facilitate the formation of a-domains in very thin films [9]. Subsequently Kim and co-workers studied the effect of compressive

misfit strain on ferroelectric domain structure of epitaxial PbTiO_3 thin films and obtained almost pure c-domain structure. The compressive strains acts in opposite way and facilitate the formation of c-domain. The strain relaxation with increasing film thickness consequences reduction in c-domains abundance. The c-domain fraction found to be critical for higher piezo response rather than domain switching from a-domain to c-domain [10]. The tensile strain found to facilitate a-domain formation and compressive strain behaves in opposite way in pulsed laser deposited epitaxial PbTiO_3 thin films.

Bai and co-workers found robust impact of epitaxial strain on BaTiO_3 films deposited by pulsed laser deposition. They found that epitaxial strain energy increase the phase transition temperature significantly. Strain relaxation by insertion of buffer layer significantly reduces the phase transition temperature in this material system [11].

The impact of mechanical constraints on dielectric and piezoelectric properties of pulsed laser deposited epitaxial PMN-PT (90/10) films was studied by the Nagarajan and co-workers on LaSrCoO_2 electroded LaAlO_3 substrate. They observed gradual stain relaxation with increasing film thickness and improvement in crystallinity with in the films. The strain relaxation with increase in film thickness results decay in phase transition temperature. The significant enhancement in dielectric and piezoelectric response with strain relaxation was measured in these films [12]. This study was further extended to investigate the impact of substrate induced strain (compressive or tensile) on dielectric and piezoelectric properties of epitaxial PMN-PT(90/10) films. For these investigations, PMN-PT films were deposited using LaAlO_3 , LSAT, STO and MgO substrates. XRD analysis indicates that PMN-PT films deposited on LaAlO_3 , LSAT, STO substrates are under compressive strain while on MgO are under tensile strain. The strong dependence of the dielectric and piezoelectric properties on misfit between substrate and PMN-PT films was observed. The enhancement of dielectric and piezoelectric

properties with decay in the in-plane compressive strain was observed in this study [13].

In this chapter, experimental study is presented focusing on the effect of substrate induced strain on crystal structure, ferro and piezoelectric properties of epitaxial PMN-PT(67/33) films. For this analysis, the PMN-PT thin films were prepared using PZT(52/48) interfacial layer on SrRuO₃ electroded various substrates in a large misfit strain range. The PZT(52/48) had been selected to use as interfacial layer due to its close in-plane lattice matching with PMN-PT (67/33). The use of interfacial layer expected to minimize/eliminate the effect of strain induced by difference of crystal lattice parameters between PMN-PT and SrRuO₃ bottom electrode. The deposited heterostructures were analyzed focusing on the impact of difference of thermal expansion coefficients on structure, ferroelectric and piezoelectric properties of epitaxial PMN-PT thin films.

6.2 Substrates and substrate pre-treatments

To study the substrate induced strain on structure, ferroelectric and piezoelectric properties of epitaxial PMN-PT (67/33) films, the selected substrate with their lattice parameters, crystal structure and thermal expansion coefficients are summarized in table 6.1.

Table 6.1: Lattice parameters of PMN-PT film and the substrates at room temperature (RT) used in these experiments together with their thermal expansion coefficients [13-15].

<i>Material</i>	<i>Bulk lattice constants a (Å)</i>	<i>Crystal Structure</i>	<i>TEC ($\times 10^{-6} K^{-1}$)</i>
PMN-PT (67/33)	4.02	Pseudo-Cubic	≈ 10
CeO ₂ /YSZ/Si	5.43	Cubic	2.6
LaAlO ₃	3.79	Cubic	10
LSAT	3.87	Cubic	12
NdGaO ₃	3.86 _(pc)	orthorhombic	9

SrTiO ₃	3.905	Cubic	11
DyScO ₃	3.95 _(pc)	orthorhombic	8.4
MgO	4.212	Cubic	14.8
CeO ₂ /YSZ	5.125	Cubic	11.4

Before thin films growth, SrTiO₃, LSAT, NdGaO₃ and DyScO₃ substrates were pre-treated to get single termination (B-site) by using methods developed by Koster et. al. and Kleibeuker et. al. Rest of the substrates were ultrasonically cleaned using acetone and ethanol prior to deposition to remove surface contaminations except MgO [16-18].

6.3 Experimental procedure

6.3.1 Samples fabrication

PMN-PT/PZT (200nm/25nm) bilayer stack is sandwiched between 100nm SrRuO₃ electrodes. It is notable here that PZT (52/48) layer is sandwiched between PMN-PT bottom electrode. The used substrates to deposit heterostructure (SrRuO₃/PMN-PT/PZT/SrRuO₃) include MgO(001) denoted as B1, CeO₂ buffered YSZ (001)-B2, LSAT(001)-B3, LaAlO₃(001)-B4, DyScO₃(001)_{pc}-B5, SrTiO₃(001)-B6, NdGaO₃(001)_{pc}-B7 and CeO₂/YSZ bilayer buffered silicon (001)-B8. The SRO used as bottom electrode can grow with cube on cube epitaxial relation on all selected oxide substrates. In case of B2 and B8, buffer layers were applied to overcome large lattice mismatch between substrate and SRO bottom electrode. The (001) orientation of PMN-PT films on silicon and YSZ substrate (B2 and B8) was achieved using (001) oriented SRO film which was fabricated using growth method developed by Dekkers and co-workers [19]. The complete layer stack was deposited subsequently to avoid un-wanted contaminations. Substrates were heated by fixing them using silver epoxy on a substrate holder and deposition temperature refers to the temperature measured by thermocouple embedded inside substrate

holder. All samples have been deposited by Pulsed Laser Deposition (PLD) using a KrF Excimer laser operating at 248nm. The layer stacks have been cooled down immediately from deposition temperature to room temperature in oxygen ambient using 1bar pressure with cooling rate of 10°C/minute. The specific growth conditions for SrRuO₃, PZT and PMN-PT films and further details about deposition system (Pulsed Laser Deposition) can be found in chapter 2.

6.3.2 Samples characterization

Structural properties and epitaxial relationship were investigated by HR-XRD (PANalytical X¹pert PRO MRD). The in-plane and out of plane lattice parameters were derived from reciprocal space maps. Device in ferroelectric capacitor geometry (200×200μm²) were patterned by standard photolithography process and structured by argon ion beam etching. Polarisation-electric field (P-E) hysteresis loops were measured using a modified Sawyer Tower circuit (AixACCT TF Analyser 3000) at a frequency of 1kHz using a bipolar triangular pulse and with 150 kV/cm amplitude. The longitudinal piezoelectric coefficients ($d_{33\text{eff}}$) were obtained using Polytec MSA-400 Micro Scanning Laser Doppler Vibrometer. The electric field vs. capacitance (E-C) measurements have been performed using Keithley 4200 at 10kHz frequency. The corresponding dielectric constants has been calculated from these E-C curves. More details about characterization techniques can be found in chapter 2.

6.4 Results and discussions

6.4.1 Structural properties

Figure 6.1(a) shows the θ -2 θ diffraction patterns of the epitaxial PMN-PT films deposited using PZT (52/48) interfacial layer. The zoom in the range of 41° – 49° (figure 6.1b) shows (002) reflections area on different substrates.

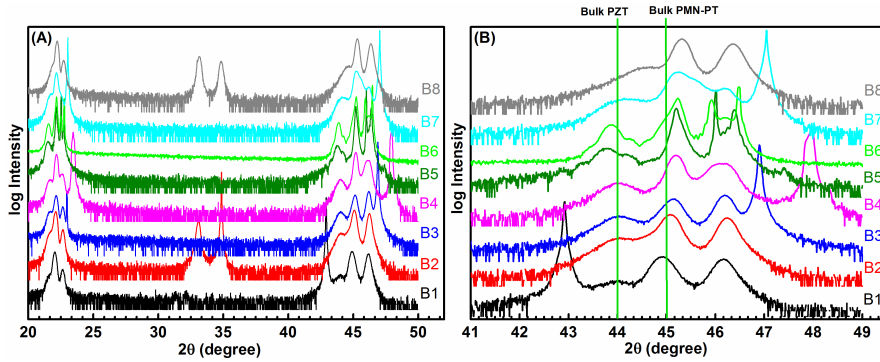


Figure 6.1: HR-XRD diffraction pattern of epitaxial PMN-PT films deposited on different substrates using PZT(52/48) as interfacial layer (a) Zoom in of the (002) diffraction peaks area. The bulk reflection positions for PZT(52/48) and PMN-PT are marked with solid green lines.

The diffraction peaks corresponds to substrates, electrodes, PZT and PMN-PT can be observed from XRD spectra. These spectra show diffraction peaks corresponding to (001) growth orientation only for both ferroelectric materials (PMN-PT and PZT). No diffraction peaks corresponds to impurity phases (pyrochlore phase) or other orientations were observed for both (PMN-PT, PZT) films. This analysis noticeably demonstrates that the deposited films are perovskite phase and (001) orientation pure within the detection limits of our instrument. The rocking curves (ω -scan) measurements for PMN-PT (002) reflection on different substrates were also performed (not shown) which show full width at half maximum (FWHM) in the range of 0.05° - 0.95° .

The solid green lines are drawn to specify the reflection positions corresponding to the bulk PZT (52/48) as well as PMN-PT (67/33) ceramics (figure 6.1 b). The reflections corresponds to PZT film are shifted from the expected angle corresponds to tetragonal unstrained bulk PZT. Similarly, the diffraction peaks corresponds to PMN-PT films are also shifted from the expected angle for unstrained pseudocubic bulk PMN-PT. The reflection corresponds to PMN-PT film deposited on MgO substrate is shifted towards lower angle

compared to bulk PMN-PT ceramics. However, the diffraction peaks representing PMN-PT film on all other substrate are shifted towards higher angle compared to the bulk PMN-PT ceramic. The PMN-PT diffraction peak shift is different for different substrates indicating substrate dependent strain variation in the deposited heterostructure. The diffractograms are arranged in a such a way that diffraction peak shift from lower angle towards higher angle can be observed easily.

The in-plane and out-of-plane lattice parameters are obtained from reciprocal space maps which were performed on the four fold reflections (103) of PZT and PMN-PT thin films. Furthermore, the (103) reciprocal space maps appears as one single reflection for the both ferroelectric materials (PZT, PMN-PT) with in the resolution of the diffracto-meter in all cases. This clearly demonstrates that no a- and c-domain formation is present in the crystallographic structure of the films. Since the composition is at morphotropic phase boundary, the PZT and PMN-PT unit cell is assumed to be nearly cubic for an unstrained free standing film. After cool down, the strain induced by the substrate, however distort the cubic unit cell and can be calculated using formula [20]

$$S_M = \frac{a - a_0}{a_0} \quad (6.1)$$

Where S_M refers to the misfit strain. The a is the measured in-plane lattice parameter while a_0 refers to the unstrained pseudocubic in-plane lattice parameter of the film. The unstrained pseudocubic in-plane lattice parameter (a_0) for PZT (52/48) interfacial layer and PMN-PT film is obtained from

$$a_0 = \sqrt[3]{(a \cdot a \cdot c)} \quad (6.2)$$

Where a and c are the measured in-plane and out-plane lattice parameters of PZT (52/48) interfacial layer and PMN-PT film respectively. The misfit strain calculated using formula 6.1 for PZT

interfacial layer and PMN-PT film is summarized in table 6.2. The reciprocal space maps for the selected samples are shown in figure 6.2.

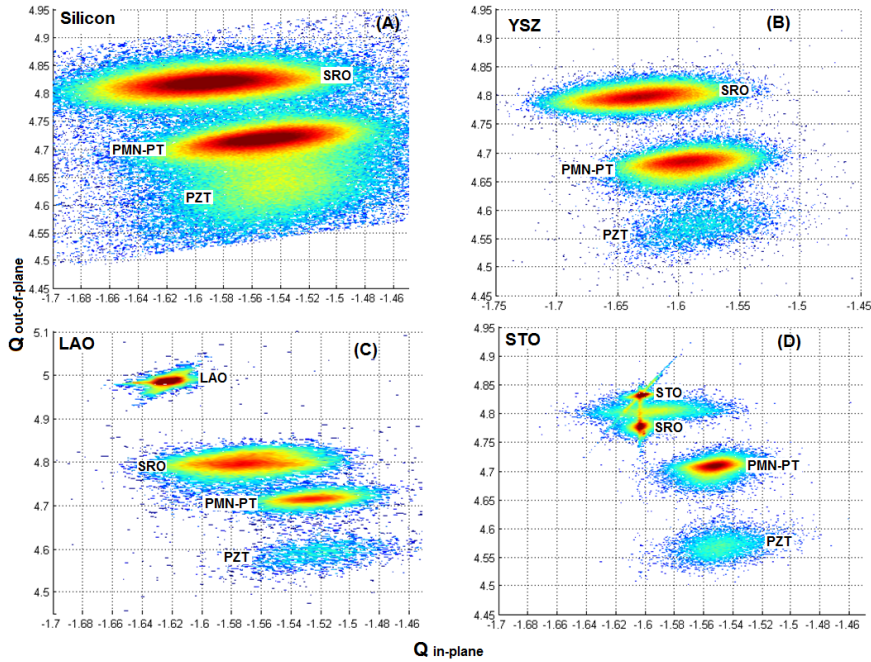


Figure 6.2: XRD reciprocal space map for PMN-PT film grown on (001) $\text{CeO}_2/\text{YSZ}/\text{Si}$ (a) (001) CeO_2/YSZ (b) (001) LAO (c) and (001) STO (d) substrates. The (103) planes of the $\text{CeO}_2/\text{YSZ}/\text{Si}$ can be detected due to in-plane 45° rotation with respect to electrode and PZT/PMN-PT bilayer stack.

Table 6.2 shows the misfit strain [$S_M (10^{-3})$] ranging from 0 to -8 for PZT (25/48) interfacial layer. The misfit strain values show that PZT film deposited on different substrate is under compressive strain except on silicon substrate which shows complete strain relaxation in this case. The strain in the PZT films deposited on silicon can relax by the formation of structural defects as well as domains. The first is less likely because film show good crystalline quality as well film thickness is much smaller than critical thickness for epitaxial strain relaxation. Most probably, the strain relaxation took place via domain

formation. The exact mechanism behind this unexpected behavior is not clear. The calculated misfit strain for PZT interfacial layer is much higher than reported for 250nm thick epitaxial PZT (52/48) film deposited by pulsed laser deposition on similar substrates [14]. This significantly higher strain calculated in our case is due to the combine effect of thermal strain (strain due to difference of thermal expansion coefficients) and epitaxial strain (strain due to different of crystal lattice parameters). The PZT thickness in our case is much less than critical thickness reported for complete crystal lattice (epitaxial) strain relaxation for epitaxial PZT thin films. The reported critical thickness for epitaxial strain relaxation is $>80\text{nm}$ [6].

The table 6.2 also show $S_M(10^{-3})$ calculated for epitaxial PMN-PT films deposited on different substrates using PZT interfacial layer. It ranges from -2.3 to 2.7. The PMN-PT film deposited on MgO substrate is under compressive strain while on other substrates is under tensile strain except YSZ which shows complete strain relaxation. The PMN-PT film grown on MgO substrate is under compressive strain due to higher thermal expansion coefficient compared to PMN-PT film. The PMN-PT films grown on STO, YSZ and LSAT substrates is expected to show compressive strain due to higher thermal expansion coefficients than PMN-PT. The PMN-PT films show tensile strain which is unexpected. This indicates that S_M is not proportional to the difference of thermal expansion coefficients. Additional factors like strain relaxation mechanism that may differ from substrate to substrate as well as additional crystal lattice (epitaxial) strain can influence the total strain in the film [14]. The crystal lattice strain seem the possible reason for tensile strain in PMN-PT films deposited on STO substrates. The FWHM for this sample is 0.05 indicating very crystalline quality of this films. This indicates that crystal lattice strain is not relaxing completely via structural defects in this case. The thermal expansion coefficients of other substrates are lower compared to PMN-PT. Hence, the deposited films are under tensile strain which is expected.

Table 6.2: In-plane and out-plane lattice parameters and S_M of PZT interfacial layers and PMN-PT films deposited on SRO electrode on different substrates.

Sample	Interfacial Layer (PZT)				PMN-PT			
	a (Å)	c (Å)	a_0 (Å)	S_M ($\times 10^{-3}$)	a (Å)	c (Å)	a_0 (Å)	S_M ($\times 10^{-3}$)
MgO-B1	4.037	4.113	4.062	-6.2	4.007	4.035	4.016	-2.3
YSZ-B2	4.039	4.112	4.063	-5.9	4.018	4.019	4.018	0.0
LSAT-B3	4.036	4.110	4.061	-6.2	4.026	4.015	4.022	1.0
LAO-B4	4.039	4.112	4.063	-5.9	4.029	4.010	4.023	1.5
DyScO ₃ -B5	4.032	4.130	4.064	-8.1	4.034	4.004	4.024	2.5
STO-B6	4.043	4.129	4.072	-6.9	4.035	4.007	4.026	2.2
NGO-B7	4.055	4.100	4.071	-3.5	4.038	4.006	4.027	2.7
Si-B8	4.056	4.057	4.056	0.0	4.032	3.999	4.021	2.7
Bulk	4.05	4.11	4.070	×××	4.022	4.022	4.022	×××

6.4.2 Ferroelectric and piezoelectric properties

To investigate the effect of substrate induced strain on ferroelectric and piezoelectric properties of epitaxial PMN-PT films, three samples out of eight are selected for further analysis. The PMN-PT films deposited on MgO substrate (B1) is under highest compressive strain in this study while the PMN-PT film grown on STO substrates (B6) is under tensile strain. These two samples are selected due to almost equal magnitude of strain (compressive for B1 and tensile for B6). The third sample (B6) was selected because it shows intermediate strain (tensile) within these samples.

The P-E loops, dielectric curves and d_{33} loops for selected samples are shown in figure 6.3. Although all three samples have similar orientation but their P-E characteristics are substantially different. The common feature of these P-E loops is characteristics slanting of relaxor type films. The second common feature is the imprint i.e. the shift of the P-E loops due to negative bias field whose magnitude is different for different samples.

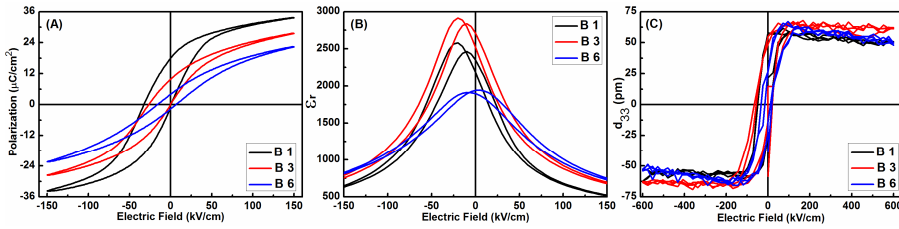


Figure 6.3: P-E loops of the PMN-PT films deposited using PZT as interfacial layer for B1, B3 and B6 (a) the dielectric curves for the same samples derived from the electric field versus capacitance measurements (b) d_{33} loops for the same samples from which longitudinal piezoelectric coefficient are derived (c).

The PMN-PT film which is under compressive strain shows very large polarization (B1). The magnitude of the polarization decreases as the misfit strain corresponds to PMT-PT film increases to positive value i.e. from high compressive strain to intermediate (tensile) strain (B3) and further towards even higher tensile strain (B6). The similar trend is expected for other samples which are not shown here.

Table 6.3 shows the out-of-plane polarization $P(0)$ at zero field obtained from the high field extrapolation for selected samples. The decreasing trend can be observed from compressive strain towards tensile strain. This trend is attributed to the rotation of the polarization vector away from the film plane. It is necessary to mention here that polarization vector is along the $[<111>]$ easy axes of a (001) oriented, unstrained PMN-PT single crystals. The PMN-PT film deposited on MgO substrate (B1) is under compressive strain which will rotate the polarization vector towards film plane. Due to this rotation, this sample showed higher polarization. The other two samples (B3 and B6) are under tensile strain. The lower polarization $P(0)$ is observed for these samples (B3 and B6) compared to the sample which is under compressive strain (B1). Considering these two samples which are under tensile strain, the higher polarization $P(0)$ for the sample under lower tensile strain (B3) is observed compared to the sample which is under higher under tensile strain (B6). Tensile strain causing rotation

the polarization vector away from the easy axes in the opposite direction of film normal. The rotation of the polarization vector is higher for the sample which have higher tensile strain (B6) result larger decay in the polarization compared to the sample having relatively lower tensile strain (B3).

Another striking difference in terms of P-E loops is the existence of the self-bias. The higher self-bias was observed for the B1 which decays for the B3 and even further decreases for B6. This self-bias is associated with the combine effect of the strain in the PZT interfacial layer and PMN-PT main ferroelectric layer. The overall strain in this sample (B1) is higher compared to the other two samples. Hence this sample shows higher self-bias field. The higher strain results higher number of defected dipoles causing higher built-in-bias for this sample. However for the sample B3, the strain in the PZT interfacial is almost similar to B1 but still this sample shows comparatively lower self-bias field. This is attributed to overall lower strain compared to sample B1. This sample have less number of defected dipoles caused by strain, hence lower self-bias is observed in this case. For B6, the strain in the PZT interfacial layer is also almost similar to other two samples. Still this samples shows lowest self-bias. This sample possess very high crystalline quality (FWHM= 0.05) of the PMN-PT film. Due to exceptionally high crystalline quality of this film, the number of defected dipoles are very small. That's why this sample have very small self-bias field. In this analysis, it is noticed that self-bias field is consequence of strain as well as density of structural defects in the PMN-PT film.

The dielectric properties of these samples are also different. The shift of the dielectric curve is similar to P-E loops. This shift decreases the permittivity at zero field and enhances the figure of merit which is beneficial for devices (sensors and actuators operating at zero volts). Nagarajan and co-workers studied the effect of epitaxial strain relaxation in PMN-PT films and found improvement in dielectric properties with strain relaxation. The PMN-PT film deposited on LSAT substrate is more relaxed compared to other two

samples. Hence this film shows higher dielectric properties. The other samples show almost similar strain but opposite sign (compressive and tensile). These two films show different dielectric behavior due to different strain relaxation mechanisms on different substrates.

The longitudinal piezoelectric coefficient shows similar trend. It is higher for the relaxed film. The electric field induced phase change (pseudocubic to tetragonal) can occur in PMN-PT films which can enhance the piezoelectric response. This effect is more likely in relaxed film. As the compressive strain already deforms the unit cell from pseudocubic to tetragonal. So the chance of this contribution diminishes. That's why the PMN-PT films under tensile strain have relatively higher piezo response compared to compressively strained film. The ferroelectric, dielectric and piezoelectric properties of the selected samples are summarized in table 6.3.

Table 6.3: The ferroelectric, dielectric and piezoelectric properties of PMN-PT films deposited on MgO, LSAT and STO substrates.

Sample	S_M ($\times 10^{-3}$)	$P(0)$ ($\mu\text{C}/\text{cm}^2$)	$E_{c.av}$ (kV/cm)	E_{sb} (kV/cm)	ϵ_r (max)	ϵ_r (0V)	d_{33} (pm)
B1	-2.3	25.78	16.5	-16.32	2525	2266	60
B3	1.0	16.80	13.5	-13.35	2879	2614	68
B6	2.2	12.42	11.32	-4.92	1970	1958	66

6.5 Conclusions

The perovskite phase and (001) orientation pure epitaxial PMN-PT films have been fabricated on a wide range of substrates using PZT as interfacial layer. The PZT interfacial layer is under compressive strain on all substrates except silicon. PMN-PT films are under tensile strain except MgO and YSZ substrate. The PMN-PT films on MgO substrate are under compressive strain while on YSZ are completely relaxed. The PMN-PT films on YSZ, LSAT, STO substrate are under tensile strain which is unexpected. The epitaxial

strain and/or strain relaxation mechanism appears the dominating factor over strain induced by the difference of the thermal expansion coefficient. The samples analyzed with respect to ferroelectric, dielectric and piezoelectric properties show that strain can effect the properties of epitaxial PMN-PT films significantly. The knowledge of strain effect on properties of epitaxial PMN-PT films is useful to engineer a PMN-PT film to achieve desired properties for specific applications.

6.6 References

- [1] P.-E. Janolin, J. Mater. Sci. 44 (2009) 5025.
- [2] M. P. Warusawithana, C. Cen, C. R. Slesman, J. C. Woicik, Y. Li, L. F. Kourkoutis, J. A. Klug, H. Li, P. Ryan, L. P. Wang, M. Bedzyk, D. A. Muller, L. Q. Chen, J. Levy, D. G. Schlom, Science, 324 (2009) 367.
- [3] S. P. Alpay in Handbook of Thin Film Materials, Vol.: 3, Ferroelectric and Dielectric Thin Films, "Twinning in Ferroelectric Thin Films: Theory and Structural Analysis," edited by H. S. Nalwa, pp. 517-543, Academic Press (San Diego), 2002.
- [4] G. Shirane, K. Suzuki and A. Takeda, J. Phys. Soc. Japan, 7 (1952) 12.
- [5] N. Pertsev and A. Zembilgotov, J. Appl. Phys. 80(11)[1996] 6401.
- [6] S. Gariglio, N. Stucki, J. M. Triscone, and G. Triscone, Appl. Phys. Lett., 90 (2007) 202905.
- [7] B. Kwak, A. Erbil, J. Budai, M. Chisholm, L. Boatner and B. Wilkens, Phys. Rev. B, 49 (21)[1994] 14865.
- [8] S. P. Alpay, A. L. Roytburd, J. Appl. Phys. 83(1998) 4714.
- [9] K. S. Lee and S. Baik, J. Appl. Phys. 87(2000) 8035.
- [10] Y. K. Kim, S. S. Kim, H. Shin and S. Baik, Appl. Phys. Lett., 84 (2004) 5085.

- [11] F. Bai, H. Zheng, H. Cao, L. E. Cross, R. Ramesh, J. Li and D. Viehland, *Appl. Phys. Lett.*, 85 (2004) 4109.
- [12] V. Nagarajan, C. S. Ganpule, B. Nagaraj, S. Aggarwal, S. P. Alpay, and A. L. Roytburd, *Appl. Phys. Lett.*, 75 (1999) 4183.
- [13] V. Nagarajan, S. P. Alpay, C. S. Ganpule, B. K. Nagaraj, S. Aggarwal, *Appl. Phys. Lett.*, 77 (2000) 438.
- [14] M. D. Nguyen, M. Dekkers, E. Houwman, R. Steenwelle, X. Wan and G. Rijnders., *Appl. Phys. Lett.*, 99 (2011) 252904.
- [15] S. H. Baek, J. Park, D. M. Kim, V. A. Aksyuk, R. R. Das, S. D. Bu, D. A. Felker, J. Lettieri,...C. B. Eom, *Science*, 334 (2011) 958.
- [16] G. Koster, B. L. Kropman, G. J. H. M. Rijnders, D. H. A. Blank, and H. Rogalla, *Appl. Phys. Lett.* 73 (1998) 2920.
- [17] J. E. Kleibeuker, G. Koster, W. Siemons, D. Dubbink, B. Kuiper, J. L. Blok, C. H. Yang, J. Ravichandran, R. Ramesh, J. E. ten Elshof, D. H. A. Blank and G. Rijnders, *Adv. Func. Mater.*, 20 (2010) 3490.
- [18] J. E. Kleibeuker, B. Kuiper, S. Harkema, D. H. A. Blank, G. Koster, G. Rijnders, P. Tinnemans, E. Vlieg, P. B. Rossen, W. Siemons, G. Portale, J. Ravichandran, J. M. Szeplieniec, and R. Ramesh, *Phys. Rev. B*, 85 (2012) 165413.
- [19] M. Dekkers, M. D. Nguyen, R. Steenwelle, P. M. te Riele, D. H. A. Blank and G. Rijnders, *Appl. Phys. Lett.* 95 (2009) 012902.
- [20] J. S. Speck, and W. Pornpe, *J. Appl. Phys.*, 76 (1994) 446.

7.

Integration with Silicon

Chapter Overview:

Epitaxial PMN-PT films with different out of plane orientation [(001) and (110)] sandwiched between symmetric SrRuO_3 electrode were deposited on a CeO_2/YSZ bilayer buffered silicon substrate. The orientation switch from (110) to (001) of the SrRuO_3 bottom electrode was achieved by carefully controlling the fabrication conditions. Subsequent PMN-PT layer follows the orientation of the bottom electrode. The ferroelectric and piezoelectric properties of the ($\text{SrRuO}_3/\text{PMN-PT}/\text{SrRuO}_3$) ferroelectric capacitors with two different crystallographic orientation were compared which showed orientation dependence. Additionally, epitaxial PMN-PT thin film based sensing devices (cantilevers) were also fabricated using SrTiO_3 buffered silicon substrate. To fabricate cantilevers, PMN-PT film were prepared using PZT (20/80) as interfacial layer on SrRuO_3 electroded and SrTiO_3 buffered silicon substrate. The SrTiO_3 buffered silicon substrates were preferred over CeO_2/YSZ bilayer buffered silicon due to remarkably better crystalline quality of the former template compared to later.

This chapter is submitted as:

- Epitaxial PMN-PT films with different out of plane orientation on silicon.
- Fabrication of epitaxial PMN-PT film based free standing cantilever.
(to be submitted)

7.1 Introduction

Silicon is a gold standard substrate for ferroelectric oxide thin film based electronic, photonic and MEMS (Micro Electromechanical Systems) devices [1-2]. It is readily available at comparatively low cost with very high crystalline and surface quality essential for thin film growth. Other advantages of silicon include good thermal conductivity and well developed processing options/tools from standard silicon technology. The main drawback of silicon for the fabrication of MEMS devices is its passive nature that it needs metallic electrodes to capacitively displace MEMS devices.

The direct growth of lead (Pb) based materials on silicon substrates at high temperature ($\approx 600^\circ\text{C}$) is mostly difficult owing to interdiffusion and interfacial reactions between lead (Pb) and silicon substrate. This interaction degrades both silicon and functional properties of the deposited thin films [3-5]. To achieve epitaxial growth of Pb based materials on silicon substrates, buffer layer(s) is required. The selection of the suitable buffer layer(s) is crucial. Buffer layer(s) not only prevents the interfacial reactions but also plays a key role in controlling the crystallinity and crystallographic orientation of the subsequent layer [5-6]. During the selection of buffer layer(s), issues like lattice mismatch, thermal expansion coefficient, thermal stability, chemical inertness, crystal structure etc. have to be considered. The epitaxial growth of PMN-PT thin films on silicon substrates had been demonstrated using appropriate buffer layer(s) which not only prevent interfacial reactions but also reduce large crystallographic lattice mismatch between silicon (5.43\AA) and PMN-PT ($\approx 4.02\text{\AA}$) [6-10].

Ferro and piezoelectric properties of the most noticeable ferroelectric oxides (the pure ferroelectric $\text{PbZr}_x\text{Ti}_{1-x}\text{O}_3$ (PZT) and the relaxor ferroelectric $(\text{PbMg}_{1/3}\text{Nb}_{2/3}\text{O}_3)_{0.67}\text{-(PbTiO}_3)_{0.33}$ (PMN-PT) etc.) are strongly correlated with the crystallographic orientation of the thin films. Therefore, A strong effort have been paid to fabricate

epitaxial PZT and PMN-PT thin film based devices on silicon with desirable orientation. Here we discuss specifically the PMN-PT thin films. It is challenging to overcome the large lattice mismatch between the PMN-PT and the silicon substrate and appropriate buffer layer(s) is required to achieve epitaxial growth. The crystallographic orientation is also influenced by the buffer layers, hence it is highly desirable to engineer the buffer layer to achieve optimised films with high crystallinity and desired orientation.

Bulk relaxor ferroelectrics like PMN-PT exhibit superior piezo-response, and 5 to 10 times larger piezoelectric coefficients than bulk PZT ceramics. This material has also a very large electromechanical coupling coefficient, $k_{33} \approx 0.9$ [11]. Hence it is an auspicious candidate for hyper active MEMS for sensor and actuator applications.

A number of buffer layers have been developed to achieve epitaxial growth of PMN-PT films on silicon. Baek et al. reported the deposition of highly crystalline, epitaxial PMN-PT films on SrTiO_3 buffered silicon substrate [6]. W. Wang and co-workers developed a $\text{SrTiO}_3/\text{TiN}/\text{Si}$ heterostructure while W. S. Tsang et al. demonstrated that the $\text{MgO}/\text{TiN}/\text{Si}$ bilayer system can be successfully used to obtain epitaxial growth of PMN-PT on silicon [7-8]. The Yttria-stabilized zirconia/ceria (YSZ/CeO_2) heterostructure is one of the most extensively investigated layer stacks for epitaxial growth of ferroelectrics oxide films on silicon [9,12-13]. There are reports on the deposition of (001) and (110) oriented epitaxial PMN-PT films using appropriate buffer layer(s) and/or electrode material [6,9]. However, there is no literature about the control of the crystallographic orientation of epitaxial PMN-PT films on a silicon substrate *without* changing the buffer layer(s) and/or the electrode material.

This chapter deals with epitaxial PMN-PT (67/33) films with (001) or (110) orientation which are controllably fabricated on silicon substrates using the *same* buffer layer/base electrode materials stack. This offers the opportunity to investigate the effect of structure and crystallographic orientation on the ferro and piezoelectric properties of

epitaxial PMN-PT films on a silicon substrate. Furthermore PMN-PT thin film based sensing devices (cantilever) has been fabricated. To fabrication cantilevers, PMN-PT thin film based heterostructures were deposited in SrTiO_3 buffered silicon substrates [14]. This template was preferred over CeO_2/YSZ bilayer buffered silicon substrates for the fabrication of cantilevers because of its exceptionally high crystallinity and surface quality. The PMN-PT films based heterostructures which will be discussed in this chapter are schematically shown in figure 7.1.

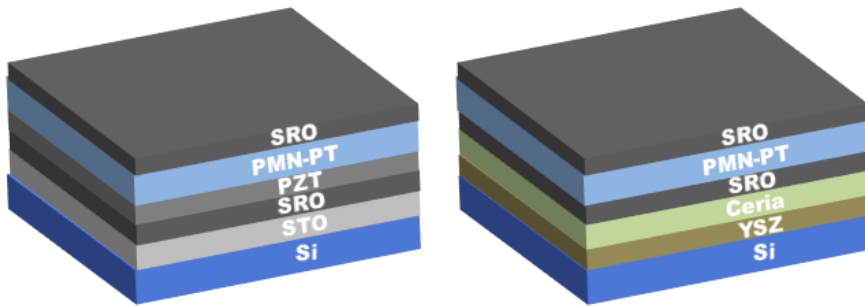


Figure 7.1: Schematic of the epitaxial PMN-PT layer stack deposited for the fabrication of cantilevers (left) and the heterostructure used to study the effect of two different out of plane orientation of PMN-PT films on silicon substrate (right).

7.2 Orientation control of PMN-PT films [(001) and (110)]

7.2.1 Thin films growth

200 nm thick epitaxial PMN-PT (67/33) films were fabricated using 100 nm thick SrRuO_3 (SRO) base and top electrodes. The SRO/PMN-PT/SRO structures are deposited on a (001) oriented silicon substrate buffered with a CeO_2/YSZ bilayer stack (each layer is 50 nm thick). To avoid undesirable contaminations, the full heterostructure ($\text{Si}/\text{YSZ}/\text{CeO}_2/\text{SRO}/\text{PMN-PT}/\text{SRO}$) was deposited without breaking the vacuum. All samples are deposited via Pulsed

Laser Deposition (PLD) using a KrF Excimer laser (248 nm wavelength). YSZ can grow heteroepitaxially on silicon as it scavenges the native silicon dioxide layer by the interaction with the metal Zr (or Y), which can occur under specific deposition conditions. This allows the reproducible coherent growth of the oxides on a silicon substrate without the need of a hydrofluoric acid (HF) pre-treatment of the silicon substrate [15]. Ceria (CeO_2) grows on YSZ buffer layer with a cube on cube epitaxial relationship and is therefore used as a second buffer layer to further reduce the lattice mismatch between YSZ and the base electrode SRO layer. The in-plane mismatch between the fluorite structure of CeO_2 and the perovskite pseudocubic SRO crystal is only 2.2% if the perovskite cubic unit cell of SRO is rotated in plane by 45° with respect to the CeO_2 unit cell [16-17]. The detailed deposition conditions for the SRO/ CeO_2 /YSZ layer stack were reported elsewhere [12]. The PMN-PT films were deposited at a substrates temperature of 585°C keeping the oxygen pressure at 0.27 mbar. The substrate was placed at a distance of 6 cm from the target. The PMN-PT films deposition was performed at a laser fluence of 2.0 J/cm^2 and 4 Hz repetition rate. After deposition the samples were cooled down in-situ from deposition temperature to room temperature under a 1 bar oxygen pressure.

7.2.2 Thin films characterizations

Crystallographic properties and epitaxial relationships were examined by High Resolution X-Ray Diffraction (XRD) (PANalytical X¹pert PRO MRD). The ferroelectric capacitor devices, $200 \times 200 \text{ }\mu\text{m}^2$ in size, were patterned by photolithography and structured by argon ion beam milling. Ferroelectric hysteresis (P-E) loops were measured with a ferroelectric tester (AixACCT TF Analyser 3000), using a bipolar triangular pulse at a frequency of 1 kHz and with 150 kV/cm amplitude. Fatigue measurements were performed using a rectangular pulse train at a frequency of 10 kHz and the same amplitude. The effective longitudinal piezoelectric coefficient ($d_{33,\text{eff}}$) loops were

measured with a Laser Doppler Vibrometer (Polytec MSA-400). The electric field vs. capacitance (E-C) measurements were performed with a Keithley 4200 at 10 kHz. The crosssectional samples were prepared to analyse microstructure of the deposited films which was performed using high resolution scanning electron microscope (Carl Zeiss Merlin HR-SEM).

7.2.3 Results and discussions

Figure 7.2(a) shows the θ - 2θ profile of a PMN-PT film grown on the SRO/CeO₂/YSZ heterostructure using a (001) silicon substrate. In this case, the SRO bottom electrode was deposited at a substrate temperature of 600°C and a constant oxygen pressure (0.13 mbar). The reflection peaks indicate that the PMN-PT film is in the perovskite phase and has (110) orientation. No extra peaks that correspond to impurity phases or other orientations are observed within the detection limits of our instrument. To investigate the crystalline quality rocking curve measurements were performed. The FWHM of the rocking curve of the PMN-PT (110) peak is 1.6°. This indicates that the (110) plane tilt angle varies significantly within the film.

The in-plane epitaxial relations of the PMN-PT(110)/SRO(110)/CeO₂(001)/YSZ(001)/Si(001) stack were studied using ϕ -scans as shown in figure 7.2(b). The ϕ -scan of the CeO₂/YSZ bilayer stack shows four identical sets of peaks located at the same ϕ angles as the Si-substrate separated by 90°, proving that CeO₂(001)/YSZ(001) bilayer is grown with a cube-on cube epitaxial relationship with the Si(001) substrate, as is typically observed [9,13].

The ϕ -scan in figure 7.2(b) corresponds to the SRO bottom electrode and shows peak doubling of the SRO(002) peaks positioned at +10° and -10° with respect to the position of the silicon peak. This indicates the presence of twin domains in the film as was previously also observed by Hou et al. [18] for SRO directly on YSZ/Si(001) and by Dekkers and co-workers [12] for SRO on CeO₂/YSZ/Si(001). The

(110) oriented growth of the SRO means that the unit cell is rotated over 45° with respect to the film normal. Because of the very small lattice mismatch between the SRO bottom electrode and the successive PMN-PT layer, the growth of PMN-PT follows the orientation of the bottom electrode. Therefore the twin domain structure also exists in the PMN-PT film as was indicated by XRD analysis (not shown). The fairly large rocking curve width of the PMN-PT (110) peak is ascribed to the twin domain structure. The out-of-plane lattice constant of the PMN-PT(110) is obtained as 0.5667 nm, which is slightly (-0.4%) less than that of an unstrained 45° tilted pseudocube ($0.5688\text{nm}=\sqrt{2}a_{pc}$, with $a_{pc} = 0.4020$ nm as determined from the θ - 2θ scan of the (001) film), hence the PMN-PT appears to be slightly tensily strained in the film plane. From Figure 1(c) it is also deduced that part of the PMN-PT (002) reflection is slightly shifted to lower angles from the angle expected for rhombohedral, unstrained PMN-PT. The broad shoulder (see inset) indicates a compressive strain of the in-plane lattice constant of the part of the layer on top of the bottom SRO layer, relaxing to the bulk value. It was previously shown that such a layer with a decreasing gradient of tetragonally strained PMN-PT induces a large self-bias field in the device, causing a large shift of the PE-loop [19].

Figure 7.2(c) shows the θ - 2θ scan of the (001) oriented PMN-PT films. Also here no additional peaks corresponding to impurity phases or other orientations were detected. The FWHM of the rocking curve of the PMN-PT (002) peak is 0.7° , which is half that of the (110) oriented PMN-PT films, reflecting the observation that there is no twinning in the (001) film. In this case, the first few atomic layers (≈ 4 Å) of the SRO bottom electrode was deposited under a reduced oxygen plasma pressure ($<10^{-5}$ mbar) and high substrate temperature of 800°C . Apart from this, the deposition conditions for the rest of the stack were equal to that of the (110) oriented film. The ϕ -scan measurements shown in figure 7.2(d) demonstrate the in-plane epitaxial relations of the SRO(001) with the Si(001) substrate. All the

layers have a four-fold rotational symmetry confirming the epitaxial growth of all the layers. The epitaxial relation between $\text{CeO}_2(001)/\text{YSZ}(001)/\text{Si}(001)$ is similar to the former case. However the ϕ scan of the subsequent SRO layer is notably different. It is rotated in-plane by 45° with respect to the buffer layers and silicon substrate. Thus the SRO unit cell is in-plane rotated. This epitaxial relation has earlier been observed for the same $\text{SRO}/\text{CeO}_2/\text{YSZ}/\text{Si}(001)$ heterostructure [12, 17]. A set of four identical peaks of the successive PMN-PT layer (not shown) are positioned at the same ϕ angles as the SRO, reflecting the cube-on-cube epitaxial relation with the SRO bottom electrode.

Thus the increase in deposition temperature, together with lowering the oxygen pressure during the growth of the first SRO unit cell layer is found to have a profound effect on the film stoichiometry. The mismatch of 45° in-plane rotated (001)- oriented SRO on CeO_2 is less than that of (110) oriented SRO on CeO_2 . The reason that under normal deposition condition SRO grows (110) oriented on the CeO_2 must be that, when both elements (Sr and Ru) are present in equal amounts, the nucleation of a (110) oriented SRO unit cell is energetically more favorable than that of a (001) oriented unit cell. SRO grows (001) oriented when only Sr is present on the CeO_2 when SRO is deposited under reducing conditions (loss of volatile Ru). It is believed that this is due to the evaporation of the Ru during the initial deposition, which consequently gives rise to a Sr enriched starting layer, favouring the formation of a SrO monolayer that acts as a (001) oriented base plane for the perovskite block of SRO. Continuation of the growth under normal conditions causes the (001) oriented growth of the SRO bottom [12].

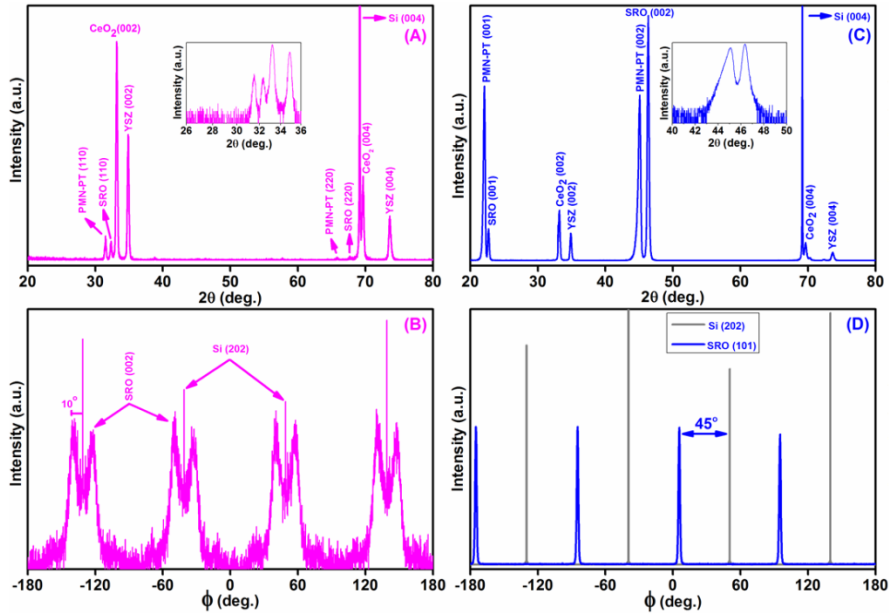


Figure 7.2: (a) XRD θ - 2θ diffractogram of 200nm thick (110) oriented PMN-PT film deposited on SRO(110)/ CeO_2 (001)/YSZ(001) tri-layer system on a silicon substrate. The inset shows an expansion of the (110) reflection. (b) Corresponding ϕ scan associated with silicon substrate and SRO bottom electrode. (c) XRD pattern of 200nm thick (001) oriented PMN-PT films with inset of the (002) reflection deposited on a SRO(001)/ CeO_2 (001)/YSZ(001) buffered silicon substrate; (d) corresponding ϕ scan of the silicon substrate and SRO bottom electrode.

The ferroelectric hysteresis loops (P-E) of the PMN-PT films with different crystallographic orientation, measured after 10^8 cycles, are shown in figure 7.3(a). The loops show the strong slanting and narrow hysteresis typical for bulk relaxors, and are very symmetric. The polarization of the (110) oriented film is significantly larger than of the (001) oriented film. This is interpreted as being due to the different orientations of the pseudocubic [111] direction, which is the preferential polarization direction in bulk PMN-PT, in these films. The projection of this axis on the film normal direction (3-direction), in which the 3-component of the polarization is measured, is a factor $\sqrt{2/3}$ for a (110)-oriented film, and $\sqrt{1/3}$ for a (001) oriented film,

of the length of a vector in the $[111]_{pc}$ direction. Thus one would expect in a first approximation that the ratio of the measured polarizations for the films with different growth orientations to be $P_{3,(110)}/P_{3,(001)} = \sqrt{2}$. Experimentally the ratio is about 1.2. The difference may be due to the films being still far from saturation. Another striking difference between the loops is the large shift of the loop of the (001) film towards positive field direction indicating the existence of a positive self-bias E_{sb} ($= (E_c^+ + E_c^-)/2$), of magnitude $+ 8.1$ kV/cm. The P-E loop of the (110) oriented PMN-PT films shows a comparatively small, negative self-bias of -2.0 kV/cm. It is worth noting that the self-bias may be beneficial since it can affect the performance of the devices fabricated from these films. For instance self-bias enhances the magnitude of (positive or negative) remanent polarization. Additionally, the build-in bias has the advantage of stabilizing the polarization in certain directions, which may affect positively the aging properties of devices usually caused by voltage and temperature excursions [20-21].

Typically, in perovskite ferroelectrics a compressive in-plane stress results into a positive imprint, whereas in-plane tensile stress acts in the opposite way [22]. Part of the PMN-PT films with (001) orientation are under compressive stress, as was deduced from the shoulder of the PMN-PT(002) reflection, whereas the (110) oriented films are under a slight tensile stress. The observed field shifts of the P-E loops are in the positive and negative direction as expected. Note that the difference of thermal expansion coefficients between PMN-PT and the silicon substrate would suggest the presence of in-plane tensile strain, which cannot explain the difference in field shift for both cases. The XRD analysis showed that the tetragonally strained part of the (001) oriented PMN-PT film shows a strain gradient, with most likely maximum strain at the base electrode/PMN-PT interface and relaxing into the film. This strain relaxation occurs by the incorporation of lattice defects. It was previously shown that a strain gradient can give rise to a large build-in electrical field which is a

possible cause for the self-bias voltage of these films [19]. The (110) oriented films show different ferroelectric behaviour compared to the (001) films, especially the self-bias is much smaller and has opposite sign. In these films strain relaxation is much easier due to the high density of structural defects, due to the twinning of the crystal structure of the bottom electrode and PMN-PT film. This is consistent with the XRD rocking curve measurements which show that the (110) oriented films have more peak broadening, hence a larger tilt angle range of the crystallites within the film and likely a higher density of structural defects compared with the (001) films. The much increased strain relaxation causes the strain gradient layer to be very thin, as is evidenced by the fact that the θ - 2θ (110) reflection does not show an obvious asymmetry (shoulder). The self-bias voltage is low and negative, suggesting that the build-in field is (over-) compensated by charged defects [19].

The relative dielectric constant curves of the deposited PMN-PT films are shown in figure 2b. The lower slope of the polarization loop of the PMN-PT(001) film is reflected in the lower dielectric constant for this film compared with that of the (110) film. The self-bias voltage slightly shifts the CE-loop of the (001) film.

The loops of the piezoelectric coefficient $d_{33} = (\partial S_3 / \partial E_3)_\sigma$ (the strain in the out-of-plane direction under an applied field in the same direction, under constant stress conditions) is very symmetric for the (001) oriented film, but is asymmetric for the (110) film. The width of the (sloped) switching part of the hysteresis loops is approximately as wide as the opening of the P-E loops. The coercive field in the d_{33} -loops is significantly larger than that of the PE-loops, indicating that there is an additional mechanism contributing to the value of d_{33} , most likely domain wall pinning. From theoretical modelling it was concluded that the interaction between domains is an important factor in determining the dielectric and piezoelectric response in clamped thin films [23]. There is also a remarkable difference between the d_{33} -loops of the two types of films. The loop of

the (001) oriented film is square and symmetric, but with a slight voltage bias, and saturates at about 38 pm/V. In contrast the loop of the (110) film shows strong maxima near the coercive field, which are asymmetric for negative applied field. The nearly constant d_{33} of the (001) film implies that the unit cell height increases linearly with applied field, whereas the unit cell height in the [110] direction of the (110)-film is more sensitive to the change in field at low fields than at higher field strengths, where d_{33} saturates at nearly the same value as for the (001)-film. In the (001) film the polarization vector rotates in a (110) plane from the [111] direction towards the \pm [001] direction under the influence of the applied field in the \pm [001] direction, whereas in the (110) film it rotates in the opposite direction towards the \pm [110] direction in a field in the \pm [110] direction. Apparently the latter rotation direction coincides with a larger displacement of the Zr/Ti ion with respect to the O-lattice, causing a larger polarization (as can be seen from the larger polarization values in the PE-loop) as well as a larger expansion of the lattice (larger d_{33}). For an increasing field in the direction of the top electrode (negative bias voltage) the lattice expansion is easier (d_{33} is larger over a large field range) than for decreasing field in the same direction. This suggests that the film is more elastic when the Zr/Ti ions, positioned closer to the top electrode within the unit cell, are moving towards the top electrode, than away from the top electrode towards the bottom electrode. On the other hand for positive bias, the Zr/Ti ions are positioned closer to the bottom electrode and movement towards the bottom electrode appears to be approximately as easy as away from it.

The maximum d_{33} values attained in these films are significantly smaller than the bulk values reported, up to 2500 pm/V [11]. The large effective d_{33} values reported for PMN-PT single domain, single crystals, poled in the (001) or (110) direction is ascribed to the large contribution of the large shear component d_{15} to $d_{33,eff}$. [24]. However in the films considered here, shearing is likely to be largely obstructed by the shear in different directions of adjacent

grains with the $\langle 111 \rangle$ polar axis in different in-plane directions. In addition the d_{33} contribution is reduced by the clamping to the substrate. We think that both factors contribute to the relatively small $d_{33,eff}$ values found.

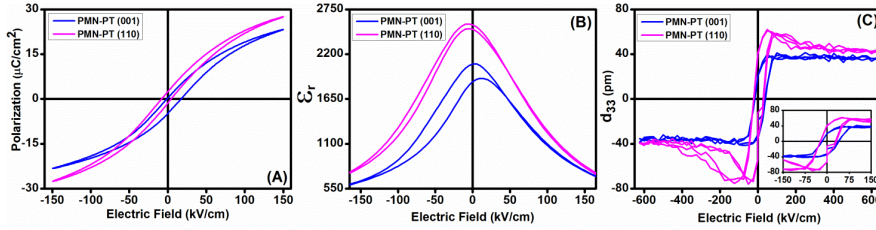


Figure 7.3: (a) Polarization hysteresis loop; (b) capacitance loop; (c) piezoelectric coefficient $d_{33,eff}$ of 200nm thick (001) and (110) oriented PMN-PT films on CeO₂/YSZ buffered (001)-oriented Si substrate, using SRO electrodes.

To analyse the effect of orientation and structure on the stability of the ferroelectric response, both films were subjected to a large number (10^9) of switching cycles. The main feature is the shift along the field axis of the PE-loop upon cycling, reflected in shifting coercive fields and thus a changing self-bias field (fig 7.4b). Both films show a shift in the negative field direction upon cycling. The relative change in self-bias of the (110) film is larger than that of the (001) film, although the absolute values are nearly the same. We interpret this shift as being due to an increased density of defect related charges in the ferroelectric, probably at the interface with the bottom electrode, where the strain gradient is present. The average coercive value $|E_c| = |E_c^+ - E_c^-|/2$ of the (001) oriented film only slightly increases with cycling, although beyond about 3×10^8 cycles a stronger increase seems to be present. Cycling of the (110) oriented PMN-PT films beyond 10^7 cycles causes opening of the P-E loop due to an increased leakage current, which is reflected in a strongly increasing value of $|E_c|$. This is ascribed to the existence of the electrically less stable grain boundaries due to the twins in the (110) oriented PMN-PT. Apparently the grain boundaries in the (001)

oriented film are much more stable, so that deterioration of the loop and increase of $|E_c|$ only sets in at a much larger cycle number.

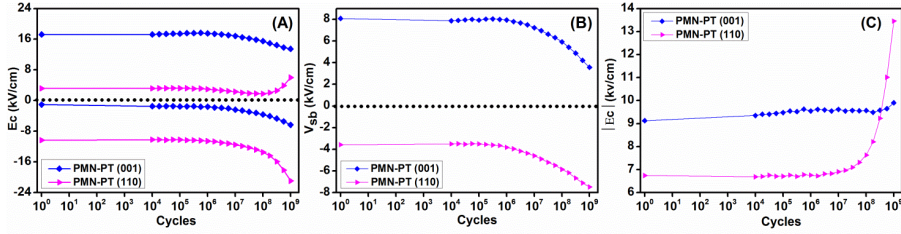


Figure 7.4: (a) Coercive fields, (b) self-bias field, and (c) average coercive field versus number of aging cycles performance of (001) and (110) oriented PMN-PT films on CeO₂/YSZ buffered (001)-oriented Si substrate, using SRO electrodes.

The microstructure of the epitaxial PMN-PT film with two different out-of-plane orientation (001 and 110) is shown in the figure 7.5.

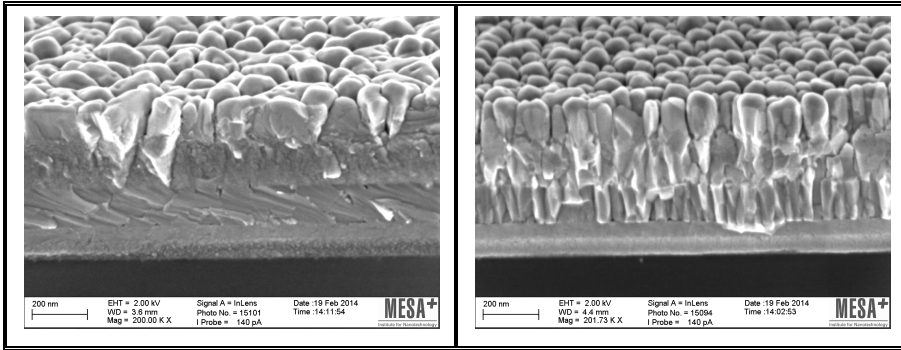


Figure 7.5: HRSEM image of the (001) oriented epitaxial PMN-PT film deposited using YSZ/CeO₂ buffered silicon substrate (left image) and (110) oriented epitaxial PMN-PT film (right image).

It can be observed that microstructure of the two films is entirely different. The change of the microstructure originate from the bottom electrode. The deposition of few monolayers of SRO bottom electrode (SRO (001) orientation case) using low pressure and

temperature not only change the orientation but also the microstructure of the bottom layer. The bottom electrode microstructure seems to effect the microstructure of the successive layers. The (001) oriented PMN-PT film possess dense microstructure compared to (110) oriented film which is columnar. The less dense columnar structure might be the possible reason of superior longitudinal piezoelectric response of these films [25].

7.3 Fabrication of PMN-PT film based free standing cantilever

7.3.1 Deposition of PMN-PT films stack for cantilever beam

Epitaxial PMN-PT/PZT bilayer stack is sandwiched between 60 nm thick SrRuO_3 (SRO) base and top electrodes. The film thickness of PMN-PT (67/33) and PZT (20/80) is 300nm and 25nm respectively. Heterostructure ($\text{SRO/PMN-PT/PZT/SRO}$) schematically shown in figure 7.1 (left) are deposited on a (001) oriented SrTiO_3 buffered silicon substrates provided by D. G. Schlom, Cornell University, USA [14]. The PZT (20/80) composition was preferred over other compositions owing to superior self-bias demonstrated by this interfacial layer. More details about the effect of PZT interfacial layer compositions on ferro and piezoelectric properties of epitaxial PMN-PT films can be found in chapter 4. To avoid undesirable contaminations, the full heterostructure was deposited subsequently without breaking the vacuum. All samples were deposited via Pulsed Laser Deposition (PLD) using a KrF Excimer laser (248 nm wavelength). The growth conditions for PMN-PT, PZT and SRO are similar to that already described in chapter 4.

7.3.2 Structure, ferroelectric and piezoelectric characterization

Crystallographic properties and epitaxial relationships were examined by High Resolution X-Ray Diffraction (XRD) (PANalytical X¹pert PRO MRD). The ferroelectric capacitor devices, $100 \times 100 \mu\text{m}^2$ in size, were patterned by photolithography and structured by argon ion beam milling in addition to free standing cantilever on the same structure. Ferroelectric hysteresis (P-E) loops were measured using these capacitors with a ferroelectric tester (AixACCT TF Analyser 3000), using a bipolar triangular pulse at a frequency of 1 kHz and with 150 kV/cm amplitude. The electric field vs. capacitance (E-C) measurements were performed with a Keithley 4200 at 10 kHz and relative dielectric constants were derived from E-C measurements. The piezoelectric properties of free standing cantilevers were measured with a Laser Doppler Vibrometer (Polytec MSA-400).

7.3.3 Structural properties of PMN-PT films stack

Figure 7.6 shows the θ - 2θ profile of a PMN-PT/PZT film grown on the SrTiO_3 buffered silicon substrate. The reflections corresponds to (001) orientation for both PMN-PT and PZT layer detected. There are no additional peaks corresponding to impurity phases or other orientations. The FWHM of the rocking curve of the PMN-PT (002) peak is 0.36° . These measurements explicitly demonstrate that our heterostructure is in perovskite phase and pure (001) orientated within the detection limits of the instrument. The ϕ -scan measurements (not shown) demonstrate the in-plane epitaxial relations of the PMN-PT (001) with the $\text{Si}(001)$ substrate. All the layers have a four-fold rotational symmetry confirming the epitaxial growth of all the layers. The detailed analysis (ϕ -scans) of the complete stack shows that SrTiO_3 unit cell is rotated in-plane by 45° with respect to the silicon substrate [26]. A set of four identical peaks

corresponds to successive layers (SRO, PZT and PMN-PT) are positioned at the same ϕ angles (not shown) as the SrTiO_3 , reflecting the cube-on-cube epitaxial relation with the SrTiO_3 buffer layer. The complete film stack is rotated in-plane by 45° with respect to the silicon substrate. This epitaxial relation has earlier been observed in PMN-PT films deposited on SrTiO_3 buffered silicon substrate [6].

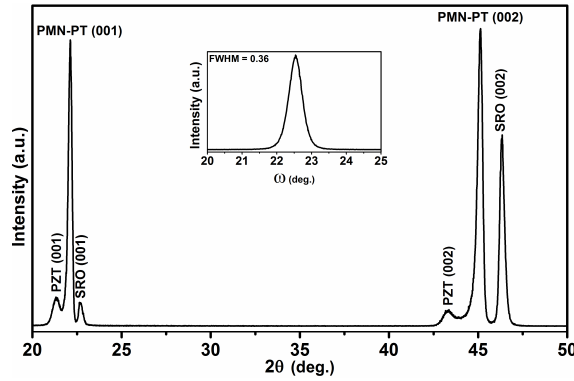


Figure 7.6: XRD θ - 2θ diffractogram of 300nm thick (001) oriented PMN-PT film deposited on SrTiO_3 buffered silicon substrate using PZT (20/80) interfacial layer.

7.3.4 Fabrication process of free standing cantilever

Figure 7.7 shows the flow chart diagram describing step by step fabrication process of free standing PMN-PT thin film based free standing cantilever beam.

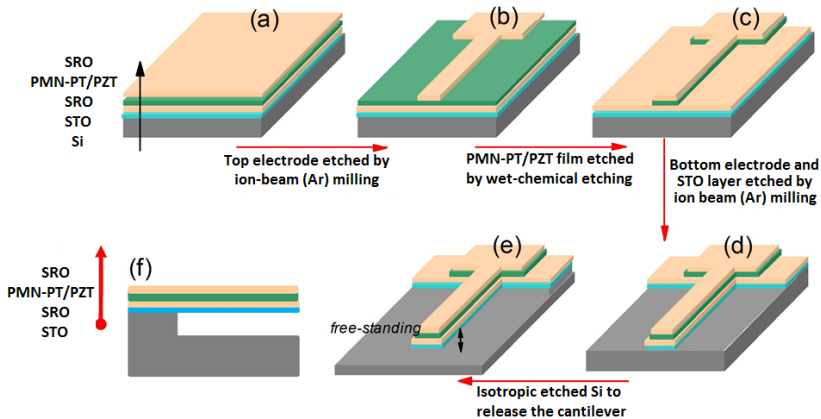


Figure 7.7: Fabrication steps of the free-standing PMN-PT thin film based cantilever: (a) Pulsed laser deposited SRO/PMN-PT/PZT/SRO layer stack deposited on SrTiO₃ buffered silicon substrate, (b) Ar-beam etched SRO top-electrode, (c) wet- chemical etched PMN-PT/PZT bilayer, (d) Ar-beam etched SRO bottom-electrode and SrTiO₃ buffer-layer, (e) Cantilever was released by etching the underlying silicon using SF₆, and (f) Cross-sectional view of a free-standing cantilever beam.

It is necessary to mention here that figure 7.7 which describe process flow diagram shows only the etching steps involved for the fabrication of free standing cantilever. This diagram does not show steps of coating and patterning of the photoresist. These steps were performed by standard photolithography process. It is important to mention here that all heterostructures that were used to fabricate the free standing cantilevers were characterized with respect to perovskite phase and (001) orientation purity to ensure the good quality of the heterostructure. The etching of the top electrode (SRO) was performed using argon-beam etching. The sandwiched piezoelectric layers (PMN-PT/PZT) were etched subsequently using wet-chemical etching. Then the bottom electrode (SRO) and SrTiO₃ buffer-layer were etched using argon-beam milling. Finally, the cantilevers were released by isotropic etching of silicon substrate using SF₆ (Figure 7.7(e)). Using this process, the cantilevers with a width of 25 μm and a length of 70 μm were fabricated. The schematic view of a suggested structure is shown in Figure 7.7(f). The scanning electron microscope (SEM) image of as fabricated PMN-PT thin based free-standing cantilever fabricated using steps described is shown in figure 7.8.

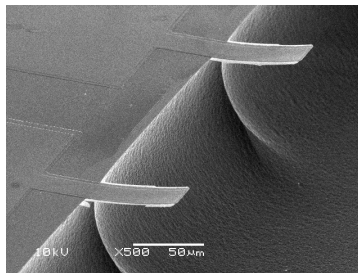


Figure 7.8: SEM image of the PMN-PT thin film based free-standing cantilever beam.

7.3.5 Analysis of the free standing cantilever beam

The Polytech MSA-400 micro-system analyzer was used for the analysis and visualization of the structural vibration and surface topography of microstructures such as piezoelectric cantilevers. A fully integrated optical microscope with a scanning laser Doppler vibrometer (LDV) and a white light interferometer allowed for the measurement of the piezoelectric actuation and initial bending of cantilevers. A schematic diagram for measuring mechanical characteristics can be found in reference [27]. The tip-displacement (δ_t) of the cantilevers was measured under a sinusoidal *ac*-voltage of 1 V and at 8 kHz frequency. Figures 7.8 shows a typical piezoelectric vibration response of a free-standing cantilever with 70 μ m in length and 25 μ m in width. The laser scanning area covered the top electrode.

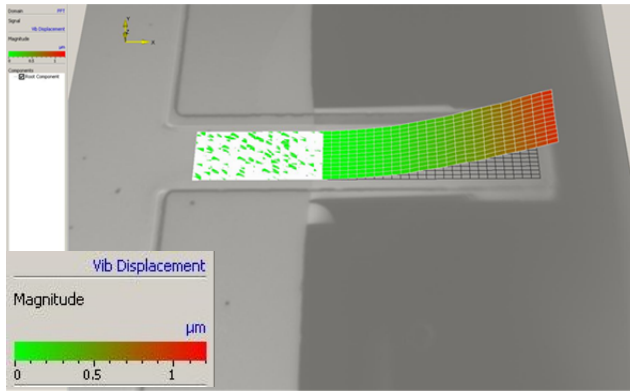


Figure 7.8 LDV measurement showing the displacement of a 70- μ m-length free-standing cantilever, measured at 1V_{ac}-1V_{dc}-8kHz.

The value of transverse piezoelectric coefficient (e_{31}) can be calculated by formula 7.1.

$$\delta = \frac{3d_{31}s_s s_p t_s (t_s + t_p) L^2 V}{s_s^2 t_p^4 + 4s_s s_p t_s t_p^3 + 6s_s s_p t_s^2 t_p^2 + 4s_s s_p t_s^3 t_p + s_p t_s^4} \quad 7.1$$

In this formula, δ is the cantilever tip displacement, s_s and s_p are the mechanical compliances of the substrate and the PMN-PT/PZT bilayer respectively, t_s and t_p are the thicknesses of the substrate and the

PMN-PT/PZT bilayer respectively, L is the length of the cantilever and V is the excitation voltage. The compliance is related to the Young's modulus E by $s = 1/E$. The values for the Young's moduli are taken from reference [6]. The figure of merit (FOM) can be calculated by formula 7.2.

$$FOM = \frac{e_{31}^2}{\varepsilon_0 \varepsilon_r} \quad 7.2$$

PMN-PT film based free standing cantilever ◆ Published in Journal “Science” [6] $e_{31} = -27 \text{ C/m}^2$ FOM = 48 GPa	PMN-PT film based free standing cantilever ◆ From this study $e_{31} = -25.6 \text{ C/m}^2$ FOM = 39.6 GPa
--	---

7.4 Conclusions

In conclusion, relaxor PMN-PT thin films were epitaxially grown on Si substrates using PLD with a CeO₂/YSZ buffer layer. By adapting the growth conditions of the first monolayer of the bottom SRO electrode the growth orientation was switched between the (001) and (110) direction. All oxide layers show in-plane epitaxial relation with the substrate. The PMN-PT films are phase pure and relax to bulk rhombohedral lattice parameters over a thin layer. The (001) oriented film shows a relatively large self-bias voltage, which is ascribed to a strain gradient layer in the relaxor at the interface with the bottom electrode. On long term cycling the self-bias is slightly reduced, probably due to the introduction of charged defects in this strained layer. In the case of the (110) oriented film the self-bias is small and has opposite sign and increases further on cycling. The effective piezoelectric coefficient $d_{33,eff}$ is about 40 pm/V, significantly smaller than that of bulk PMN-PT, which is attributed to the granular nature of the film and clamping by the substrate.

Furthermore, PMN-PT thin film based free standing cantilever beams are fabricated and characterized with respect to transverse piezo-response ($e_{31\text{eff}}$) which shows excellent response.

7.5 References

- [1] D. H. Do, P. G. Evan, E. D. Isaacs, D. M. Kim, C. B. Eom and E. M. Dufresne, *Nat. Mater.* 3 (2004) 364.
- [2] M. D. Nguyen, H. N. Vu, D. H. A. Blank and G. Rijnders, *Adv. Nat. Sci.: Nanosci. Nanotechnol.*, 2 (2011) 2011.
- [3] Y. Shichi, S. Tanimoto, T. Goto, K. Kuroiwa and Y. Tarui, *Jpn. J. Appl. Phys.* 33 (1994) 5172.
- [4] F. F. C. Duval, R. A. Dorey, R. W. Wright, H. Zhaorong, R. W. Whatmore, *J. Electroceram.* 13 (2004), 267-270.
- [5] S. Horita, T. Naruse, M. Watanabe, A. Masuda, T. Kawada, Y. Abe, *Appl. Surf. Sci.*, 117–118 (1997), P. 429-433.
- [6] S. H. Baek, J. Park, D. M. Kim, V. A. Aksyuk, R. R. Das, S. D. Bu and C. B. Eom, *Science*. 334 (2011) 958.
- [7] W. Wang, Q. X. Zhu, X. M. Li, M. M. Yang, X. D. Gao, X. Q. Zhao, *J. Mater. Sci: Mater. Electron.*, 24 (2013) 3782-3787.
- [8] W. S. Tsang, K. Y. Chan, C. L. Mak, and K. H. Wong, *Appl. Phys. Lett.*, 83 (2003) 1599 -1601.
- [9] J. Jiang, S. G. Hur and S. G. Yoon, *J. Electrochem. Soc.*, 158 (2011) G83-G87.
- [10] Y. Okada and Y. Tokumaru, *J. Appl. Phys.*, 56 (1984) 314.
- [11] S. E. Park and T. R. Shrout, *J. Appl. Phys.* 82 (1997) 1804.
- [12] M. Dekkers, M. D. Nguyen, R. Steenwelle, P. M. te Riele, D. H. A. Blank and G. Rijnders, *Appl. Phys. Lett.* 95 (2009) 012902.
- [13] A. Chopra, D. Pantel, Y. Kim, M. Alexe and D. Hesse, *J. Appl. Phys.* 114 (2013) 084107.
- [14] 30nm SrTiO_3 buffer-layer was deposited on silicon by molecular beam epitaxy; samples provided by Prof. D. G. Schlom, Cornell University, USA.

- [15] S. J. Wang, C. K. Ong, L. P. You and S. Y. Xu, *Semicond. Sci. Technol.*, 15 (2000) 836.
- [16] C. A. Copetti, H. Soltner, J. Schubert, W. Zander, O. Hollricher, Ch. Buchal, H. Schulz and N. Klein, *Appl. Phys. Lett.* 63 (1993) 1429.
- [17] M. Kondo, K. Maruyama and K. Kurihara, *Fujitsu Scientific and Technical Journal*. 38 (2002) 46.
- [18] S. Y. Hou, J. Kwo, R. K. Watts, J. Y. Cheng and D. K. Fork, *Appl. Phys. Lett.* 67 (1995) 1387.
- [19] M. Boota, E. P. Houwman, M. Dekkers, M. D. Nguyen, and G. Rijnders, *Appl. Phys. Lett.*, 104 (2014) 00000.
- [20] R. G. Polcawich and S. Trolier-McKinstry, *J. Mater. Res.*, 15 (2000) 2505.
- [21] R. G. Polcawich, J. S. Pulskamp, D. Judy, P. Ranade, S. Trolier-McKinstry and M. Dubey, *IEEE Trans. Microwave Theory and Techn.*, 55 (2007) 2642.
- [22] Z. Zhang and J. H. Park, S. Trolier-McKinstry, *MRS Proc. Ferroelectric Thin Films VIII*, 596 (2000) 73.
- [23] L. Chen and A. L. Roytburd, *Appl. Phys. Lett.*, 90 (2007) 102903.
- [24] S. Zhang and F. Li, *J. Appl. Phys.*, 111 (2012) 031301.
- [25] P. Muralt, *J. Am. Ceram. Soc.*, 91 (5) [2008] 1385.
- [26] S. H. Baek and C. B. Eom, *Acta Mater.*, 61 (2013) 2734.
- [27] M. D. Nguyen, H. Nazeer, M. Dekkers, D. H. A. Blank, G. Rijnders, *Smar. Mater. and Struc.*, 22(8) [2013] 085013.

Acknowledgements

At last, the time has arrived to wrap up my PhD study period. I am feeling very relaxed and happy to write this last page of my PhD dissertation. To achieve this goal, I have had to work long hours including weekends. It is also bringing me back to the different stages of my PhD: my excitements when I observed narrow perovskite phase pure PMN-PT reflections in Bruker D8 Discover and also occasional frustrations when I got pyrochlore phase impurity. All feelings are now equally great memories. Above all this time is reminding me of every single person who was involved in my work and/or has made my time joyful at STM group in Rome, Italy and IMS group in Enschede, The Netherlands. Though, my vocabulary here is very limited, I want to express my great gratitude to,

Prof. Edoardo Bemporad, my wonderful official supervisor. Your encouragement and endless support during the entire PhD study period have made me accomplish this dissertation. Thanks a lot! For believing in me, and for giving me the opportunity to perform my PhD studies in your prestigious group (STM) under your kind supervision. It has been great to have you as my official supervisor. I found you a very kind and great human being.

Prof. Guus Rijnders, my wonderful supervisor in The Netherlands. Thanks a lot! For giving me the opportunity to perform the international part of my PhD studies in your prestigious group (IMS). Thanks a lot! For giving me so much freedom in my research work which inspired me greatly. It has been a great pleasure to work under your kind guidance.

Dr. Giulia Lanzara, my wonderful co-supervisor. Thanks a lot! for introducing me to this exciting field of ferroelectric material research. Many, many thanks for your valuable time and guidance to fix daily research relating issues. I am grateful for your kind time to correct my scientific reports and assessment comments for the evaluation commission every year. I am grateful for your encouragement and support to send me to The Netherlands to complete international part of PhD studies.

Dr. Evert Houwman, thanks a lot! For your kind help to correct my manuscripts and PhD dissertation. I am highly impressed by your deep understanding of this exciting research area. I learnt a lot from you. Without

your kind help, it was not easy for me to understand PMN-PT, a complex and exciting material. You will stay in nice memories belonging to my PhD studies period.

I am thankful to Prof. Fabio, Mark, Gertjan, Andre, Marco, Antonio, and other staff members in IMS and STM group for their help and cooperations.

Special thanks to Matthijn for helping me to correct part of my thesis and manuscripts. I am grateful to Minh for his help. I enjoy a lot to work with you. Special thanks to Huiyu for kind cooperations. You never said no to me whenever I requested for help.

Many thanks to Kurt, Ruud, Zhaoliang, Ben, Rik, Martin, Alim, Tom, Peter, David, Alessandro, Kenan, Brian, Debakanta, Nirupam, Anuj, Federico, Lucia, Giuditta, Luca, Sjoerd, Werner, Michelle, Pablo, Anirban and Gerard for kind helps and cooperations. I am also thankful to colleagues on Nano-lab, ICE group for their cooperations.

I am grateful to my office colleagues; Wouter, Rogier and Petra, in IMS and my officemates; Marco, Mattia, Vincenzo, Rashid in STM group. I enjoyed my work a lot in your nice company. I am grateful for your kind cooperation and creating a pleasant working environment.

I am grateful to technical staff, Henk, Dominic, Frank, Dick, Remco, Daniele and Jose for technical supports. Thanks a lot for keeping us working.

Many thanks to Marion Bollaen (IMS) and Dragana Nikolic (STM) for helping me with all administrative stuff that I have to deal as international student.

I am thankful to all the past and present members of the STM and IMS group for their cooperation.

I would like to give special thanks to my parents, brothers and sisters for their prayers. Many thanks to my wife and children for their endless love, prayers and sacrifices.

Muhammad Boota
May 2014

Publications

(Included in Thesis)

- [1] M. Boota, E.P. Houwman, M. Dekkers, M. Nguyen and G. Rijnders, Epitaxial PMN-PT thin films with large tuneable self-bias field controlled by a PZT interfacial layer, Appl. Phys. Lett., 104 (2014) 182909.
- [2] Muhammad Boota, Evert P. Houwman , Matthijn Dekkers, Minh D. Nguyen, Kurt H. Vergeer, G. Lanzara and Guus Rijnders, Ferroelectric and piezoelectric properties of epitaxial PMN-PT films with (001) and (110) out of plane orientation on silicon.
(Submitted)
- [3] Optimization of the growth of epitaxial PMN-PT thin films on (001) SrTiO₃ substrates.
(In manuscript)
- [4] Dielectric and piezoelectrics properties of epitaxial PMN-PT films controlled by the PZT interfacial layer composition.
(To be submitted).
- [5] The effect of hard and soft doped PZT interfacial layer on structural, ferroelectric and piezoelectric properties of epitaxial PMN-PT films.
(To be submitted).
- [6] The effect of substrate induced strain on ferroelectric and piezoelectric behavior of epitaxial PMN-PT films.
(To be submitted).
- [7] Fabrication of PMN-PT film based free standing cantilever.
(To be submitted).

(Not included in Thesis)

- [1] M. D. Nguyen, E. P. Houwman, M. Boota, M. Dekkers, G. Rijnders, Effect of oxide based-electrode materials on the properties of heteroepitaxial Pb(Zr_{0.52}Ti_{0.48})O₃ thin films on buffered silicon substrates by pulsed laser deposition.
(Submitted)

- [2] The effect of films thickness on ferro and piezoelectric properties of epitaxial PMN-PT films deposited using PZT (50/50) interfacial layer.
(To be Submitted)
- [3] Deposition of PMN-PT films on calcium niobate nanosheets.
(To be Submitted)
- [4] Deposition of PMN-PT films on titania nanosheets.
(To be Submitted)